Universidade de São Paulo
Instituto de Física

Método de Hartree multiconfiguracional para sistemas de muitas partículas

Alex Valerio Andriati

Orientador: Prof. Dr. Arnaldo Gammal

Tese de doutorado apresentada ao Instituto de Física da Universidade de São Paulo, como requisito parcial para a obtenção do título de Doutor em Ciências.
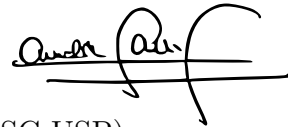
Banca Examinadora:
Prof. Dr. Arnaldo Gammal - Orientador (IFUSP)
Prof. Dr. Caetano Rodrigues Miranda (IFUSP)
Prof. Dra. Monica Andrioli Caracanhas Santarelli (IFSC-USP)
Prof. Dr. Tommaso Macri (UFRN)
Prof. Dr. Peter Schmelcher (Universität Hamburg)

São Paulo
2022

University of São Paulo
Physics Institute

Multiconfigurational Hartree method for many-particle systems

Alex Valerio Andriati

Supervisor: Prof. Dr. Arnaldo Gammal

Thesis submitted to the Physics Institute of the University of São Paulo in partial fulfillment of the requirements for the degree of Doctor of Science.

Examining Committee:
Prof. Dr. Arnaldo Gammal - Supervisor (IFUSP)
Prof. Dr. Caetano Rodrigues Miranda (IFUSP)
Prof. Dra. Monica Andrioli Caracanhas Santarelli (IFSC-USP)
Prof. Dr. Tommaso Macri (UFRN)
Prof. Dr. Peter Schmelcher (Universität Hamburg)

São Paulo
2022

Acknowledgments

Abstract

In the present thesis, the multiconfigurational time-dependent Hartree method is applied to study flow properties of bosons trapped in annular geometry. This physical system provides a suitable platform to investigate beyond meanfield features, since as one spatial dimensional problem, we can explore different interacting regimes, set a rather large range for parameter values without excessive concern about the computational cost and explore relevant concepts, such as superfluidity. As a very important part of the present thesis, the multiconfigurational time-dependent Hartree method for bosons (MCTDHB) is carefully described, providing all relevant derivations up to the final equations of motion, as well as a prospectus of the numerical approach. As such, this thesis also deals with topics of numerical analysis due to its method complexity. After the MCTDHB derivation and its numerical implementation are shown, the superfluid properties of a bosonic gas in annular geometry are studied with the most general approach proposed in reference [1], without any assumptions about the condensation status of the system. In addition, the MCTDHB's capability to provide correlation functions is exploited to characterize the loss of superfluid fraction due to a potential barrier. Within the same goal to study bosonic flow properties in a ring, persistent currents are also investigated, with two alternative derivations for the metastability condition as energy local minimum. Besides, the dynamical decay of the current is analyzed after quenching a potential barrier. Fluctuations of the number operator and probabilities are calculated along the time evolution to provide information about the quantum statistical distribution embedded in experimental measures, aiming to spot relevant information on image observation of flowing states.

keywords: Multiconfigurational Hartree method; many-particle system; bosons; Bose-Einstein condensation; superfluid.

Resumo

Nesta tese, o método de Hartree multiconfiguracional dependente do tempo é aplicado para estudar a circulação de bósons armadilhados em geometria anular. Este sistema físico oferece uma plataforma adequada para investigar características além do escopo de campo médio, uma vez que sendo em uma dimensão espacial, podemos explorar diferentes regimes de interação, estabelecer um longo alcance para valores dos parâmetros sem demasiadas preocupações com o custo computacional e explorar conceitos relevantes, como a superfluidez. Como uma parte muito importante da presente tese, o método de Hartree multiconfiguracional dependente do tempo para bósons (MCT-DHB) é cuidadosamente descrito, fornecendo todas derivações relevantes até as equações finais de movimento, bem como um prospecto para abordagem numérica. Assim sendo, esta tese também trata de tópicos de análise numérica devido a complexidade do método envolvido. Após a derivação do MCTDHB e sua implementação numérica serem mostradas, as propriedades superfluídas de um gás bosônico em geometria anular foram estudadas com a maior generalidade possível proposta na referência [1], sem qualquer suposição sobre o estado de condensação do sistema. Além disso, a capacidade do MCTDHB de fornecer funções de correlação é explorada para caracterizar a perda da fração de superfluido devido a um barreira. Ainda dentro do mesmo objetivo de estudar propriedades de circulação bosônicas em um anel, correntes persistentes também são investigadas, com duas derivações alternativas para condição de meta-estabilidade como um mínimo local para energia. Ademais, o decaimento dinâmico da corrente é analisado após abruptamente introduzir uma barreira como potencial. Flutuações do operador de número e probabilidades são calculadas ao longo da evolução temporal para fornecer informações sobre a distribuição estatística quântica em medidas experimentais, objetivando revelar informações relevantes sobre a observação por imagem de estados com circulação.

Palavras-Chave: método de Hartree multiconfiguracional; sistemas de muitas partículas; bósons; condensação de Bose-Einstein; superfluido.

Acronyms

MCTDHB → Multiconfigurational time-dependent Hartree method for bosons

GP → Gross-Pitaevskii

IPS → Individual particle states

QT → Quantum tunneling

LL → Lieb-Liniger

BEC → Bose-Einstein condensate

TG → Tonks-Girardeau

RDM → Reduced density matrix

Contents

Chapter 1

Introduction

Analytical solutions for quantum many-particle problems rapidly become scarce when a few relevant assumptions are considered, such as interactions among the particles, peculiar trapping potentials or time evolution of non-stationary states. Among the most popular solvable examples are some interacting spin systems in thermal equilibrium present in statistical mechanics textbooks [2,3], but adding the spatial description is a difficult step. For a bosonic system with traslational degree of freedom, an example of analytically solvable model is the Lieb-Liniger(LL) gas [4,5], consisting of bosons confined in a periodic one dimensional space. Despite the many-particle wave function can be obtained for the ground and excited states, the computation of observables is not trivial and requires multi-dimensional integrals of a complicated wave-function, with the dimension given by the number of particles.

After more than fifty years of the LL model has been reported, there is still ongoing research about it, for instance on approximations [6,7] and focusing on a narrow band of the excitation spectrum, to reproduce solitons predicted in the meanfield theory [8], just to mention a few. Besides, the hard core limit(impenetrable particles), which conducts to the Tonks-Girardeau(TG) gas [9,10], has been used in many one-dimensional studies as an upper bound when analyzing the effect of strong interactions [7,11]. The LL model illustrate well that in many-particle physics there are many gaps in our understanding yet to be filled, from the fundamentals of quantum mechanics to collective phenomena, which cannot be thought by reductionism [12], even knowing the many-body wave function.

The importance of collective phenomena, concomitantly with the limitations of analytical approaches, justifies the progressive use of numerical computation, which has became

almost indispensable on present research. Surely, any numerical method employed impose limitations as well, though they generally are far less stiff than a pure analytical approach.

One of the main ingredients of many-particle systems complexity is a reservoir coupling, in general, leading to the consideration of a thermal description. However, progressive improvement in cooling techniques of atoms [13–16] have provided clean and controllable environments to study many-particle systems within a pure state instead of a statistical ensemble description. This is important for both, approximation methods designing and experiments to study fundamental properties of quantum systems. A Bose-Einstein condensate(BEC) [17–21] thus provide the idealization of this scenario, as it exhibits a negligible thermal cloud, depicted in Fig.(1.1).

Even at zero temperature, systems of many identical particles, such as the BEC, are not trivial to deal with. Usually, the second quantization formalism is adopted, in which the type of particle statistics, fermions or bosons, are implied in the commutation relations of operators that raise or decrease by one particle the state, called creation and annihilation operators, respectively. Within this framework, an exact approach would require a complete set of Individual Particle States(IPS), also named orbitals[1], which the particles can occupy through the action of the operators. All these elements yield the number occupation basis of many-particle systems, also called Fock basis, which of course is of infinite dimension and thus imply the first issue to approach the problem with numerical methods. To overcome this drawback, the Hilbert space must be truncated. This IPS basis truncation and the spanned Fock basis of occupation numbers are the core elements of multiconfigurational methods.

---

[1]Methods employed here are also used in chemistry, from which came the designation of orbitals used in the study of molecules.
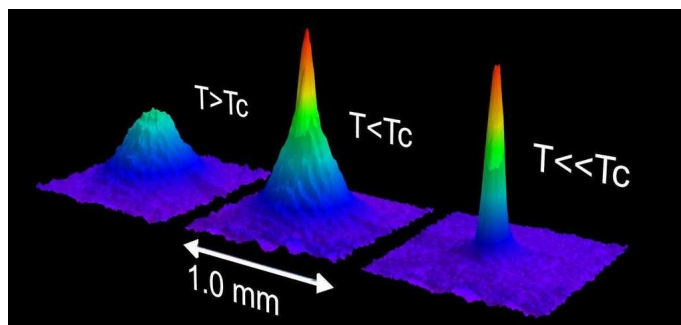
Figure 1.1: Bose-Einstein condensation. Examples of atomic densities in three regimes around the transition temperature. Figure taken from Ref. [22]

As shall become clearer throughout this thesis, the truncation of many-particle system Hilbert space is suitable because it offers an approach which can be progressively improved, by raising the space dimension, differently from other methods that impose inflexible constraints from the beginning, as is the case of meanfield description.

1.1 Multiconfigurational approach

Generally, a system of particles coupled to an complicated external environment can be described by a density matrix, which the time-evolution is determined by a master equation after tracing out the environment [23, 24]. A simpler case is the thermal equilibrium with the environment, where the density matrix is represented by the statistical ensemble theory, which is strictly defined in terms of the Hamiltonian of the system and Lagrange multipliers [2, 3]. As the temperature decreases, the density matrix approach asymptotically a projector operator to the many-particle ground state, that is, a pure state, as all excited states probabilities goes to zero, regardless of the particle type, bosons or fermions. Therefore, at low enough temperature, the many-particle system can be well approximated by a pure state, which is the starting point for the intended numerical approach envisaged in the previous section.

In the case of fermions, the anticommutation of their creation and annihilation operators, which implies the antisymmetry of the wave function under permutations of the particles, prohibit more than one occupation per IPS, spreading the occupations requiring at least the same number of particles for the IPS. The bosons, instead, allow for simultaneous occupation, and decreasing the temperature, typically concentrate particles in the IPS with lowest single particle energy. Actually, for an ideal bose gas, all the particles shall occupy the lowest energy single particle state in the system's ground state[2]. Therefore, in ultracold many-particle systems, even for a large number of particles a small number of IPS can be enough to describe bosons, while fermions restrict the analysis to fewer particle numbers.

The arbitrariness of the IPS can be solved imposing a variational method to minimize the many-body action, occasionally including time dependence, which would provide the most efficient spanned space to the problem, either to study dynamics or stationary states.

---

[2]Considering there are no degeneracies for the many-particle ground state

This variational approach often yield the optimal IPS basis to the problem instead of a particular choice. All these elements are part of the multiconfigurational time-Dependent Hartree method(MCTDH), which started to be investigated firstly in molecular dynamics in chemistry [25–29], though not necessarily including a formalism for identical particles. Later, it was adopted in physics to describe systems of identical particles, first bosons [30] and later fermions [31]. Since then, several studies were performed including comparison to theoretical models [32,33], quench dynamics [34–42], fermions [43–47], quantum information [34, 36] and condensate fragmentation [48–52]. Throughout this thesis, systems of bosons are studied within Multiconfigurational Time Dependent Hartree Method for Bosons(MCTDHB).

In contrast to the variational approach of MCTDHB, for some specific systems, the IPS may be fixed to work just in the configuratinal space with diagonalization techniques [53,54], reducing the numerical effort, for instance using momentum basis in translational invariant systems, or in the Bose-Hubbard model, where the IPS do not even need to be specified, requiring only two numerical parameters instead, for neighbors site tunneling and in-site interaction. Differently, in trapped systems, specially the ones with no symmetry or in time dependent problems, the variational approach to the IPS show advantages over a fixed choice [32].

Despite the general formulation with an arbitrary number of IPS mentioned so far, in some occasions only one function is enough for the description, known as the meanfield or macroscopic wave-function, and in this case it describes a BEC [20]. Many criteria for Bose-Einstein condensation were studied over the time since the first formulation for ideal gases [17, 18], which was generalized for interacting cases [55] and proved in the dilute-limit [56,57]. Apart from the specific criteria for the validity and limitations of meanfield description, since the first observation of BEC [19] it has been undoubtedly useful in connection with most part of the experiments, at least providing assistant results for dilute and weakly interacting limit.

A remarkable property of the MCTDHB is the containment of meanfield as a special case, providing an easy way to compare results from both approaches. Therefore, the number of IPS can be viewed as a straightforward generalization of meanfield description, which can offer progressive improvement in calculations as it is increased, eventually, until a convergence criterion is achieved.

1.2   Beyond meanfield features

One of the main purposes of the MCTDHB, besides the improving accuracy in the many-particle state, is the accessibility to observables absent in the meanfield description, the most important ones being the spatial mutual probability functions(also known as correlations) and fragmentation in dynamics of nonstationary states. These key features are related to the general definition of the p-order Reduced Density Matrix($p-$RDM) [58–61],

$$\rho^{(p)}(\mathbf{x}_1, ..., \mathbf{x}_p | \mathbf{x}'_1, ..., \mathbf{x}'_p) = \left\langle \prod_{i=1}^{p} \hat{\Psi}^{\dagger}(\mathbf{x}'_i) \prod_{j=1}^{p} \hat{\Psi}(\mathbf{x}_i) \right\rangle \frac{(N-p)!}{N!} \ , \qquad (1.1)$$

where the brackets $\langle . \rangle$ denote the average with respect to a many-particle state. As will be shown in the following chapters, the $p-$RDM can also be related to the many-body wave-function

$$\rho^{(p)}(\mathbf{x}_1, ..., \mathbf{x}_p | \mathbf{x}'_1, ..., \mathbf{x}'_p) = \int \left(\prod_{i=p+1}^{N} \mathrm{d}\mathbf{x}_i \right) \Psi^*(\mathbf{x}'_1, ..., \mathbf{x}'_p, \mathbf{x}_{p+1}, ..., \mathbf{x}_N) \Psi(\mathbf{x}_1, ..., \mathbf{x}_N) \ . \quad (1.2)$$

This form is particularly useful to see the relation with mutual probabilities by setting the primed variables equal to the unprimed ones, which are important in understanding the density measurement of a bosonic gas [59].

In meanfield description, the mutual probability obtained from Eq. (1.2) with $\mathbf{x}'_k = \mathbf{x}_k$ for all $k \in \{1, ..., p\}$ is rather meaningless since it is reduced to the $p-$product of the modulus squared of a single function, which translates to the mutual probability of independent events of measuring particles in the respective positions. Moreover, any single particle property holds information about all the other particles, and thus, the meanfield description lacks correlation information about the many-particle system.

In addition, the $1-$RDM provide special information since it can be used to define the condensation fraction according to Penrose-Onsager criterion [55]. The possibility to compute it at any time instant of the many-particle state evolution presents one of the major advantages of the MCTDHB when compared to other alternative methods.

As a final introductory remark on the advantages of the MCTDHB, we have the possibility to decouple some concepts as condensation and superfluidity for an arbitrary many-particle state [1]. As pointed out by Leggett [62] using the example of liquid ^{4}He, one concept does not imply the other, and with a method capable to tackle many-particle

properties, we are able to study superfluid fraction through the moment of inertia [1,63,64].

1.3   Thesis outline

In this project, some applications of the MCTDHB are evaluated and contrasted with the meanfield results whenever possible, highlighting the beyond meanfield behavior of many-particle systems in one dimension. The main focus is to study many-body effects absent in the meanfield theory and to obtain more accurate results in stronger interaction regimes, specially analyzing the $p-$RDM [61], which introduces the general concept of condensation fraction [55] and provide correlation functions. Furthermore, the numerical solution of MCTDHB equations can provide important features about many-particle physics until now not fully understood and serve as basis for new experiments in a wider variety of conditions than previously possible.

In the following, chapter 2 is devoted to analytical derivation of multiconfigurational methods and Bose-Einstein condensation. In chapter 3, some particular details of MCT-DHB numerical implementation is presented, emphasizing the memory allocation and numerical representation of the multiconfigurational space elements. A study on the performance of the implementation used here was evaluated with an additional analysis of the parallelized codes [65]. Chapter 4 summarize some important results analyzed with MCTDHB. Essentially, a work on superfluid fraction of few bosons in annular geometry published in Physical Review A journal [64] is revisited, extending it with dynamical studies about superfluid fraction and persistent currents on a ring trapped gas. Finally, the conclusions and further perspectives are presented in chapter 5.

Chapter 2

Multiconfigurational time-dependent Hartree method

An introduction to the MCTDHB is easier provided in the second quantization framework, since the many-particle state is automatically symmetric due to the commutation relations of creation and annihilation operators. Some traditional quantum mechanics books provide a comprehensive introduction to the theme [66,67], thus, this chapter starts with a brief and not so rigorous review of the main concepts, aiming self containment. Therefore, starting from the second quantization formalism, time-dependent IPS are introduced and used as moving basis for the variational approach in the many-body action. After deriving the equations of motion for the IPS and coefficients of Fock basis expansion, discussions about Bose-Einstein condensation and beyond meanfield observables are addressed.

2.1   Symmetrization of states for identical particles

For justification of the operators commutation relations for bosons and fermions, we can start from the usual way to write a many-particle Hamiltonian with tensor products of operators for each particle.

Suppose, for simplicity, a two-level Hamiltonian for two particles as

$$H = \frac{\epsilon}{2}(\mathbb{1}_2 \otimes \sigma_z + \sigma_z \otimes \mathbb{1}_2) \tag{2.1}$$

where $\mathbb{1}_2$ is the 2x2 identity matrix and

$$
\sigma_z = \begin{pmatrix} 1 & 0 \\ 0 & -1 \end{pmatrix}, \tag{2.2}
$$

is the third Pauli matrix. The most convenient basis, in a first moment, is given by σ_z eigenstates, namely $|\chi_+\rangle$ and $|\chi_-\rangle$, which satisfy $\sigma_z|\chi_\pm\rangle = \pm 1$. Therefore, the basis for the composed system of two particles can be written in the lexicographic ordering as

$$
\{|\chi_+\rangle \otimes |\chi_+\rangle, |\chi_+\rangle \otimes |\chi_-\rangle, |\chi_-\rangle \otimes |\chi_+\rangle, |\chi_-\rangle \otimes |\chi_-\rangle\}, \tag{2.3}
$$

which are all eigenstates of the model example in Eq. (2.1).

For simplicity, the tensor product sign $\otimes$ is usually omitted, and product states are simply written as $|\chi_a\rangle \otimes |\chi_b\rangle \equiv |\chi_a, \chi_b\rangle$. Thus, the operators are indexed as $A \otimes B \equiv A^{(1)}B^{(2)}$ to indicate in which space they act. This convention is adopted for the next passages.

Nonetheless, for indistinguishable particles, we must additionally require that the two-particle state is invariant under permutation, otherwise we would be able to label the particles in the system, causing an inconsistency with the first assumption. For instance, the overlaps $\langle \chi_a, \chi_b|\Psi\rangle$ and $\langle \chi_b, \chi_a|\Psi\rangle$ must be identical for any two-particle state $|\Psi\rangle$ representing indistinguishable particles. With that noted, we cannot take arbitrary combinations of the states $|\chi_+, \chi_-\rangle$ and $|\chi_-, \chi_+\rangle$ in $|\Psi\rangle$ definition, but instead have constrained combinations to respect the indistinguishability. Equivalently, we must require that $|\Psi\rangle$ is eigenstate of the permutation operator P_{12}.

The permutation operator P_{12} have the property $P_{12}^2 = \mathbb{1}_4$, which implies that its eigenvalues are $\lambda_\pm = \pm 1$. Therefore, for any indistinguishable state of two particles $|\Psi\rangle$, we must choose one of the two sings in $\lambda_\pm$ to have as eigenvalue for $|\Psi\rangle$, that is, $P_{12}|\Psi\rangle = +|\Psi\rangle$ or $P_{12}|\Psi\rangle = -|\Psi\rangle$, which lead us to define two classes of particles, symmetric or antisymmetric under permutations, that characterize bosons and fermions, respectively.

However, the basis introduced in the set (2.3) does not follow the requirements for

indistinguishable particles. By representing the projector operator in this basis yields

$$P_{12} = \begin{pmatrix} 1 & 0 & 0 & 0 \\ 0 & 0 & 1 & 0 \\ 0 & 1 & 0 & 0 \\ 0 & 0 & 0 & 1 \end{pmatrix}, \tag{2.4}$$

which is not diagonal. A suitable basis should only have eigenstates of P_{12}, with one of its eigenvalues, either plus or minus, and thus, any state represented in one of these bases would automatically be eigenstate of P_{12}, with a specific symmetrization rule. In other words, we not only need P_{12} diagonalized, but also separate the sectors with ± 1 eigenvalues.

A basis in which P_{12} is diagonal can be conveniently written as

$$\left\{|\chi_+, \chi_+\rangle, \ (|\chi_+, \chi_-\rangle + |\chi_-, \chi_+\rangle)/\sqrt{2}, \ |\chi_-, \chi_-\rangle\right\} \bigcup \left\{(|\chi_+, \chi_-\rangle - |\chi_-, \chi_+\rangle)/\sqrt{2}\right\}, \tag{2.5}$$

where the left set in the union hold all symmetric states and the right set the antisymmetric ones. As mentioned above, indistinguishable particles must be represented by one of those sets, which give us a prescription to build bases from the default product state basis, by diagonalizing the permutation operator and selecting the symmetric states for bosons and antisymmetric ones for fermions.

For a general system with N spinless[1] particles in free space with D-dimensions of length L, the product basis becomes

$$\Lambda = \left\{|\mathbf{k}_1, ..., \mathbf{k}_N\rangle; \ k_{i_\gamma} = 2\pi n_{i_\gamma}/L, \ i = 1, ..., N, \ \gamma = 1, ..., D\right\}. \tag{2.6}$$

The description of indistinguishable particles requires to convert the basis Λ in such way to have all states as eigenstates of all possible permutation operators P_{ij}. This can be done with (anti)symmetrization operators $(A)S$, whose when applied to a product state

---

[1]Usually the spin degree of freedom is eliminated by polarization, which is many times termed spinless.

yield a sum of all possible permutations of the labels $\mathbf{k}_i$,

$$S|\mathbf{k}_1, ..., \mathbf{k}_N\rangle = \sum_{\mathbf{P}} |\mathbf{k}_{P_1}, ..., \mathbf{k}_{P_N}\rangle, \tag{2.7}$$

$$A|\mathbf{k}_1, ..., \mathbf{k}_N\rangle = \sum_{\mathbf{P}} (-1)^{n(\mathbf{P})} |\mathbf{k}_{P_1}, ..., \mathbf{k}_{P_N}\rangle, \tag{2.8}$$

where $\mathbf{P}$ is a tuple of integer numbers obtained from permutations, such that its components fulfill $1 \leq P_i \leq N$ with no repetitions, and $n(\mathbf{P})$ give us the number of permutations done over the trivial tuple $\tilde{P}_i = i$. The basis for bosons or fermions are thus the outcome of S and A over the states in Λ with a proper normalization factor. However, the states in Λ that are already permutations from others must be ignored to avoid duplications in the outcome of A or S.

The normalization factor for the antisymmetric case is easier to obtain, since in the sum over all permutations, no repetitions of the same state can occur, thus there are $N!$ nonzero scalar products. In the symmetric case, if some $\mathbf{k}_i$ is repeated n_i times, then

$$\sum_{\mathbf{P}} \equiv n_i! \sum_{\mathbf{C}(n_i)} \sum_{\mathbf{P}(N-n_i)}, \tag{2.9}$$

where $\mathbf{C}(n_i)$ is the sum over all different possibilities to sort the equal $\mathbf{k}_i$s, which must have $N!/(n_i!(N-n_i)!)$ terms, and $\mathbf{P}(N-n_i)$ is the sum over permutation of $\mathbf{k}_j$s with $j \neq i$. Therefore, in computing the scalar product we get $N!n_i!$ nonzero cases. The generalization to more subset repetitions is straightforward. In summary, the basis states of an indistinguishable particle system are

$$|\mathbf{k}_1, ..., \mathbf{k}_N\rangle^A = \frac{1}{\sqrt{N!}} A|\mathbf{k}_1, ..., \mathbf{k}_N\rangle, \tag{2.10}$$

$$|\mathbf{k}_1, ..., \mathbf{k}_N\rangle^S = \frac{1}{\sqrt{N!n_1!...n_N!}} S|\mathbf{k}_1, ..., \mathbf{k}_N\rangle, \tag{2.11}$$

excluding a subset of vectors $\{\mathbf{k}_i\}_{i=1,...,N}$ from Eq. (2.6) that are related by permutations to avoid duplications in the outcome of A or S. As result, the basis for identical particles systems are smaller, in agreement with the example in Eq. (2.5), since they are sectors of the set of eigenvalues of permutation operators.

Trace calculation in the symmetrized or antisymmetrized basis must be evaluate carefully, because the sum must be done over necessarily different $|\cdot\rangle^{A,S}$ states, which is not

simply the free sum over all $\mathbf{k}_i$ vectors. Nonetheless, for any operator O,

$$\text{Tr}(O) = \sum_{|\vec{\mathbf{k}}\rangle^{A,S}} {}^{A,S}\langle \mathbf{k}_1, ..., \mathbf{k}_N | O | \mathbf{k}_1, ..., \mathbf{k}_N\rangle^{A,S} =$$

$$\frac{1}{N!} \sum_{\mathbf{k}_1,...,\mathbf{k}_N} (n_1!...n_N!)^{A,S}\langle \mathbf{k}_1, ..., \mathbf{k}_N | O | \mathbf{k}_1, ..., \mathbf{k}_N\rangle^{A,S}, \quad (2.12)$$

since in exchange to sum freely over all $\mathbf{k}_i$s, the permutations of different vectors $\mathbf{k}$s are present in the summation and yield the same result in the symmetrization or antisymmetrization process. Note however, that $N!$ would simply exclude permutations over all vectors, but those that are equal appears only once in the sum, such that we also need the factor $n_1!...n_N!$ for the number of repetitions for each one of $\mathbf{k}_1, ..., \mathbf{k}_N$, respectively, which only affects the symmetric(bosonic) case.

2.1.1   Symmetrization in position space

Linear combinations of states $|\mathbf{k}_1, ..., \mathbf{k}_N\rangle^A$ or $|\mathbf{k}_1, ..., \mathbf{k}_N\rangle^S$ are automatically antisymmetric or symmetric, respectively. Hence, using them as basis for a generic state $|\Psi\rangle^{A,S}$ representation, automatically encodes the symmetrization needed. The product state of localized positions $|\mathbf{x}_1, ..., \mathbf{x}_N\rangle$ can be used to obtain the wave-function corresponding to $|\Psi\rangle^{A,S}$, where any different order chosen in the positions $\mathbf{x}_i$ will only produce an overall sign. As a simple example,

$$\langle \mathbf{x}_1, \mathbf{x}_2 | \left(\frac{|\mathbf{k}_1, \mathbf{k}_2\rangle \pm |\mathbf{k}_2, \mathbf{k}_1\rangle}{\sqrt{2}} \right) = \frac{\phi_{\mathbf{k}_1}(\mathbf{x}_1)\phi_{\mathbf{k}_2}(\mathbf{x}_2) \pm \phi_{\mathbf{k}_2}(\mathbf{x}_1)\phi_{\mathbf{k}_1}(\mathbf{x}_2)}{\sqrt{2}}$$

$$= \pm \left[\frac{\phi_{\mathbf{k}_1}(\mathbf{x}_2)\phi_{\mathbf{k}_2}(\mathbf{x}_1) \pm \phi_{\mathbf{k}_2}(\mathbf{x}_2)\phi_{\mathbf{k}_1}(\mathbf{x}_1)}{\sqrt{2}} \right]$$

$$= \pm \langle \mathbf{x}_2, \mathbf{x}_1 | \left(\frac{|\mathbf{k}_1, \mathbf{k}_2\rangle \pm |\mathbf{k}_2, \mathbf{k}_1\rangle}{\sqrt{2}} \right), \quad (2.13)$$

which demonstrate that no additional permutations are required in the positions. Finally,

$$\psi^{(A,S)}(\mathbf{x}_1, ..., \mathbf{x}_N) = \langle \mathbf{x}_1, ..., \mathbf{x}_N | \Psi\rangle^{A,S} \quad (2.14)$$

is the corresponding wave-function, where $|\Psi\rangle^{A,S}$ is any normalized linear combination of states of the either (2.10) or (2.11). Therefore, $\psi^{(A,S)}$ is either symmetric or antisymmetric under permutations of its arguments.

As a final important remark, the symmetrization of the states can be done directly with the wave function basis states, as shown between steps of Eq. (2.13), where there is no actual difference in choosing for the permutation of positions($\mathbf{x}_i$) or state labels($\mathbf{k}_i$). These permutations can be conveniently written as determinants for the antisymmetric case and permanents for the symmetric case, whereas the first is known as Slater determinant [66, 68].

2.1.2   Effect of symmetrization for bosons and fermions

An illustrative example of indistinguishability implications is a system with two ideal particles in free space, which is the smallest system to provide simple yet useful information. The Hamiltonian is given by

$$H = \frac{\mathbf{p}_1^2}{2m} + \frac{\mathbf{p}_2^2}{2m}.$$
(2.15)

This system at thermal equilibrium have as density matrix

$$\rho_T^{A,S} = \frac{e^{-\beta H}}{Z^{A,S}}, \ Z^{A,S} = \mathrm{Tr}_{A,S}(e^{-\beta H}),$$
(2.16)

with $Z^{A,S}$ being the canonical partition function, whereas the probability to have the system at some arbitrary state $|\Psi\rangle$ is $\mathrm{Tr}_{A,S}(|\Psi\rangle\langle\Psi|\rho_T^{A,S}) = \langle\Psi|\rho_T^{A,S}|\Psi\rangle$. For the partition function, the trace yields

$$Z^{A,S} = \frac{1}{2!} \sum_{\mathbf{k}_1\mathbf{k}_2} \frac{1}{\sqrt{2!}} \Big(\langle\mathbf{k}_1, \mathbf{k}_2| \pm \langle\mathbf{k}_2, \mathbf{k}_1| \Big) \exp\left(-\frac{\beta\hbar^2}{2m}(\mathbf{k}_1^2 + \mathbf{k}_2^2) \right) \frac{1}{\sqrt{2!}} \Big(|\mathbf{k}_1, \mathbf{k}_2\rangle \pm |\mathbf{k}_2, \mathbf{k}_1\rangle \Big),$$
(2.17)

where the plus sign indicate the symmetric(S) case and minus the antisymmetric(A) one.

$$\begin{aligned}
Z^{A,S} &= \frac{1}{2} \sum_{\mathbf{k}_1\mathbf{k}_2} \exp\left(-\frac{\beta\hbar^2}{2m}(\mathbf{k}_1^2 + \mathbf{k}_2^2) \right) \Big(1 \pm \delta_{\mathbf{k}_1\mathbf{k}_2} \Big) \\
&= \frac{1}{2} \sum_{\mathbf{k}_1\mathbf{k}_2} \exp\left(-\frac{\beta\hbar^2}{2m}(\mathbf{k}_1^2 + \mathbf{k}_2^2) \right) \pm \frac{1}{2} \sum_{\mathbf{k}} \exp\left(-\frac{\beta\hbar^2\mathbf{k}^2}{m} \right).
\end{aligned}$$
(2.18)

The first term in this last equation is just the usual partition function without considering identical particles divided by 2, and the second term incorporates the symmetry property. Considering a very large dimension length L, the sums are approximated by integrals,

and

$$Z^{A,S} = \frac{1}{2}\left(\frac{L}{2\pi}\right)^{2D}\int d\mathbf{k}_1 d\mathbf{k}_2 \exp\left(-\frac{\beta\hbar^2}{2m}(\mathbf{k}_1^2 + \mathbf{k}_2^2)\right) \pm \frac{1}{2}\left(\frac{L}{2\pi}\right)^{D}\int d\mathbf{k} \exp\left(-\frac{\beta\hbar^2\mathbf{k}^2}{m}\right), \quad (2.19)$$

which are simply gaussian integrals and yields

$$Z^{A,S} = \frac{1}{2}\left(\frac{L}{2\pi}\right)^{2D}\left(\frac{2m\pi}{\beta\hbar^2}\right)^{D} \pm \frac{1}{2}\left(\frac{L}{2\pi}\right)^{D}\left(\frac{m\pi}{\beta\hbar^2}\right)^{D/2},$$

$$Z^{A,S} = \frac{1}{2}\left(\frac{L}{\lambda_T}\right)^{2D}\left[1 \pm \left(\frac{\lambda_T}{\sqrt{2}L}\right)^{D}\right], \quad (2.20)$$

where

$$\lambda_T = \left(\frac{h^2}{2\pi m k_B T}\right)^{1/2}, \quad (2.21)$$

is the DeBroglie thermal wavelength. Clearly, the symmetrization correction term with $\pm$ sign is negligible for large systems and high temperatures, as $\lim_{T\to\infty}\lambda_T = 0$. So ultracold gases are suitable to explore these differences brought by identical particles consideration.

The conversion of the sum to an integral requires that the exponential in Eq. (2.18) varies smoothly in the discrete steps of momentum, thereby, the decay imposed by its argument cannot be abrupt. In this case, using the momentum minimal step $\delta_k = 2\pi/L$ for validation of the above calculations, the relation

$$\frac{\beta\hbar^2}{m}\delta_k^2 = \left(\frac{\sqrt{2\pi}\lambda_T}{L}\right)^2 \ll 1, \quad (2.22)$$

must be valid.

Another interesting property is the probability density distribution of these two particles, to see the impact, if there is any, of the symmetrization properties. Therefore, we need to calculate $\langle\mathbf{r}_1, \mathbf{r}_2|\rho_T^{A,S}|\mathbf{r}_1, \mathbf{r}_2\rangle$, which as discussed in the last section, the coordinates states are simple products without symmetrization, since it is already incorporated in the basis.

$$\text{Tr}_{A,S}\left(|\mathbf{r}_1, \mathbf{r}_2\rangle\langle\mathbf{r}_1, \mathbf{r}_2|e^{-\beta H}\right) = \sum_{|\mathbf{k}_1\mathbf{k}_2\rangle^{A,S}}\left|\langle\mathbf{r}_1, \mathbf{r}_2|\mathbf{k}_1\mathbf{k}_2\rangle^{A,S}\right|^2 \exp\left(-\frac{\beta\hbar^2}{2m}(\mathbf{k}_1^2 + \mathbf{k}_2^2)\right)$$

$$= \frac{1}{2L^{2D}}\sum_{\mathbf{k}_1\mathbf{k}_2}\left\{\exp\left(-\frac{\beta\hbar^2}{2m}(\mathbf{k}_1^2 + \mathbf{k}_2^2)\right) \pm \frac{1}{2}\left[f(\mathbf{k}_1, \mathbf{k}_2) + f(\mathbf{k}_1, \mathbf{k}_2)^*\right]\right\}, \quad (2.23)$$

where

$$f(\mathbf{k}_1, \mathbf{k}_2) = \exp\left[i\mathbf{k}_1 \cdot (\mathbf{r}_1 - \mathbf{r}_2) + i\mathbf{k}_2 \cdot (\mathbf{r}_2 - \mathbf{r}_1) - \frac{\beta\hbar^2}{2m}(\mathbf{k}_1^2 + \mathbf{k}_2^2)\right]. \qquad (2.24)$$

With the same assumption as before, to justify the integration replacing the sum, we must use the a Fourier transformation of a gaussian to obtain

$$\int d\mathbf{k}_1 d\mathbf{k}_2 f(\mathbf{k}_1, \mathbf{k}_2) = \left(\frac{2\pi m}{\beta\hbar^2}\right)^D \exp\left(\frac{m}{\beta\hbar^2}(\mathbf{r}_2 - \mathbf{r}_1)^2\right). \qquad (2.25)$$

Gathering the results of the gaussian integrals with Eqs. (2.16, 2.23) yield

$$\langle \mathbf{r}_1, \mathbf{r}_2 | \rho_T^{A,S} | \mathbf{r}_1, \mathbf{r}_2 \rangle = \frac{1}{2Z^{A,S}(\lambda_T)^{2D}}\left[1 \pm e^{-2\pi(\mathbf{r}_1 - \mathbf{r}_2)^2/\lambda_T^2}\right]. \qquad (2.26)$$

This result clearly show the difference between bosons and fermions, as bosons have greater probability to be found near each other for $|\mathbf{r}_2 - \mathbf{r}_1| \lesssim \lambda_T$, and for fermions this probability decreases to 0 when $\mathbf{r}_2 = \mathbf{r}_1$.

2.2   Number occupation basis: second quantization

The approach presented in the previous section rapidly increases its complexity as the number of particles is raised, and working with an arbitrary number of particles can become rather cumbersome. Within this scenario, the second quantization formalism is very convenient in reducing many-particle systems complexity.

One important thing to note from Eqs. (2.10, 2.11) is the impossible single particle labeling as result of the permutations, with either positive or negative signs, where the single particle labels can be of any type.[2] However, it is still possible to infer the number of particles sharing the same label without identifying them, due to the way the states in Eqs. (2.10, 2.11) are constructed, starting from a known product state with specific labels. Therefore, by construction, we have a correspondence of

$$|\mathbf{k}_1, ..., \mathbf{k}_N\rangle^{A,S} \to |n_1, ..., n_i, ...\rangle, \qquad (2.27)$$

for a new basis which only the number of particles for each label is used, known as Fock basis.

---

[2]Although in the previous section the momentum was used to workout a specific example.

The many-particle operators must follow an equivalent mapping, defining the action rules in this new basis. For instance, a Hamiltonian should be mapped as

$$H = \sum_{i=1}^{N} \left[h(\mathbf{r}_i, \mathbf{p}_i) + \sum_{j>i} V(\mathbf{r}_i, \mathbf{r}_j) \right] \rightarrow \hat{H}, \tag{2.28}$$

where the $\hat{H}$ indicate the version acting on Fock states.

Before working out this mapping for the operators, a basic starting point is the investigation of Fock states $|n_1, ..., n_i, ...\rangle$, providing their construction process and most important features. In the following, we start from the simplest assumption of all n_i being positive integers and by analogy with quantum harmonic oscillator [66] two possible algebras are derived, one for bosons (symmetric case) and other for fermions (antisymmetric).

2.2.1   Creation and annihilation operators

Let $|\Psi(n_j)\rangle$ be a many-particle state which has at least one well defined occupation eigenvalue, n_j, representing the number of particles in a particular labeled IPS j. Therefore, the annihilation operator in this state j must satisfy

$$\hat{a}_j |\Psi(n_j)\rangle = c(n_j)|\Psi(n_j - 1)\rangle, \tag{2.29}$$

consequently, there is a commutation relation with the number operator specified by

$$[\hat{a}_j, \hat{n}_j] = \hat{a}_j, \tag{2.30}$$

and using the adjoint in both sides yield

$$[\hat{n}_j, \hat{a}_j^\dagger] = \hat{a}_j^\dagger. \tag{2.31}$$

This last commutation rule also implies

$$\hat{a}_j^\dagger |\Psi(n_j)\rangle = d(n_j)|\Psi(n_j + 1)\rangle. \tag{2.32}$$

Combining the results from Eqs. (2.29, 2.32), the constants $c(n_j)$ and $d(n_j)$ can be

chosen such that $\hat{a}_j^\dagger \hat{a}_j |\Psi(n_j)\rangle = n_j |\Psi(n_j)\rangle$. Therefore, the number operator can be written as

$$\hat{n}_j = \hat{a}_j^\dagger \hat{a}_j, \tag{2.33}$$

provided that the constants are $c(n_j) = \sqrt{n_j}$ and $d(n_j) = \sqrt{n_j + 1}$.

Another inspection in Eq. (2.30), show two different ways to expand the commutator as

$$[\hat{a}_j, \hat{a}_j^\dagger \hat{a}_j] = [\hat{a}_j, \hat{a}_j^\dagger]\hat{a}_j, \tag{2.34}$$

$$[\hat{a}_j, \hat{a}_j^\dagger \hat{a}_j] = \{\hat{a}_j, \hat{a}_j^\dagger\}\hat{a}_j - \hat{a}_j^\dagger \{\hat{a}_j, \hat{a}_j\}. \tag{2.35}$$

These formulas reveal two possible algebras for the creation and annihilation operators, the first requires $[\hat{a}_j, \hat{a}_j^\dagger] = 1$, while the second $\{\hat{a}_j, \hat{a}_j^\dagger\} = 1$ and $\hat{a}_j^2 = 0$. Remarkably, the one involving the anticommutator describes fermions as double annihilation automatically produces zero, while the former is suitable for bosons since resembles the quantum harmonic oscillator and allow for arbitrary positive integer numbers in any IPS j.

The complete set of commutation relation is obtained based on arguments that the sequential action of two operator involving different IPS shall produce equivalent states by changing the ordering [66], which implies

$$\hat{a}_j \hat{a}_i |\Psi\rangle = \lambda \hat{a}_i \hat{a}_j |\Psi\rangle, \tag{2.36}$$

$$\hat{a}_j^\dagger \hat{a}_i |\Psi\rangle = \lambda \hat{a}_i \hat{a}_j^\dagger |\Psi\rangle, \tag{2.37}$$

$$\hat{a}_j^\dagger \hat{a}_i^\dagger |\Psi\rangle = \lambda \hat{a}_i^\dagger \hat{a}_j^\dagger |\Psi\rangle, \tag{2.38}$$

for $i \neq j$. As the difference between the sides of the equations above are only permutations of the initial ordering, then $\lambda = -1$ for fermions and $\lambda = +1$ for bosons. Finally, the set of commutation relation becomes either

$$\left[\hat{a}_j, \hat{a}_i^\dagger\right] = \delta_{ij}, \quad \left[\hat{a}_j, \hat{a}_i\right] = 0, \tag{2.39}$$

for bosons or

$$\left\{\hat{a}_j, \hat{a}_i^\dagger\right\} = \delta_{ij}, \quad \left\{\hat{a}_j, \hat{a}_i\right\} = 0, \tag{2.40}$$

for fermions.

As can be anticipated, the IPS which the set of operators for creation and annihilation corresponds is still arbitrary, although must satisfy the completeness relation. As a final remark, it is worth to note that the occupation number states defined in the mapping (2.27) can be build from the vacuum state with

$$|n_1, ..., n_i, ...\rangle = \prod_i \frac{\left(\hat{a}_i^\dagger\right)^{n_i}}{\sqrt{n_i!}} |\mathbf{0}\rangle, \tag{2.41}$$

where the vacuum state $|\mathbf{0}\rangle$ return zero under action of any annihilation operator. For fermions, n_i can only be 0 or 1, thus, the factorials in denominator are usually omitted. In addition, fermions require a convention in the operator ordering in Eq. (2.41) that must be self-consistently followed.

The total number of particles operator is straightforward defined as

$$\hat{N} = \sum_i \hat{a}_i^\dagger \hat{a}_i, \tag{2.42}$$

which as will be shown later is independent of the IPS basis of the operators $\hat{a}_i$.

2.2.2 Basis conversion and field operator

Usually a suitable basis for a specific problem is not known explicitly but through a transformation of another. This is the case, for example, of the quantum harmonic oscillator subject to external forces, where a relevant basis to the problem is build with coherent states [68]. If two individual particle basis are available, $\{|\psi_k\rangle\}_k$ and $\{|\phi_j\rangle\}_j$, they are related by the unitary transformation matrix U, with $U_{jk} = \langle\psi_k|\phi_j\rangle$, such that $|\phi_j\rangle = \sum_k U_{jk}|\psi_k\rangle$ and $|\psi_k\rangle = \sum_j U_{jk}^*|\phi_j\rangle$. Therefore, a given IPS in one basis must be a superposition of states in the other basis, and that must imply the same when creating a particle in the second quantization formalism. Then, the relation for the operators are

$$\hat{a}_k^\dagger = \sum_j U_{jk}^* \hat{b}_j^\dagger = \sum_j \langle\phi_j|\psi_k\rangle \hat{b}_j^\dagger, \tag{2.43}$$

$$\hat{a}_k = \sum_j U_{jk} \hat{b}_j = \sum_j \langle\psi_k|\phi_j\rangle \hat{b}_j, \tag{2.44}$$

with $\hat{a}_k$ and $\hat{b}_k$ related to $|\psi_k\rangle$ and $|\phi_k\rangle$ respectively.

This operator basis expansion is a recurrent tool to represent a BEC in meanfield

approach. In the general case, there is a time-dependent creation operator related to the state the condensation occurs, usually represented by the $0-$indexed pair $\hat{a}_0^\dagger(t)$ for the operator and $|\psi_0(t)\rangle$ for the condensate wave-function. However, once there is a static complete individual particle basis for the problem, namely $\{|\phi_j\rangle\}_j$, the many-particle BEC state is

$$|\Psi_0(t)\rangle = \frac{\left(\hat{a}_0^\dagger(t)\right)^N}{\sqrt{N!}}|\mathbf{0}\rangle = \frac{1}{\sqrt{N!}}\left(\sum_j\langle\phi_j|\psi_0(t)\rangle\hat{b}_j^\dagger\right)^N|\mathbf{0}\rangle, \qquad (2.45)$$

at any time instant t. This expansion often appears in approximations imposing a truncation of the coefficients $c_j(t) = \langle\phi_j|\psi_0(t)\rangle$ when only a finite number of IPS are relevant in the expansion [69–71].

The Eqs. (2.43, 2.44) can also be used with position eigenstates, substituting $j \to \mathbf{x}$ with the required adaptations, for instance, changing the sum to an integral and $|\phi_j\rangle \to |\mathbf{x}\rangle$. Usually, instead of writing $\hat{b}_\mathbf{x}$, $\hat{\Psi}(\mathbf{x}) \equiv \hat{b}_\mathbf{x}$ is introduced and

$$\hat{a}_k = \int d\mathbf{x}\,\psi_k(\mathbf{x})^*\hat{\Psi}(\mathbf{x}). \qquad (2.46)$$

Using the completeness relation in spatial coordinates space, $\sum_k \psi_k(\mathbf{x}')\psi_k(\mathbf{x})^* = \delta(\mathbf{x}-\mathbf{x}')$, yields

$$\hat{\Psi}(\mathbf{x}) = \sum_k \psi_k(\mathbf{x})\hat{a}_k. \qquad (2.47)$$

Eq. (2.47) is usually the origin of the so called second quantization formalism, since seems like an ordinary wave-function expansion though the coefficients are replaced by operators acting on Fock basis.

These derivations can also consider a time-dependent individual particle basis, provided that the states are mutually orthogonal and the completeness relation hold for any instant. This will be required in the derivation of the MCTDHB.

Finally, the commutation or anticommutation relations are readily obtained using either Eq. (2.39) or Eq. (2.40) with Eq. (2.47), respectively. Therefore,

$$[\hat{\Psi}(\mathbf{x}), \hat{\Psi}^\dagger(\mathbf{x}')] = \delta(\mathbf{x} - \mathbf{x}'), \quad [\hat{\Psi}(\mathbf{x}), \hat{\Psi}(\mathbf{x}')] = 0, \qquad (2.48)$$

for bosons and

$$\{\hat{\Psi}(\mathbf{x}), \hat{\Psi}^\dagger(\mathbf{x}')\} = \delta(\mathbf{x} - \mathbf{x}'), \quad \{\hat{\Psi}(\mathbf{x}), \hat{\Psi}(\mathbf{x}')\} = 0, \qquad (2.49)$$

for fermions.

The basis conversions rules derived here show an interesting result when used in the total number operator, defined in Eq. (2.42). Substituting Eqs. (2.43, 2.44) in Eq. (2.42) yield

$$
\begin{aligned}
\hat{N} &= \sum_k \left[\left(\sum_j \langle \phi_j | \psi_k \rangle \hat{b}_j^\dagger \right) \left(\sum_i \langle \psi_k | \phi_i \rangle \hat{b}_i \right) \right] \\
&= \sum_{ij} \left[\langle \phi_j | \left(\sum_k | \psi_k \rangle \langle \psi_k | \right) | \phi_i \rangle \hat{b}_j^\dagger \hat{b}_i \right] \\
&= \sum_i \hat{b}_i^\dagger \hat{b}_i,
\end{aligned}
\tag{2.50}
$$

where the completeness relation and orthogonality of the IPS were assumed. Additionally, similar calculations using the conversion relation for the field operator in Eq. (2.46) imply

$$
\hat{N} = \int \mathrm{d}\mathbf{x} \hat{\Psi}^\dagger(\mathbf{x}) \hat{\Psi}(\mathbf{x}).
\tag{2.51}
$$

2.2.3   Many-body wave function through field operators

The wave-function, by definition, must satisfy the many-body Schrödinger equation of the system, hence, to obtain it from the second quantization formalism, there must be a scalar function of N variables, $\psi(\mathbf{x}_1, ..., \mathbf{x}_N)$, that is either symmetric or antisymmetric under the bosonic or fermionic commutation rules respectively, summarized by Eqs. (2.48, 2.49). The function

$$
\psi(\mathbf{x}_1, ..., \mathbf{x}_N; t) = \frac{1}{\sqrt{N!}} \langle \mathbf{0} | \hat{\Psi}(\mathbf{x}_1) \hat{\Psi}(\mathbf{x}_2) ... \hat{\Psi}(\mathbf{x}_N) | \Psi^{(N)}; t \rangle,
\tag{2.52}
$$

is the one to fulfill the requirements, as shown in Ref. [66]. Moreover, a reciprocal version to obtain the state $|\Psi^{(N)}\rangle$ from the many-body wave function is

$$
|\Psi^{(N)}; t \rangle = \int \left(\prod_{i=1}^N \mathrm{d}\mathbf{x}_i \right) \frac{1}{\sqrt{N!}} \hat{\Psi}^\dagger(\mathbf{x}_N) ... \hat{\Psi}^\dagger(\mathbf{x}_2) \hat{\Psi}^\dagger(\mathbf{x}_1) | \mathbf{0} \rangle \psi(\mathbf{x}_1, \mathbf{x}_2, ..., \mathbf{x}_N; t).
\tag{2.53}
$$

The Eqs. (2.52, 2.53) demand an ordering convention when working with fermions, as already mentioned before in the definition of Fock states. Nonetheless, in this way written here, both equations are valid for bosons and fermions [66].

2.2.4   n-point Green's function relation to the wave-function

The Eqs. (2.52, 2.53) can also be used to prove the compatibility of operators introduced in the second quantization formalism, for instance, by reproducing the known formulas with the many-body wave function. For this compatibility proof, the expression

$$\langle \Psi_A^{(N)}; t | \Psi^\dagger(\mathbf{y}_1') ... \Psi^\dagger(\mathbf{y}_n') W(\mathbf{y}_1', ..., \mathbf{y}_n'; \mathbf{x}_n', ..., \mathbf{x}_1') \Psi(\mathbf{x}_n') \Psi(\mathbf{x}_1') | \Psi_B^{(N)}; t \rangle, \qquad (2.54)$$

for a general n-body operator density plays an important role. Moreover, if $W = 1$, this expression has crucial importance in the interpretation of reduced density matrices and correlation functions, as will be discussed later. Usually, when $W = 1$ this expression is also named $n-$point Green's function.

In order to show the relation of Eq. (2.54) to the system's wave-function, let $|\Phi^{(N-1)}\rangle = \hat{\Psi}(\mathbf{x}_1')|\Psi^{(N)}\rangle$ represent a generic state, omitting for simplicity the time dependence. Using Eq. (2.53),

$$|\Phi^{(N-1)}\rangle = \int \left(\prod_{i=1}^{N} d\mathbf{x}_i \right) \frac{1}{\sqrt{N!}} \hat{\Psi}(\mathbf{x}_1') \hat{\Psi}^\dagger(\mathbf{x}_N) ... \hat{\Psi}^\dagger(\mathbf{x}_2) \hat{\Psi}^\dagger(\mathbf{x}_1) |0\rangle \psi(\mathbf{x}_1, \mathbf{x}_2, ..., \mathbf{x}_N). \quad (2.55)$$

Following one of the commutation rules of Eq. (2.48) or Eq. (2.49),

$$\hat{\Psi}(\mathbf{x}_1') \hat{\Psi}^\dagger(\mathbf{x}_N) ... \hat{\Psi}^\dagger(\mathbf{x}_2) \hat{\Psi}^\dagger(\mathbf{x}_1) |0\rangle = \left(\delta(\mathbf{x}_1' - \mathbf{x}_N) \pm \hat{\Psi}^\dagger(\mathbf{x}_N) \hat{\Psi}(\mathbf{x}_1') \right) ... \hat{\Psi}^\dagger(\mathbf{x}_2) \hat{\Psi}^\dagger(\mathbf{x}_1) |0\rangle$$

$$= \delta(\mathbf{x}_1' - \mathbf{x}_N) \prod_{i=N-1}^{1} \hat{\Psi}^\dagger(\mathbf{x}_i)|0\rangle \pm \hat{\Psi}^\dagger(\mathbf{x}_N) \hat{\Psi}(\mathbf{x}_1') ... \hat{\Psi}^\dagger(\mathbf{x}_2) \hat{\Psi}^\dagger(\mathbf{x}_1)|0\rangle,$$

$$(2.56)$$

where the minus sign is valid for fermions while the plus sign for bosons, and the product, $\prod$, must be done stacking operator with decreasing index from left to the right, until hit the vacuum. Proceeding with similar steps until $\hat{\Psi}(\mathbf{x}_1')$ hits the vacuum yield

$$\hat{\Psi}(\mathbf{x}_1') \hat{\Psi}^\dagger(\mathbf{x}_N) ... \hat{\Psi}^\dagger(\mathbf{x}_2) \hat{\Psi}^\dagger(\mathbf{x}_1)|0\rangle = \sum_{j=1}^{N} (\pm 1)^{N-j} \delta(\mathbf{x}_1' - \mathbf{x}_j) \prod_{\substack{i=N \\ i \neq j}}^{1} \hat{\Psi}^\dagger(\mathbf{x}_i)|0\rangle. \qquad (2.57)$$

This last equation can be inserted in Eq. (2.55) to obtain

$$|\Phi^{(N-1)}\rangle = \sum_{j=1}^{N}(\pm 1)^{N-j} \int \left(\prod_{\substack{k=1 \\ k\neq j}}^{N} d\mathbf{x}_k\right) \frac{1}{\sqrt{N!}} \prod_{\substack{i=N \\ i\neq j}}^{1} \hat{\Psi}^\dagger(\mathbf{x}_i)|0\rangle \int d\mathbf{x}_j \delta(\mathbf{x}_1' - \mathbf{x}_j)\psi(\mathbf{x}_1, ..., \mathbf{x}_N),$$

(2.58)

where for each summation term is possible to separate the integral corresponding to the missing operator, thereby, integrating only the delta with the wave-function. After this integration is calculated, the j-th argument of ψ will be replaced by $\mathbf{x}_1'$, with all others unaffected,

$$|\Phi^{(N-1)}\rangle = \sum_{j=1}^{N}(\pm 1)^{N-j} \int \left(\prod_{\substack{k=1 \\ k\neq j}}^{N} d\mathbf{x}_k\right) \frac{1}{\sqrt{N!}} \prod_{\substack{i=N \\ i\neq j}}^{1} \hat{\Psi}^\dagger(\mathbf{x}_i)|0\rangle \psi(\mathbf{x}_1, ..., \mathbf{x}_{j-1}, \mathbf{x}_1', \mathbf{x}_{j+1}, ..., \mathbf{x}_N).$$

(2.59)

A final step is a rearrangement of the variables for each j. First, in the wave-function ψ, the variable $\mathbf{x}_1'$ can be moved one position at a time until occupying the first argument. As consequence of moving this way, $j-1$ successive exchanges with neighbor arguments are required, and yield a overall factor of $(\pm 1)^{j-1}$ due to these permutations, thereby

$$|\Phi^{(N-1)}\rangle = \sum_{j=1}^{N}(\pm 1)^{N-1} \int \left(\prod_{\substack{k=1 \\ k\neq j}}^{N} d\mathbf{x}_k\right) \frac{1}{\sqrt{N!}} \prod_{\substack{i=N \\ i\neq j}}^{1} \hat{\Psi}^\dagger(\mathbf{x}_i)|0\rangle \psi(\mathbf{x}_1', ..., \mathbf{x}_{j-1}, \mathbf{x}_{j+1}, ..., \mathbf{x}_N),$$

(2.60)

with the permutation factor $(\pm 1)^{j-1}$ merged into the previous $(\pm 1)^{N-j}$. Moreover, all the integration variables $\mathbf{x}_k$, with $k > j$, can be relabeled decreasing one index, with $k \to k-1$, resulting in the integration variable indexes always between 1 and $N-1$,

$$|\Phi^{(N-1)}\rangle = \sum_{j=1}^{N}(\pm 1)^{N-1} \int \left(\prod_{k=1}^{N-1} d\mathbf{x}_k\right) \frac{1}{\sqrt{N!}} \prod_{i=N-1}^{1} \hat{\Psi}^\dagger(\mathbf{x}_i)|0\rangle \psi(\mathbf{x}_1', \mathbf{x}_1, ..., \mathbf{x}_{N-1}), \quad (2.61)$$

which has no dependence on j, and finally

$$|\Phi^{(N-1)}\rangle = \sqrt{N}(\pm 1)^{N-1} \int \left(\prod_{k=1}^{N-1} d\mathbf{x}_k\right) \frac{1}{\sqrt{(N-1)!}} \prod_{i=N-1}^{1} \hat{\Psi}^\dagger(\mathbf{x}_i)|0\rangle \psi(\mathbf{x}_1', \mathbf{x}_1, ..., \mathbf{x}_{N-1}).$$

(2.62)

The factor $(\pm 1)^{N-1}$ in this last equation is particular to the choice of setting the first variable of the wave function, although, in general, the required assumption is to fix one

arbitrary argument of ψ to hold $\mathbf{x}_1'$. Nevertheless, with $\mathbf{x}_1'$ as the first argument the expression is apparently more convenient to interpret, as it is very similar to the initial one to a system of $N - 1$ particles, Eq. (2.53), apart of the numerical factors before the integration and the additional label $\mathbf{x}_1'$.

The original goal of computing Eq. (2.54) now follows straightforward calculations in applying $\hat{\Psi}(\mathbf{x}_2')\hat{\Psi}(\mathbf{x}_1')|\Psi^{(N)}\rangle = \hat{\Psi}(\mathbf{x}_2')|\Phi^{(N-1)}\rangle$, basically repeating the steps above,

$$|\Phi^{(N-2)}\rangle \equiv \hat{\Psi}(\mathbf{x}_2')|\Phi^{(N-1)}\rangle = \sqrt{N}(\pm 1)^{N-1}$$
$$\left[\int \left(\prod_{k=1}^{N-1} d\mathbf{x}_k \right) \frac{1}{\sqrt{(N-1)!}} \hat{\Psi}(\mathbf{x}_2')\hat{\Psi}^\dagger(\mathbf{x}_{N-1})...\hat{\Psi}^\dagger(\mathbf{x}_1)|\mathbf{0}\rangle f^{(1)}(\mathbf{x}_1, ..., \mathbf{x}_{N-1}) \right], \quad (2.63)$$

where $f^{(1)}(\mathbf{x}_1, ..., \mathbf{x}_{N-1}) \equiv \psi(\mathbf{x}_1', \mathbf{x}_1, ..., \mathbf{x}_N)$ ease the calculations since $\mathbf{x}_1'$ plays no important role. For the expression inside square brackets, following very similar passages done starting from Eq. (2.55) yield

$$|\Phi^{(N-2)}\rangle = \sqrt{N(N-1)}(\pm 1)^{N-2}(\pm 1)^{N-1}$$
$$\int \left(\prod_{k=1}^{N-2} d\mathbf{x}_k \right) \frac{1}{\sqrt{(N-2)!}} \prod_{i=N-2}^{1} \hat{\Psi}^\dagger(\mathbf{x}_i)|\mathbf{0}\rangle \psi(\mathbf{x}_1', \mathbf{x}_2', \mathbf{x}_1, ..., \mathbf{x}_{N-2}). \quad (2.64)$$

Therefore, for the general case,

$$\hat{\Psi}(\mathbf{x}_n')...\hat{\Psi}(\mathbf{x}_1')|\Psi^{(N)}\rangle = \sqrt{\frac{N!}{(N-n)!}}(\pm 1)^{(N-(n+1)/2)n}$$
$$\int \left(\prod_{k=1}^{N-n} d\mathbf{x}_k \right) \frac{1}{\sqrt{(N-n)!}} \prod_{i=N-n}^{1} \hat{\Psi}^\dagger(\mathbf{x}_i)|\mathbf{0}\rangle \psi(\mathbf{x}_1', ..., \mathbf{x}_n', \mathbf{x}_1, ..., \mathbf{x}_{N-n}). \quad (2.65)$$

Back to Eq. (2.54), using Eq. (2.65) with the proper labels A and B in the wave functions,

$$\langle \Psi_A^{(N)}; t|\Psi^\dagger(\mathbf{y}_1')...\Psi^\dagger(\mathbf{y}_n')W(\mathbf{y}_1', ..., \mathbf{y}_n'; \mathbf{x}_n', ..., \mathbf{x}_1')\Psi(\mathbf{x}_n')...\Psi(\mathbf{x}_1')|\Psi_B^{(N)}; t\rangle =$$
$$\frac{N!}{\left[(N-n)!\right]^2} \int \left(\prod_{k=1}^{N-n} d\mathbf{y}_k d\mathbf{x}_k \right) \left[\langle \mathbf{0}|\hat{\Psi}(\mathbf{y}_1)...\hat{\Psi}(\mathbf{y}_{N-n})\hat{\Psi}^\dagger(\mathbf{x}_{N-n})...\hat{\Psi}^\dagger(\mathbf{x}_1)|\mathbf{0}\rangle \right.$$
$$\left. \psi_A(\vec{\mathbf{y}}', \mathbf{y}_1, ..., \mathbf{y}_{N-n}; t)^* W(\vec{\mathbf{y}}'; \vec{\mathbf{x}}')\psi_B(\vec{\mathbf{x}}', \mathbf{x}_1, ..., \mathbf{x}_{N-n}; t) \right], \quad (2.66)$$

where the notation $\vec{\mathbf{z}}' \equiv (\mathbf{z}'_1, ..., \mathbf{z}'_n)$ was introduced for brevity.

The calculation of the operator average $\langle \mathbf{0} | \hat{\Psi}(\mathbf{y}_1)...\hat{\Psi}(\mathbf{y}_{N-n}) \hat{\Psi}^\dagger(\mathbf{x}_{N-n})...\hat{\Psi}^\dagger(\mathbf{x}_1) | \mathbf{0} \rangle$ is provided in Ref. [66, ch. 21, p. 548], by adapting the general result

$$\langle \mathbf{0} | \hat{\Psi}(\mathbf{y}_1)...\hat{\Psi}(\mathbf{y}_m) \hat{\Psi}^\dagger(\mathbf{x}_m)...\hat{\Psi}^\dagger(\mathbf{x}_1) | \mathbf{0} \rangle =$$

$$\sum_{\{P_i\}} (\pm 1)^{n(\{P_i\})} \delta(\mathbf{y}_{P_1} - \mathbf{x}_1) \delta(\mathbf{y}_{P_2} - \mathbf{x}_2)...\delta(\mathbf{y}_{P_m} - \mathbf{x}_m), \quad (2.67)$$

where $\{P_i\}$ is the set of all permutations of the tuple $(1, 2, ..., m)$, and $n(\{P_i\})$ is the number of permutations done. When substituting this result above, the integrals over $\mathbf{x}_k$ can be evaluated, meanwhile, for each term in the sum over permutations, the un-primed arguments in ψ_B will be shuffled. Notwithstanding, the wave-function ψ_B is also symmetric$(+1)$ or antisymmetric(-1) under permutations by construction in Eq. (2.52), therefore, this can be used to eliminate the $(\pm 1)^{n(\{P_i\})}$ factor to produce

$$\langle \Psi_A^{(N)}; t | \Psi^\dagger(\mathbf{y}'_1)...\Psi^\dagger(\mathbf{y}'_n) W(\mathbf{y}'_1, ..., \mathbf{y}'_n; \mathbf{x}'_n, ..., \mathbf{x}'_1) \Psi(\mathbf{x}'_n)...\Psi(\mathbf{x}'_1) | \Psi_B^{(N)}; t \rangle =$$

$$\frac{N!}{\left[(N-n)!\right]} \int \left(\prod_{k=1}^{N-n} \mathrm{d}\mathbf{y}_k \right) \psi_A(\vec{\mathbf{y}}', \mathbf{y}_1, ..., \mathbf{y}_{N-n}; t)^* W(\vec{\mathbf{y}}'; \vec{\mathbf{x}}') \psi_B(\vec{\mathbf{x}}', \mathbf{y}_1, ..., \mathbf{y}_{N-n}; t), \quad (2.68)$$

which complete the desired result for the moment.

In this assessment of a general n-body operator density some interesting features are now more evident. Apart from the primed variables, the others are simply integrated out in the wave-functions, which is usually addressed as a partial trace. The function W is rather general and can represent even non-local operators from ordinary quantum mechanics, which will be used in the following to show the compatibility with usual results starting from the second quantization formalism. Finally, ignoring the factorials, for $W = 1$ and $\vec{\mathbf{y}}' = \vec{\mathbf{x}}'$, the mutual probability of finding particles at $\mathbf{x}'_1, ..., \mathbf{x}'_n$ is obtained.

2.3   Many-body operators in second quantization

The many-body operators can be divided in classes considering the number of particles required to evaluate them. The most common ones are the single and two particle operators, which are related to free particles and their pairwise interactions respectively. However, in principle, general n-interacting particle operators are possible.

2.3.1 many-body extension of single particle operators

The extension of single particle operators to a many-body system can be done through its eigenstates. The indistinguishability of the particles requires only the occupation number in each eigenstate, hence, for a set of eigenvalues κ_i of an one-body operator K, the many-body extension is

$$\hat{K} = \sum_k \kappa_k \hat{a}_k^\dagger \hat{a}_k, \tag{2.69}$$

which, using the conversion rules in Eqs. (2.43, 2.44), can be expressed in a general IPS basis $\{|\phi_i\rangle\}$ as

$$\hat{K} = \sum_{kij} \kappa_k \langle \phi_i | \psi_k \rangle \hat{b}_i^\dagger \langle \psi_k | \phi_j \rangle \hat{b}_j. \tag{2.70}$$

The completeness relation for the single particle eigenstates $\{\psi_k\}$ yields

$$\hat{K} = \sum_{ij} \langle \phi_i | K | \phi_j \rangle \hat{b}_i^\dagger \hat{b}_j. \tag{2.71}$$

In addition to the general formula above, the same can be done in terms of the field operator. Generally, the projection on position of the single particle operator K involves terms containing analytic functions of $\mathbf{x}$ and derivatives. Specifically, $\langle \mathbf{x} | K | \phi \rangle = K(\mathbf{x}, \nabla)\langle \mathbf{x} | \phi \rangle$, thus, using the unitary operator as projection in position space implies

$$\hat{K} = \sum_{ij} \int d\mathbf{x} \langle \phi_i | \mathbf{x} \rangle \langle \mathbf{x} | K | \phi_j \rangle \hat{b}_i^\dagger \hat{b}_j = \int d\mathbf{x} \left(\sum_i \phi_i(\mathbf{x})^* \hat{b}_i^\dagger \right) K(\mathbf{x}, \nabla) \left(\sum_j \phi_j(\mathbf{x}) \hat{b}_j \right),$$

$$\hat{K} = \int d\mathbf{x} \hat{\Psi}^\dagger(\mathbf{x}) K(\mathbf{x}, \nabla) \hat{\Psi}(\mathbf{x}). \tag{2.72}$$

The precise proof for the equivalence of this operator $\hat{K}$ in second quantization formalism is obtained using overlap with two arbitrary many-body states. With Eq. (2.68), replacing $W(\mathbf{y}_1', \mathbf{x}_1') = K(\mathbf{y}_1', \nabla_{\mathbf{y}_1'})\delta(\mathbf{y}_1' - \mathbf{x}_1')$ and integrating in both $\mathbf{y}_1'$ and $\mathbf{x}_1'$ yield

$$\int d\mathbf{y}_1' d\mathbf{x}_1' \langle \Psi_A^{(N)}; t | \hat{\Psi}^\dagger(\mathbf{y}_1') K(\mathbf{y}_1', \nabla_{\mathbf{y}_1'})\delta(\mathbf{y}_1' - \mathbf{x}_1')\Psi(\mathbf{x}_1') | \Psi_B^{(N)}; t \rangle =$$

$$N \int \left(\prod_{k=1}^N d\mathbf{y}_k \right) \psi_A(\mathbf{y}_1, ..., \mathbf{y}_N; t)^* K(\mathbf{y}_1, \nabla_{\mathbf{y}_1})\psi_B(\mathbf{y}_1, ..., \mathbf{y}_N; t), \tag{2.73}$$

which is actually obtained after relabeling $\mathbf{y}_1'$ in the right side of equal sign. This is exact the same expression obtained when evaluating the overlap of two arbitrary wave-

functions with the operator K added up over all the particles positions, whereas due to the indistinguishability of the particles, K can act only in the first argument.

2.3.2   Many-body extension of interaction operators

An important point to note in the expression of single particle operators in Eq. (2.71) is the number of creation and annihilation operators. For a single annihilation operator to the right, any state that is not the vacuum can produce a nonzero expectation value. Intuitively, for a two-body interaction operator four field operators are needed in total, two of creation type and their adjoint.

From the position space representation of an interaction potential $V(\mathbf{x}_1, \mathbf{x}_2)$, its extension to second quantization formalism is

$$\hat{V} = \frac{1}{2} \int d\mathbf{x}_1 d\mathbf{x}_2 \hat{\Psi}^\dagger(\mathbf{x}_1) \hat{\Psi}^\dagger(\mathbf{x}_2) V(\mathbf{x}_1, \mathbf{x}_2) \hat{\Psi}(\mathbf{x}_2) \hat{\Psi}(\mathbf{x}_1). \tag{2.74}$$

In addition, V is usually required to have translational invariance, thus $V(\mathbf{x}_1, \mathbf{x}_2) \equiv V(|\mathbf{x}_1 - \mathbf{x}_2|)$. This expression can be verified with similar steps evaluated for single particle operators above, just setting $W(\mathbf{y}_1', \mathbf{y}_2'; \mathbf{x}_2', \mathbf{x}_1') = \frac{1}{2} V(\mathbf{y}_1', \mathbf{y}_2') \delta(\mathbf{x}_1' - \mathbf{y}_1') \delta(\mathbf{x}_2' - \mathbf{y}_2')$, integrating over all primed variables as well and adjusting some labels in integrations yield

$$\langle \Psi_A; t | \hat{V} | \Psi_B; t \rangle = \frac{N(N-1)}{2} \int \left(\prod_{k=1}^N d\mathbf{y}_k \right) \psi_A(\mathbf{y}_1, ..., \mathbf{y}_N; t)^* V(\mathbf{y}_1, \mathbf{y}_2) \psi_B(\mathbf{y}_1, ..., \mathbf{y}_N; t), \tag{2.75}$$

which matches the exact same expression of the expectation value of two-body operator with wave-functions, considering identical particles. Another form can be obtained using the conversion rule in Eq. (2.47),

$$\hat{\mathcal{V}} = \frac{1}{2} \sum_{k,l,q,s} \hat{a}_k^\dagger \hat{a}_s^\dagger \hat{a}_l \hat{a}_q \langle \phi_k, \phi_s | V | \phi_q, \phi_l \rangle, \tag{2.76}$$

which accepts any complete IPS basis $\{|\phi_k\rangle\}$ and is valid for both fermions and bosons within this strict ordering of indexes in operators and IPS.

Theoretically, general $n-$body interaction functions can be defined, although, there are no evidences that they are present in atomic systems. In ultracold regimes, as the precise potential function $V(\mathbf{x}_1, \mathbf{x}_2)$ is unknown, it is usually replaced by an effective contact interaction based on the scattering length of atom pairs. Such assumption, min-

imally demands that the interactions in the gas are well represented by pair collisions, whereas, no more than two particles are scattered at the same time, and wave-functions of outgoing particles from a collision event must assume their asymptotic form before another scattering process. This approximation requires a minimal diluteness of the gas, and when not fulfilled, $3-$body interaction terms are phenomenologically introduced to attenuate this problem. Nevertheless, it does not mean that there exists theoretically such an interaction, but instead, it tries to emulate 3-body simultaneous scattering. For a more elaborate discussion see Refs. [72, 73], especially the note listed as reference five in [72].

2.4   Reduced density matrices and correlations

A preliminar discussion about the $p-$order Reduced Density Matrix($p-$RDM) was made in the introduction, as a tool to provide information beyond meanfield approach. In the scope of this thesis it is defined as

$$\rho^{(p)}(\mathbf{x}_1,...,\mathbf{x}_p|\mathbf{x}_1',...,\mathbf{x}_p';t) = \left\langle \prod_{i=1}^{p} \hat{\Psi}^\dagger(\mathbf{x}_i') \prod_{j=1}^{p} \hat{\Psi}(\mathbf{x}_i) \right\rangle \frac{(N-p)!}{N!} \ , \qquad (2.77)$$

where the average is over an arbitrary time dependent state and the out-bracket terms provide unit trace due to the relation with the many-body wave-function, as derived in Eq. (2.68). This relation to the many-body wave-function is obtained simply setting $W = 1$ in Eq. (2.68), which yields

$$\rho^{(p)}(\mathbf{x}_1,...,\mathbf{x}_p|\mathbf{x}_1',...,\mathbf{x}_p';t) = \int \left(\prod_{i=p+1}^{N} \mathrm{d}\mathbf{x}_i \right) \psi^*(\mathbf{x}_1',...,\mathbf{x}_p',\mathbf{x}_{p+1},...,\mathbf{x}_N;t)\psi(\mathbf{x}_1,...,\mathbf{x}_N;t).$$

$$(2.78)$$

The unit trace follows immediately from the normalization of the wave-function,

$$\int \left(\prod_{i=1}^{p} \mathrm{d}\mathbf{x}_i \right) \rho^{(p)}(\vec{\mathbf{x}}|\vec{\mathbf{x}};t) = 1. \qquad (2.79)$$

where $\vec{\mathbf{x}}$ is short for $\mathbf{x}_1,...,\mathbf{x}_N$.

In addition to the probabilities distribution information, the $p-$RDM contains all necessary information to evaluate any $p-$body operators through traces, a property that specifically legitimize calling it by density matrix, which shall not be confused with a

statistical ensemble density matrix, since there is still a pure many-body state underneath its definition. For instance, from Eqs. (2.78, 2.73),

$$\langle \hat{K} \rangle = N \int \mathrm{d}\mathbf{x} \Big[K(\mathbf{x}, \nabla_{\mathbf{x}}) \rho^{(1)}(\mathbf{x}|\mathbf{x}'; t) \Big]_{\mathbf{x}'=\mathbf{x}}, \tag{2.80}$$

and similarly, using Eq. (2.75),

$$\langle \hat{V} \rangle = \frac{N(N-1)}{2} \int \mathrm{d}\mathbf{x}_1 \mathbf{x}_2 \Big[V(\mathbf{x}_1, \mathbf{x}_2) \rho^{(2)}(\mathbf{x}_1, \mathbf{x}_2 | \mathbf{x}_1', \mathbf{x}_2'; t) \Big]_{\substack{\mathbf{x}_1'=\mathbf{x}_1 \\ \mathbf{x}_2'=\mathbf{x}_2}}. \tag{2.81}$$

The $p-$RDM also provide a discrete form. Once introduced an IPS basis $\{|\phi_k\rangle\}_k$, with $\hat{a}_j$ being the corresponding operator to destroy a particle in the state $|\phi_j\rangle$, then

$$\rho^{(p)}_{i_1,\ldots,i_p,j_1,\ldots,j_p}(t) \equiv \langle \hat{a}_{i_1}^\dagger \ldots \hat{a}_{i_p}^\dagger \hat{a}_{j_1} \ldots \hat{a}_{j_p} \rangle \frac{(N-p)!}{N!}. \tag{2.82}$$

also with unit trace, which is the sum over all i_k, for $k = 1, ..., p$ and $j_k = i_k$. The proof is straightforward using the conversion rule Eq. (2.46) and Eq. (2.79). In addition, throughout the text, the tilde will denote the unnormalized $p-$RDM, with

$$\tilde{\rho}^{(p)} = \frac{N!}{(N-p)!} \rho^{(p)}. \tag{2.83}$$

In the following, some properties from the $1-$RDM are worked out, which are very important in the concepts of condensation, fragmentation and long-range order.

2.4.1   Natural occupations, condensation and fragmentation

The $1-$RDM is of special interest due to its relation to IPS bases. In order to show its importance concerning the Bose-Einstein condensation, it is relevant to define the first order coherence operator for an IPS basis representation, which is the second quantization version of the projection $|\psi_l\rangle\langle\psi_k|$ for two generic states labeled by l and k. Substituting $K \to |\psi_l\rangle\langle\psi_k|$ in Eq. (2.71), the first order coherence is given by

$$\hat{C}\big(|\psi_l\rangle\langle\psi_k|\big) = \sum_{ij} \langle\phi_i|\psi_l\rangle\langle\psi_k|\phi_j\rangle \hat{b}_i^\dagger \hat{b}_j = \hat{a}_l^\dagger \hat{a}_k, \tag{2.84}$$

where the conversion rules (2.43, 2.44) were used and $\hat{a}_k$ is the destruction operator in state

$|\psi_k\rangle$. With $\hat{C}_{lk} \equiv \hat{C}(|\psi_l\rangle\langle\psi_k|)$ for simplification, its average is one of the terms contained in an unnormalized discrete $1-$RDM, in particular, $\langle\hat{C}_{kk}\rangle = \langle\hat{a}_k^\dagger\hat{a}_k\rangle$ is the average occupation in single particle state $|\psi_k\rangle$. Calling this operator first order coherence is motivated by its average being the off-diagonal terms of $\tilde{\rho}^{(1)}$.

The natural single particle states, also known as natural orbitals, by definition are those whose the first order coherences vanishes, thus, related to diagonalization of the $1-$RDM. In terms of the normalized $1-$RDM $\rho^{(1)}$, its eigenvalues $\{p_k\}$ are positive due to hermiticity and constrained by the fixed total number of particles through Eq. (2.50),

$$1 = \text{Tr}\left(\rho^{(1)}(t)\right) = \sum_k p_k(t), \tag{2.85}$$

The determination of the natural occupations and orbitals requires the transformation matrix of the diagonal representation. First, introducing the unitary matrix U, which transforms the discrete $1-$RDM $\rho^{(1)}$ to a diagonal form as

$$\rho_{kl}^{(1)}(t) = \sum_i U_{ki}(t)p_i(t)U_{il}^\dagger(t), \tag{2.86}$$

then, the eigenvalues can be equivalently written as

$$p_j(t)\delta_{ij} = \sum_{kl} U_{ik}^\dagger(t)\rho_{kl}^{(1)}(t)U_{lj}(t). \tag{2.87}$$

With the definition in Eq. (2.82),

$$p_j(t)\delta_{ij} = \frac{1}{N}\sum_{kl} U_{ik}^\dagger(t)\langle\hat{a}_k^\dagger\hat{a}_l\rangle U_{lj}(t) = \frac{1}{N}\left\langle\left(\sum_k U_{ik}^\dagger(t)\hat{a}_k^\dagger\right)\left(\sum_l U_{lj}(t)\hat{a}_l\right)\right\rangle, \tag{2.88}$$

$$p_j(t)\delta_{ij} = \frac{1}{N}\langle\hat{c}_i^\dagger(t)\hat{c}_j(t)\rangle, \tag{2.89}$$

where the conversion rules (2.43, 2.44) were applied. This last equation proves that, for this set of operators $\{\hat{c}_i(t)\}$, indeed the first order coherence vanishes at every instant t, although their underlying IPS, which are the natural orbitals, remains to be specified.

The complete specification of the natural orbitals is determined by the spatial projection of the $1-$RDM [(2.77), $p = 1$]. With the field expansion in Eq. (2.47), it can be written as

$$\rho^{(1)}(\mathbf{x}|\mathbf{x}';t) = \sum_{k,l} \rho_{kl}^{(1)}(t)\phi_k^*(\mathbf{x}')\phi_l(\mathbf{x}). \tag{2.90}$$

Using Eq. (2.86), we can regroup the terms in a convenient way to obtain

$$\rho^{(1)}(\mathbf{x}|\mathbf{x}';t) = \sum_i p_i(t) \left[\sum_k U_{ki}(t)\phi_k(\mathbf{x}')^*\right]\left[\sum_l U_{li}^*(t)\phi_l(\mathbf{x})\right]. \tag{2.91}$$

Apart of the different summation index, the terms inside square brackets in this last equation are conjugate of each other. Therefore, the set $\{\psi_i(\mathbf{x},t)\}$, where,

$$\psi_i(\mathbf{x},t) = \sum_l U_{li}^*(t)\phi_l(\mathbf{x}), \tag{2.92}$$

provides the IPS which the operators $\{\hat{c}_i(t)\}$ refers to, as such, classifying them as the natural orbitals. The completeness of the initial set of IPS $\{\phi_k(\mathbf{x})\}$ implies the same condition for the natural orbitals, since they are related by an unitary transformation, and it is straightforward to verify the property

$$U_{ji}(t) = \int \mathrm{d}\mathbf{x}\psi_i(\mathbf{x},t)^*\phi_j(\mathbf{x}) = \langle\psi_i|\phi_j\rangle. \tag{2.93}$$

The natural orbitals also provide $\rho^{(1)}(\mathbf{x}|\mathbf{x}';t)$ in diagonal form, but in continuum means, as

$$\rho^{(1)}(\mathbf{x}|\mathbf{x}';t) = \sum_i p_i(t)\psi_i(\mathbf{x}',t)^*\psi_i(\mathbf{x},t) , \tag{2.94}$$

and therefore, also satisfies the eigenvalue equation

$$\int \mathrm{d}\mathbf{x}'\rho^{(1)}(\mathbf{x}|\mathbf{x}';t)\psi_k(\mathbf{x}';t) = p_k(t)\psi_k(\mathbf{x};t) . \tag{2.95}$$

Eventually, the proof of zero coherence can be done using the spatial projection of $1-$RDM, with Eq. (2.46) for the conversion of $\hat{c}$ to the field operators and using Eq. (2.95),

$$\frac{1}{N}\langle\hat{c}_k^\dagger(t)\hat{c}_l(t)\rangle = \int \mathrm{d}\mathbf{x}\int \mathrm{d}\mathbf{x}'\psi_k(\mathbf{x}';t)\psi_l(\mathbf{x};t)^*\frac{\langle\hat{\Psi}^\dagger(\mathbf{x}')\hat{\Psi}(\mathbf{x})\rangle}{N} = p_k(t)\delta_{kl} , \tag{2.96}$$

Within this general approach, we can define the average fraction of BEC particles according to the Penrose-Onsager criterion [55], by the largest value of the set $\{p_k(t)\}$. Conversely, if more eigenvalues have the same magnitude of the first one, taking into account the total number of particles, the many-particle state is said to be fragmented. As a final remark, the Refs. [60, 61, 69] provide relevant discussions about the subject of

this section though the normalization convention for $p-$RDM may change.

2.4.2   Correlations and fluctuations

Correlations in a generic statistical sample are related to simultaneous variations around the mean of two different variables weighted by their variances. This approach can be extended for any pair of observables, but a very relevant one is the spatial distribution probability of simultaneously find particles, since there is a stark contrast with the mean-field description.

The spatial $p-$order correlation function, $g^{(p)}$ follows the general definition

$$g^{(p)}(\mathbf{x}_1, ..., \mathbf{x}_p | \mathbf{x}'_1, ..., \mathbf{x}'_p; t) = \frac{\rho^{(p)}(\mathbf{x}_1, ..., \mathbf{x}_p | \mathbf{x}'_1, ..., \mathbf{x}'_p; t)}{\sqrt{\prod_{i=1}^{p} \rho^{(1)}(\mathbf{x}_i; t) \rho^{(1)}(\mathbf{x}'_i; t)}}, \tag{2.97}$$

which is the same as in the Ref. [61], with $\rho^{(1)}(\mathbf{x}; t) \equiv \rho^{(1)}(\mathbf{x} | \mathbf{x}; t)$. In the case the primed variables are equal to the unprimed ones, it reduces to

$$g^{(p)}(\mathbf{x}_1, ..., \mathbf{x}_p; t) = \frac{\rho^{(p)}(\mathbf{x}_1, ..., \mathbf{x}_p; t)}{\prod_{i=1}^{p} \rho^{(1)}(\mathbf{x}_i; t)}, \tag{2.98}$$

where the simplification on the explicit arguments $f^{(p)}(\mathbf{x}_1, ..., \mathbf{x}_p) \equiv f^{(p)}(\mathbf{x}_1, ..., \mathbf{x}_p | \mathbf{x}_1, ..., \mathbf{x}_p)$ was used for both $g^{(p)}$ and $\rho^{(p)}$. This formula shows that $g^{(p)}$ in this case is reduced to the mutual probability weighted by the independent probabilities.

A first important case to analyze is the pure condensate state, when an unique eigenvalue of $\rho^{(1)}$ is one or at least much larger than the others, such that for practical purposes $p_0 \approx 1$ and $p_k \approx 0$ for $k > 0$ in Eq. (2.94). Consequently, the many-body state describing the system must have only one occupied IPS, corresponding to $\hat{c}_0$, such that $\langle \hat{c}_0^\dagger \hat{c}_0 \rangle = N p_0$. Therefore, in the definition of the $p-$RDM, expanding the field operator in this basis of natural orbitals will be equivalent to substitute

$$\hat{\Psi}(\mathbf{x}) \rightarrow \hat{c}_0 \psi_0(\mathbf{x}), \tag{2.99}$$

whereas the correlation function becomes simply

$$g^{(p)}_{BEC}(\mathbf{x}_1, ..., \mathbf{x}_p) = 1. \tag{2.100}$$

This result is an extension of the long-range order mentioned in books for the case $g^{(1)}$ [21]. Moreover, it also shows that in a BEC, all particles work as independent variables in statistical distribution means, represented by the same wave-function $\psi_0(\mathbf{x})$, and this wave-function is usually regarded as the classical counterpart of the field operator, thereby, named as a meanfield approach. However, this shall not be confused with $\sqrt{N}\psi_0(\mathbf{x}) \equiv \langle \hat{\Psi}(\mathbf{x}) \rangle$, which would necessarily require fluctuations in the total number of particles. This issue is addressed in Refs. [74, 75], and there is no possibility that this approach fundamentally describes a pure many-particle state, regardless of whether it provides a good approximation.

2.5 MCTDHB equations of motion

In the previous sections in this chapter, the general framework of second quantization was reasonably explored, focusing in some features interesting for this project. Despite the generality of most passages, without distinguish between bosons and fermions, starting in this section and throughout the rest of the thesis, the particles will be treated exclusively as bosons with no further mention to fermions.

The main idea in the MCTDHB is the extension of the many-particle state implied in the meanfield approach, by allowing more IPS to include quantum depletion. From this starting point, all possible Fock states are considered for the many-particle state expansion, thereby, justifying the multiconfigurational name, with a configuration understood as a particular arrangement of occupation numbers respecting the total number of particles.

2.5.1 Individual particle states and configurational basis

Any many-body state can particularly be represented in the Fock basis, in terms of the states defined in Eq. (2.41), at any time instant t through basis expansion with a set of time-dependent coefficients, such that

$$|\Psi; t\rangle = \sum_{\vec{n} \in \Lambda(N)} C_{\vec{n}}(t)|\vec{n}\rangle, \tag{2.101}$$

with $\Lambda(N) = \{\vec{n} \in \mathbf{N}^\infty; \sum_i n_i = N\}$, considering an infinite IPS basis whose the occu-

pation numbers corresponds. The elements of the set in $\Lambda(N)$ are called configurations, which are arrangements of particles in the IPS.

Despite the completeness of the IPS set, according to the expansion in Eq. (2.101), they remain the same during any dynamical process, eventually consuming many configurations to accurately describe $|\Psi; t\rangle$. As example, in a dynamical process that squeeze or broaden an harmonic trap, the initial basis can become inappropriate if it was chosen for a fixed harmonic trapping parameter, while the physical process is simply a scale transformation, and consequently, require occupations in a larger number of states. A basis that adaptively squeeze or broaden its states according to the system's trap in this example would be more appropriate, and intuitively, less states are required in Eq. (2.101).

In addition to the intuitive example mentioned above, in a numerical approach the set $\Lambda(N)$ will be truncated as will be described in the next chapter, thus, the IPS basis should be the best possible at any time instant of the evolution. Therefore, a generic time dependence is introduced to provide a time adjustable basis and the corresponding operators are

$$\hat{a}_k(t) = \int \mathrm{d}\mathbf{x}\, \phi_k(\mathbf{x}, t)^* \hat{\Psi}(\mathbf{x}),\tag{2.102}$$

with $\{\phi_k(\mathbf{x}, t)\}$ satisfying orthonormality and completeness at every time instant t. The expansion then becomes

$$|\Psi; t\rangle = \sum_{\vec{n}} C_{\vec{n}}(t)|\vec{n}; t\rangle,\tag{2.103}$$

where

$$|\vec{n}; t\rangle \equiv \prod_k \frac{\left[\hat{a}_k^\dagger(t)\right]^{n_k}}{\sqrt{n_k!}}|\mathbf{0}\rangle.\tag{2.104}$$

The set of configurations used in the expansion (2.103) is no longer stated for simplicity. Numerically, this set of configurations will even be finite with a possible enumeration, but this will be approached later, and at this point, this omitted information will not harm the next passages.

In view of preserving the generality of the method for an arbitrary problem, the time dependence is established by minimization of Schrödinger action.

2.5.2 Action minimization

The equations of motion for the set of IPS and coefficients used in the expansion must be derived by minimization of

$$\mathcal{S}\Big[\mathbf{C}, \{\phi_k, \phi_k^*\}\Big] = \int \mathrm{dt}\Big[i\hbar\langle\Psi(t)|\dot{\Psi}(t)\rangle - \langle\Psi(t)|\hat{H}(t)|\Psi(t)\rangle - \sum_{k,l}\mu_{kl}(t)\langle\phi_k;t|\phi_l;t\rangle\Big], \quad (2.105)$$

where $\mu_{kl}(t)$ are Lagrange multipliers to ensure orthonormality of the IPS at all times, even if the set is truncated and not complete. The many-particle Hamiltonian is written in terms of the time dependent operators as

$$\hat{H}(t) = \sum_{l,k}\Big[\langle\phi_l;t|T|\phi_k;t\rangle\hat{a}_l^\dagger(t)\hat{a}_k(t) + \frac{1}{2}\sum_{s,q}\hat{a}_l^\dagger(t)\hat{a}_k^\dagger(t)\hat{a}_s(t)\hat{a}_q(t)\langle\phi_l,\phi_k;t|V|\phi_q,\phi_s;t\rangle\Big].$$
$$(2.106)$$

With the action properly set in Eq. (2.105), it needs to be minimized with respect to the coefficients and IPS independently. Using infinitesimal variations, this corresponds to vanishing functional derivatives,

$$\frac{\delta\mathcal{S}\Big[\mathbf{C}, \{\phi_k, \phi_k^*\}\Big]}{\delta\mathbf{C}} = 0, \quad \frac{\delta\mathcal{S}\Big[\mathbf{C}, \{\phi_k, \phi_k^*\}\Big]}{\delta\phi_j^*} = 0. \quad (2.107)$$

Therefore, the first requirement is to fully specify Eq. (2.105) in terms of all functions $\phi_k(\mathbf{x}, t)$ and complex coefficients $C_{\vec{n}}(t)$. Before proceeding with additional manipulations, it is worth to introduce the following useful formulas for the next steps [76],

$$\frac{d}{dt}\Big[\prod_i f_i(t)\Big] = \sum_i \frac{df_i}{dt}\prod_{j\neq i} f_j(t), \quad (2.108)$$

$$\frac{\delta}{\delta\phi_k^*(\mathbf{x}, t)}\langle\phi_j;t'|T|f;t'\rangle = \delta(t-t')\int\mathrm{d}\mathbf{x}'\delta_{kj}\delta(\mathbf{x}-\mathbf{x}')\Big[Tf(\mathbf{x}',t')\Big] = \delta_{kj}\delta(t-t')Tf(\mathbf{x},t),$$
$$(2.109)$$

$$\frac{\delta}{\delta\phi_k^*(\mathbf{x}, t)}\langle\phi_j,\phi_l;t'|V|g,f;t'\rangle = \delta(t-t')\int\mathrm{d}\mathbf{x}'\mathrm{d}\mathbf{x}''\Big\{$$

$$\Big[\delta_{kj}\delta(\mathbf{x}-\mathbf{x}')\phi_l(\mathbf{x}'',t)^* + \delta_{kl}\delta(\mathbf{x}-\mathbf{x}'')\phi_j(\mathbf{x}',t)^*\Big]V(\mathbf{x}',\mathbf{x}'')g(\mathbf{x}',t')f(\mathbf{x}'',t')\Big\}$$

$$= \delta(t-t')\Big[\delta_{kj}g(\mathbf{x},t)\langle\phi_l;t|W_V(\mathbf{x})|f;t\rangle + \delta_{kl}f(\mathbf{x},t)\langle\phi_j;t|W_V(\mathbf{x})|g;t\rangle\Big], \quad (2.110)$$

where the exchange symmetry of the potential, $V(\mathbf{x}_1, \mathbf{x}_2) = V(\mathbf{x}_2, \mathbf{x}_1)$, and the effective single particle operator

$$\langle \mathbf{x}_1 | W_V(\mathbf{x}) | \mathbf{x}_2 \rangle \equiv \delta(\mathbf{x}_2 - \mathbf{x}_1) V(\mathbf{x}, \mathbf{x}_2) \tag{2.111}$$

were used to simplify the last equation.

One tricky part is the computation of the time devirative of the state $|\Psi; t\rangle$, due to time dependence of the operators, therefore,

$$\frac{\partial}{\partial t} |\Psi; t\rangle = \sum_{\vec{n}} \frac{\partial C_{\vec{n}}}{\partial t} |\vec{n}; t\rangle + C_{\vec{n}}(t) \frac{\partial}{\partial t} |\vec{n}; t\rangle, \tag{2.112}$$

where

$$\frac{\partial}{\partial t} |\vec{n}; t\rangle = \frac{\partial}{\partial t} \prod_i \frac{\left(\hat{a}_i^\dagger(t)\right)^{n_i}}{\sqrt{n_i!}} |\mathbf{0}\rangle \tag{2.113}$$

$$= \sum_i \frac{1}{\sqrt{n_i!}} \left[\frac{\partial}{\partial t} \left(\hat{a}_i^\dagger(t)\right)^{n_i} \right] \prod_{j \neq i} \frac{\left(\hat{a}_j^\dagger(t)\right)^{n_j}}{\sqrt{n_j!}} |\mathbf{0}\rangle \tag{2.114}$$

$$= \sum_i (1 - \delta_{0n_i}) \sqrt{n_i} \left[\frac{\partial \hat{a}_i^\dagger(t)}{\partial t} \right] \frac{\left(\hat{a}_i^\dagger(t)\right)^{n_i-1}}{\sqrt{(n_i-1)!}} \prod_{j \neq i} \frac{\left(\hat{a}_j^\dagger(t)\right)^{n_j}}{\sqrt{n_j!}} |\mathbf{0}\rangle \tag{2.115}$$

$$= \sum_i (1 - \delta_{0n_i}) \sqrt{n_i} \left[\int d\mathbf{x} \frac{\partial \phi_i(\mathbf{x}, t)}{\partial t} \hat{\Psi}^\dagger(\mathbf{x}) \right] \frac{\left(\hat{a}_i^\dagger(t)\right)^{n_i-1}}{\sqrt{(n_i-1)!}} \prod_{j \neq i} \frac{\left(\hat{a}_j^\dagger(t)\right)^{n_j}}{\sqrt{n_j!}} |\mathbf{0}\rangle \tag{2.116}$$

$$= \sum_i (1 - \delta_{0n_i}) \sum_k \sqrt{n_i} \left\langle \phi_k; t \left| \frac{\partial}{\partial t} \right| \phi_i; t \right\rangle \hat{a}_k^\dagger(t) \frac{\left(\hat{a}_i^\dagger(t)\right)^{n_i-1}}{\sqrt{(n_i-1)!}} \prod_{j \neq i} \frac{\left(\hat{a}_j^\dagger(t)\right)^{n_j}}{\sqrt{n_j!}} |\mathbf{0}\rangle, \tag{2.117}$$

with Eq. (2.108) used from the first to second line and the field operator conversion rules used back and forth in the last two lines. The Kronecker delta only avoids deriving states with $n_i = 0$. Due to bosonic commutation rules in Eq. (2.39),

$$\hat{a}_i(t) \left(\hat{a}_j^\dagger(t)\right)^m = m \delta_{ij} \left(\hat{a}_j^\dagger(t)\right)^{m-1} + \left(\hat{a}_j^\dagger(t)\right)^m \hat{a}_i(t), \tag{2.118}$$

which implies

$$\frac{\partial}{\partial t} |\vec{n}; t\rangle = \sum_{ik} \left\langle \phi_k; t \left| \frac{\partial}{\partial t} \right| \phi_i; t \right\rangle \hat{a}_k^\dagger(t) \hat{a}_i(t) |\vec{n}; t\rangle. \tag{2.119}$$

As a final remark on these passages, the Kronecker delta factor is no longer needed since if $n_i = 0$, $\hat{a}_i(t)$ will act directly on vacuum state.

The equations for the coefficients are the easier ones to obtain compared to the IPS. It is important to note though, that only the state $|\Psi; t\rangle$ depends on the coefficients, thus, to compute the variations with respect to them, we can suitably express the action as

$$
S\Big[\mathbf{C}, \{\phi_k, \phi_k^*\}\Big] = \int \mathrm{dt} \Bigg\{ \sum_{\vec{n}'} C_{\vec{n}'}(t)^* \Big[i\hbar \frac{\partial C_{\vec{n}'}(t)}{\partial t} +
$$
$$
\sum_{\vec{n}} \left(i\hbar \left\langle \vec{n}'; t \left| \frac{\partial}{\partial t} \right| \vec{n}; t \right\rangle - \langle \vec{n}'; t | \hat{\mathcal{H}}(t) | \vec{n}; t \rangle \right) C_{\vec{n}}(t) - \sum_{k,l=1}^{M} \mu_{kl}(t) \langle \phi_k; t | \phi_l; t \rangle \Big] \Bigg\}, \quad (2.120)
$$

which after evaluating the functional derivatives with respect to the coefficients yields

$$
i\hbar \frac{\partial C_{\vec{n}'}(t)}{\partial t} = \sum_{\vec{n}} \left(\langle \vec{n}'; t | \hat{\mathcal{H}}(t) | \vec{n}; t \rangle - i\hbar \left\langle \vec{n}'; t \left| \frac{\partial}{\partial t} \right| \vec{n}; t \right\rangle \right) C_{\vec{n}}(t). \quad (2.121)
$$

The second term inside the parentheses seems unusual for a typical Hamiltonian time-evolution, but it came from the fact that the basis is time-dependent. Nonetheless, it can be removed with a proper unitary transformation, as will be done later.

The derivation of the IPS equations requires some extra passages. Firstly, gathering Eqs. (2.112, 2.119) to evaluate the first term in Eq. (2.105),

$$
\left\langle \Psi; t \left| \frac{\partial}{\partial t} \right| \Psi; t \right\rangle = \sum_{\vec{n}'} C_{\vec{n}'}(t)^* \frac{\partial C_{\vec{n}'}(t)}{\partial t} +
$$
$$
\sum_{ik} \left\langle \phi_k; t \left| \frac{\partial}{\partial t} \right| \phi_i; t \right\rangle \sum_{\vec{n}, \vec{n}'} \langle \vec{n}'; t | \hat{a}_k^\dagger(t) \hat{a}_i(t) | \vec{n}; t \rangle C_{\vec{n}'}(t)^* C_{\vec{n}}(t). \quad (2.122)
$$

The last term can be simplified with the definition of the discrete unnormalized $1-$RDM, hence,

$$
\left\langle \Psi; t \left| \frac{\partial}{\partial t} \right| \Psi; t \right\rangle = \sum_{\vec{n}'} C_{\vec{n}'}(t)^* \frac{\partial C_{\vec{n}}(t)}{\partial t} + \sum_{ik} \left\langle \phi_k; t \left| \frac{\partial}{\partial t} \right| \phi_i; t \right\rangle \tilde{\rho}_{ki}^{(1)}(t), \quad (2.123)
$$

where $\tilde{\rho}_{ki}^{(1)}(t) = \langle \Psi; t | \hat{a}_k^\dagger(t) \hat{a}_i(t) | \Psi; t \rangle$. Secondly, the expectation value of the Hamiltonian in terms of discrete $1-$ and $2-$RDMs is

$$
\langle \Psi; t | \hat{\mathcal{H}}(t) | \Psi; t \rangle = \sum_{l,k} \Bigg[\langle \phi_l; t | T | \phi_k; t \rangle \tilde{\rho}_{lk}^{(1)}(t) + \frac{1}{2} \sum_{s,q} \tilde{\rho}_{lksq}^{(2)}(t) \langle \phi_l, \phi_k; t | V | \phi_q, \phi_s; t \rangle \Bigg]. \quad (2.124)
$$

The next and final step is to compute the functional derivative over the parts in Eqs. (2.123, 2.124), thus

$$\frac{\delta}{\delta\phi_m^*(\mathbf{x},t')}i\hbar\left\langle \Psi;t\left|\frac{\partial}{\partial t}\right|\Psi;t\right\rangle = i\hbar\delta(t-t')\sum_i \tilde{\rho}_{mi}^{(1)}(t)\frac{\partial\phi_i(\mathbf{x},t)}{\partial t}, \qquad (2.125)$$

while for the Hamiltonian part

$$\frac{\delta}{\delta\phi_m^*(\mathbf{x},t')}\langle\Psi;t|\hat{\mathcal{H}}(t)|\Psi;t\rangle = \delta(t-t')\sum_k \left[\tilde{\rho}_{mk}^{(1)}(t)T\phi_k(\mathbf{x},t) +\right.$$

$$\left.\sum_{sq}\tilde{\rho}_{mksq}^{(2)}(t)\langle\phi_k;t|W_V(\mathbf{x})|\phi_s;t\rangle\phi_q(\mathbf{x},t)\right], \quad (2.126)$$

whose the interaction part is obtained using Eq. (2.110) and also the commutation rules of bosonic operators inside $\tilde{\rho}^{(2)}$ definition with some index relabeling. Substituting Eqs. (2.123, 2.124) in the action definition in Eq. (2.105), then, with the results provided by Eqs. (2.125, 2.126) give us

$$0 = \frac{\delta\mathcal{S}}{\delta\phi_m^*(\mathbf{x},t')} = i\hbar\sum_i \tilde{\rho}_{mi}^{(1)}(t')\frac{\partial\phi_i(\mathbf{x},t')}{\partial t'} - \sum_l \mu_{ml}(t')\phi_l(\mathbf{x},t')$$

$$-\sum_k\left[\tilde{\rho}_{mk}^{(1)}(t')T\phi_k(\mathbf{x},t') + \sum_{sq}\tilde{\rho}_{mksq}^{(2)}(t')\langle\phi_k;t'|W_V(\mathbf{x})|\phi_s;t'\rangle\phi_q(\mathbf{x},t')\right]. \quad (2.127)$$

The two Eqs. (2.121, 2.127) obtained still need some refinements to be more suitable for a numerical approach, which will be worked out in the following. First, this last equation for the IPS is the spatial projected version of

$$0 = i\hbar\sum_i \tilde{\rho}_{mi}^{(1)}(t)\frac{\partial}{\partial t}|\phi_i;t\rangle - \sum_l \mu_{ml}(t)|\phi_l;t\rangle - \sum_k\left[\tilde{\rho}_{mk}^{(1)}(t)T|\phi_k;t\rangle + \sum_{sq}\tilde{\rho}_{mksq}^{(2)}(t)W_{V_{ks}}(t)|\phi_q;t\rangle\right],$$

$$(2.128)$$

where the primes in time were dropped from the notation and the matrix operator $W_{V_{ks}}(t)$ have the property $\langle\mathbf{x}|W_{V_{ks}}(t)|f;t\rangle = \langle\phi_k;t|W_V(\mathbf{x})|\phi_s;t\rangle f(\mathbf{x},t)$. The Lagrange multipliers $\mu_{ml}(t)$ can be obtained by taking the product of the above equation with $\langle\phi_j;t|$, demanding the orthonormality condition at any time, $\langle\phi_j;t|\phi_n;t\rangle = \delta_{jn}$, therefore,

$$\mu_{mj}(t) = \langle\phi_j;t|\left\{i\hbar\sum_i \tilde{\rho}_{mi}^{(1)}(t)\frac{\partial}{\partial t}|\phi_i;t\rangle - \sum_k\left[\tilde{\rho}_{mk}^{(1)}(t)T|\phi_k;t\rangle + \sum_{sq}\tilde{\rho}_{mksq}^{(2)}(t)W_{V_{ks}}(t)|\phi_q;t\rangle\right]\right\},$$

$$(2.129)$$

and Eq. (2.128) for the IPS can be written in terms of a projector as

$$
0 = \left(\mathbb{1} - \sum_l |\phi_l; t\rangle\langle\phi_l; t|\right)\Bigg\{
$$
$$
i\hbar \sum_i \tilde{\rho}_{mi}^{(1)}(t)\frac{\partial}{\partial t}|\phi_i; t\rangle - \sum_k \left[\tilde{\rho}_{mk}^{(1)}(t)T|\phi_k; t\rangle + \sum_{sq} \tilde{\rho}_{mksq}^{(2)}(t)W_{V_{ks}}(t)|\phi_q; t\rangle\right]\Bigg\}. \quad (2.130)
$$

Another simplification can be done using the inverse of the matrix $\tilde{\rho}^{(1)}(t)$ to obtain

$$
0 = \left(\mathbb{1} - \sum_l |\phi_l; t\rangle\langle\phi_l; t|\right)\Bigg\{
$$
$$
i\hbar\frac{\partial}{\partial t}|\phi_j; t\rangle - T|\phi_j; t\rangle - \sum_{mksq} \left(\tilde{\rho}^{(1)}(t)\right)_{jm}^{-1}\tilde{\rho}_{mksq}^{(2)}(t)W_{V_{ks}}(t)|\phi_q; t\rangle\Bigg\}, \quad (2.131)
$$

which isolate the time derivative from the density matrix.

The final step working in these equations is the proof that we can always consider the projector acting on the time derivative as zero, that is equivalent to $\langle\phi_l; t|i\hbar(\partial/\partial t)|\phi_j; t\rangle = 0$, for all l and j. Aiming the proof, let $\{|\xi_i; t\rangle\}_i$ be another time moving basis related to the selected IPS by a unitary transformation $U(t)$, such that

$$
|\phi_j; t\rangle = \sum_i U_{ji}|\xi_i; t\rangle. \quad (2.132)
$$

Therefore, in order to have a zero projection of the time derivative,

$$
0 = \left\langle\phi_l; t\left|i\hbar\frac{\partial}{\partial t}\right|\phi_j; t\right\rangle \quad (2.133)
$$

$$
0 = \langle\phi_l; t|\sum_i \left(\frac{\partial U_{ji}}{\partial t}|\xi_i; t\rangle + U_{ji}\frac{\partial}{\partial t}|\xi_i; t\rangle\right) \quad (2.134)
$$

$$
0 = \sum_{ik} \left(\frac{\partial U_{ji}}{\partial t}U_{lk}^*\langle\xi_k; t|\xi_i; t\rangle + U_{ji}U_{lk}^*\left\langle\xi_k; t\left|\frac{\partial}{\partial t}\right|\xi_i; t\right\rangle\right), \quad (2.135)
$$

where we can use the unitarity of $U(t)$, multiplying by $U_{ln}(t)$ and summing in l to obtain

$$
0 = \sum_{ik} \left(\frac{\partial U_{ji}}{\partial t}\delta_{kn}\langle\xi_k; t|\xi_i; t\rangle + U_{ji}\delta_{kn}\left\langle\xi_k; t\left|\frac{\partial}{\partial t}\right|\xi_i; t\right\rangle\right), \quad (2.136)
$$

$$
\frac{\partial U_{jn}}{\partial t} = -\sum_i U_{ji}\left\langle\xi_n; t\left|\frac{\partial}{\partial t}\right|\xi_i; t\right\rangle. \quad (2.137)
$$

To complete the proof, it is straightforward to show that the matrix $D(t)$, which

$$D_{in}(t) = i \int_0^t dt' \left\langle \xi_n; t' \left| \frac{\partial}{\partial t} \right| \xi_i; t' \right\rangle, \tag{2.138}$$

is Hermitian using integration by parts and orthonormality $\langle \xi_n; t' | \xi_i; t' \rangle = \delta_{ni}$. Thus, using the Dyson series which commonly appears in time-dependent pertubation theory [66, Section 14.6, p. 338-340], we can express the solution for $U(t)$ as

$$U(t) = U(0)\mathcal{T} \exp\left[iD(t) \right], \tag{2.139}$$

with $\mathcal{T}$ the time-ordering operator. This last equation finishes the proof, since it shows that $U(t)$ is indeed unitary due to $D(t)$ hermiticity. Thereby, due to the equivalence of the spanned space, we can always impose this constraint in a variational approach for the action minimization. As a result, Eq. (2.119) will vanish, which implies a simpler form for the equations of motion (2.121, 2.131), such that, the final equations of MCTDHB can be written as

$$i\hbar \frac{\partial}{\partial t} |\phi_j; t\rangle = \left(\mathbb{1} - \sum_l |\phi_l; t\rangle\langle\phi_l; t| \right) \left\{ T|\phi_j; t\rangle + \sum_{mksq} \left(\tilde{\rho}^{(1)}(t) \right)^{-1}_{jm} \tilde{\rho}^{(2)}_{mksq}(t) W_{V_{ks}}(t)|\phi_q; t\rangle \right\}, \tag{2.140}$$

$$i\hbar \frac{\partial C_{\vec{n}'}(t)}{\partial t} = \sum_{\vec{n}} \langle\vec{n}'; t|\hat{\mathcal{H}}(t)|\vec{n}; t\rangle C_{\vec{n}}(t). \tag{2.141}$$

whereas the spatial projection of $W_{V_{ks}}(t)$ is given by (see its first definition in Eq. (2.111)),

$$\langle \mathbf{x}|W_{V_{ks}}(t)|\psi; t\rangle = \langle\phi_k; t|W_V(\mathbf{x})|\phi_s; t\rangle\psi(\mathbf{x}, t) = \int d\mathbf{x}' \phi_k^*(\mathbf{x}', t) V(\mathbf{x}, \mathbf{x}')\phi_s(\mathbf{x}', t)\psi(\mathbf{x}, t). \tag{2.142}$$

These final equations do not terminate all the underlying details, but at this stage, a few points are important to emphasize. The summation indexes were left unspecified during all the derivation, just to be as general as possible and not overcharge the notation. As such, a point to emphasize is the projector featuring in Eq. (2.140),

$$Q(t) = \mathbb{1} - \sum_l |\phi_l; t\rangle\langle\phi_l; t|, \tag{2.143}$$

which is zero if the IPS form a complete set, as such, implying all time derivatives to be

zero as well. This should be expected since for a complete set there is no need to include a time moving basis. However, this is not the case numerically, where a small number of functions can be used. Therefore, the number of IPS will be the main approximation parameter to tweak in the MCTDHB to improve accuracy of the results.

The meanfield approach can be easily obtained by constraining the number of IPS to 1, which also imply a single configuration and thus only one coefficient. Due to normalization, the time evolution of the coefficient is trivial, and the single IPS is then subject to

$$i\hbar\frac{\partial \phi_0(\mathbf{x},t)}{\partial t} = T(\mathbf{x},\nabla)\phi_0(\mathbf{x},t) + (N-1)\left[\int d\mathbf{x}'V(\mathbf{x},\mathbf{x}')\big|\phi_0(\mathbf{x}',t)\big|^2\right]\phi_0(\mathbf{x},t), \qquad (2.144)$$

where the density matrices are reduced to $\tilde{\rho}^{(1)}(t) = N$ and $\tilde{\rho}^{(2)}(t) = N(N-1)$ and the projector is no longer required since the final equation is already norm conservative. This is the well known GP equation, which governs the dynamics in a meanfield approach.

The equations of MCTDHB (2.140, 2.141) are rather complicated, even to solve numerically, because they involve systems of ordinary differential equations and partial integral-differential equations, all coupled to each other. Analytically, there is no hope to solve these equations, unless in the meanfield case with a single IPS. In the next chapter, the numerical integration techniques are described.

Chapter 3

Numerical implementation of MCTDHB

The numerical implementation is a challenging task, with two main relevant obstacles to overcome. The first is an effective way to enumerate the configurations after the truncation of the IPS basis. The second is a proper choice of algorithms to integrate the equations for coefficients and IPS altogether. The numerical approach for these problems and the pursue of a general algorithm implementation in which one can easily change all the parameters without need to access the source code is the most time consuming part for a project based on MCTDHB.

3.1 Finite multiconfigurational basis

With the truncation of the IPS basis, the set of all configurations will be finite and can be enumerated. Therefore, the space dimension can be addressed as the total number of possible arrangements of N identical particles in M different states, which can be evaluated by permuting the circles and sticks all together in Fig. (3.1), but removing self

Figure 3.1: Illustration of a generic configuration with particles as circles and IPS separated by vertical dashes.

permutations of both,

$$N_c(N, M) = \binom{N + M - 1}{M - 1} = \frac{(N + M - 1)!}{N!(M - 1)!}, \quad N, M \geq 1. \tag{3.1}$$

The many-particle Ansatz required in the Schrödinger action, Eq. (2.105), must be adapted with a notation for the finite number of configurations. With the IPS basis having M functions, the many-particle state becomes

$$|\Psi; t\rangle = \sum_{\beta=0}^{N_c(N,M)-1} C_\beta(t)|\vec{n}^{(\beta)}; t\rangle, \tag{3.2}$$

where $\vec{n}^{(\beta)} \in \Lambda(N, M)$, with

$$\Lambda(N, M) = \left\{ \vec{n} \in \mathbf{N}^M; \sum_{i=0}^{M-1} n_i = N \right\}, \tag{3.3}$$

β an enumeration index and $|\vec{n}^{(\beta)}; t\rangle$ encoding a time dependence due to the operators $\hat{a}_k^\dagger(t)$ used in their definition,

$$|\vec{n}^{(\beta)}; t\rangle \equiv \prod_{k=0}^{M-1} \frac{\left[\hat{a}_k^\dagger(t)\right]^{n_k^{(\beta)}}}{\sqrt{n_k^{(\beta)}!}} |\mathbf{0}\rangle. \tag{3.4}$$

Regarding the numerical implementation to handle this multiconfigurational space, there are two main issues which will be detailed in the next chapter. First, we need to enumerate the configurations, that is, to establish an unambiguous relation between β and its configuration $\vec{n}^{(\beta)}$. This problem is equivalent to develop a hashing function, and it was worked out in Refs. [77, 78]. Second, we need functions to act with the creation and annihilation operators, to handle the many-particle Hamiltonian.

3.2 Enumeration of configurations - Hashing Function

Sorting Fock states is a recurrent problem in numerical approach of many-particle systems, with some examples directed to particles confined in optical lattices within the Bose-Hubbard model [54, 79] and spin systems [80–82]. Nevertheless, the first general and
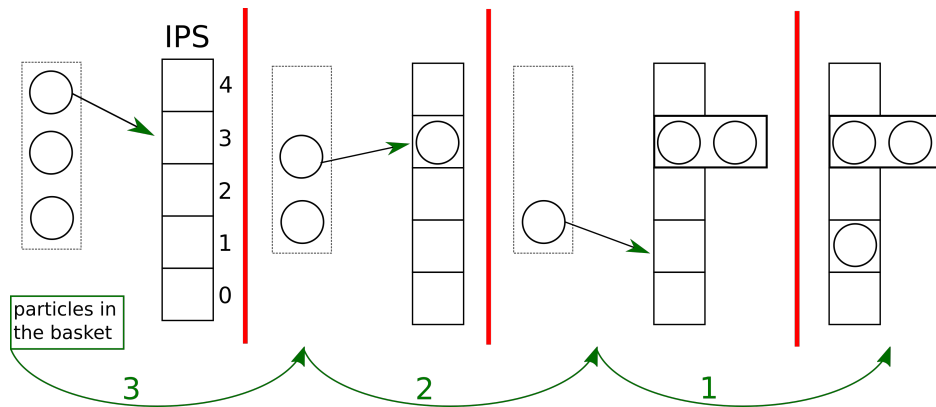
Figure 3.2: Example to illustrate the process of IPS occupations with $N = 3$ and $M = 5$ for the specific final state $|0, 1, 0, 2, 0\rangle$. The total cost of this configuration is $N_c(3, 3) + N_c(2, 3) + N_c(1, 1) = 17$ where the terms being added are presented following the order of arrows.

ideal hashing function was obtained in Ref. [77], only considering the particles type, which is characterized by an one-to-one mapping between configurations and integer numbers for a fixed arbitrary number of IPS. Later, an equivalent work [78] showed the same mapping with some additional details on handling operators. In the following, an alternative derivation of this hashing problem is presented for bosons attributing a metric to rank configurations.

Given an enumeration for the IPS from 0 to $M - 1$, if we take one with number k where $0 \leq k \leq M - 1$, there are other k IPS below it, since we are counting the number zero. Thus, to end up with a vector of integer numbers representing a configuration, we can think that we have to distribute particles from a basket to the IPS. In this way, to put a new particle in a selected state k, a cost is defined by the total number of configurations of remaining particles in the basket over all previous IPS, from 0 to $k - 1$. In other words, this cost is equivalent to the number of possibilities to set up the particles from the basket in k states, which is just the multiconfigurational space dimension with these k states.

The distribution process described above, executed from the highest to lowest indexed state, provides a raking for the configurations. When the basket has none particle left, the process is finished and the total cost will be the index of the configuration. In Fig. 3.2 a practical example is depicted, where the combination function defined in Eq. (3.1) plays a crucial role being used to compute the costs for every particle moved to the states.

The procedure described above, indexing of a generic object (all vectors in the set (3.3)), is called hashing [83]. The specific method suggested here yields an ideal hashing as will

be shown below, since it has no index collisions, because every index corresponds to an unique configuration, and the number of indexes required is the size of the configurational space.

3.2.1 Ideal hashing derivation

First, by definition, there is no cost to add particles in the state number 0, thus, for completeness, we can extend the definition in Eq. (3.1) such that

$$N_c(n, 0) \equiv 0, \tag{3.5}$$

for any $n \in \mathbb{N}$. Second, we can write a rigorous formula for the hashing function based on the discussion in the last section as

$$I(\vec{n}) = \sum_{m=1}^{M-1} \sum_{k=1}^{n_m} N_c \left(N - k + 1 - \sum_{i>m}^{M-1} n_i, m \right). \tag{3.6}$$

This general formula has some nested terms inside the arguments of N_c that deserve some attention. The part $\sum_{i>m} n_i$ account for the particles already distributed in higher ranked states, such that, $N - \sum_{i>m} n_i$ would be the remaining particles in the basket. However, this is actually correct for the first particle to be set in state m, if more particles occupies the same state, the remaining particles in the basket is updated by $-(k-1)$ part.

A second important point, besides the general formula in Eq. (3.6), is the proof that indeed no collisions can happen, that is, two different configurations cannot produce the same index, one of the properties of ideal hashing.

Taking advantage of the construction process, suppose two configurations $\vec{n}^{(1)}$ and $\vec{n}^{(2)}$ are different, thus, we can assume there is an index j which is the highest ranked state to provide different occupation numbers, as such, $n_i^{(1)} = n_i^{(2)}$ for all $i > j$. Consequently, $j \geq 1$ due to the common total number of particles constraint, which implies that $n_0^{(\alpha)} = N - \sum_{i=1}^{M-1} n_i^{(\alpha)}$, thus if $j = 0$ we would have $n_0^{(1)} = n_0^{(2)}$, contradicting the first assumption.

Without hamper the proof generality, we can take $n_j^{(1)} > n_j^{(2)}$, then

$$I(\vec{n}^{(1)}) - I(\vec{n}^{(2)}) = \sum_{m=1}^{j} \left[\sum_{k=1}^{n_m^{(1)}} N_c \left(N - k + 1 - \sum_{i>m}^{M-1} n_i^{(1)}, m \right) - \sum_{l=1}^{n_m^{(2)}} N_c \left(N - l + 1 - \sum_{i>m}^{M-1} n_i^{(2)}, m \right) \right]$$

$$\geq N_c \left(N - n_j^{(2)} - \sum_{i>j}^{M-1} n_i^{(2)}, j \right) - \sum_{m=1}^{j-1} \sum_{l=1}^{n_m^{(2)}} N_c \left(N - l + 1 - \sum_{i>m}^{M-1} n_i^{(2)}, m \right),$$

(3.7)

where the term inside square brackets for $m = j$ in the first line produces at least one positive outcome for $k = n_j^{(2)} + 1$, which is the one maintained outside the sum with all other possible positive contributions dropped. It is also worth to note the change of $n_i^{(1)} = n_i^{(2)}$ inside N_c first argument, since $i > j$. Moreover, still inside the first argument of N_c outside the sums, we must have $\sum_{i=j}^{M-1} n_i^{(2)} < N$, otherwise $n_j^{(1)}$ could not be greater than $n_j^{(2)}$, which contradicts the previous hypothesis.

For continuing the proof, the following properties

$$N_c(n, m - 1) = \left(\frac{m - 1}{n + m - 1} \right) N_c(n, m) < N_c(n, m), \tag{3.8}$$

$$N_c(n - 1, m) = \left(\frac{n}{n + m - 1} \right) N_c(n, m) \leq N_c(n, m), \tag{3.9}$$

are required to show that N_c monotonically increases with both arguments. Therefore, the maximum value of the nested sum in inequality (3.7) occurs when all remaining particles are set in state $j - 1$, thus

$$I(\vec{n}^{(1)}) - I(\vec{n}^{(2)}) \geq N_c(\tilde{n}, j) - \sum_{l=1}^{\tilde{n}} N_c(\tilde{n} - l + 1, j - 1), \tag{3.10}$$

where

$$\tilde{n} = N - \sum_{i=j}^{M-1} n_i^{(2)} > 1, \tag{3.11}$$

is the number of remaining particles in states with number $m < j$. If $j = 1$, we trivially obtain $I(\vec{n}^{(1)}) - I(\vec{n}^{(2)}) \geq N_c(\tilde{n}, 1) = 1$ and the proof ends. In the another case, $j > 1$, with the following formula [84, section 0.15]

$$\binom{n + m + 1}{n + 1} = \sum_{k=0}^{m} \binom{n + k}{n}, \tag{3.12}$$

we can adapt it for Eq. (3.1) so that

$$N_c(\tilde{n}, j) = \sum_{k=0}^{\tilde{n}} N_c(k, j-1).$$ (3.13)

Finally using the above equation back in inequality (3.10) yield

$$I(\vec{n}^{(1)}) - I(\vec{n}^{(2)}) \geq \sum_{k=0}^{\tilde{n}} N_c(k, j-1) - \sum_{l=1}^{\tilde{n}} N_c(\tilde{n} - l + 1, j-1) = N_c(0, j-1) = 1, \quad (3.14)$$

which not only proves that the hashing has no collisions but also spot further information about the ordering of the configurations.

As a final and easier step, the maximum index must be equal to the configurational space dimension. As N_c monotonically increases with both arguments, from Eq. (3.6), the largest index is given by

$$I_{MAX} = I(0, ..., N) = \sum_{k=1}^{N} N_c(N-k+1, M-1) = \sum_{k=1}^{N} N_c(k, M-1) = N_c(N, M) - 1, \quad (3.15)$$

where Eq. (3.13) was used to obtain the last equality, with the -1 due to enumeration starting at 0. This finally completes the proof that Eq. (3.6) provides an ideal hashing function.

As a final remark, in Refs. [77,78] an alternative approach using an equivalence to the problem involving fermions is used. In that case, differently of what was presented here, the basic structure is a vector with separators position, as depicted in Fig. (3.1).

3.2.2 Hashing algorithm

The previous section provide all the ingredients to implement two algorithms, the first to convert a given input configuration to its index and the second to set all occupations from a configuration index. The later case demands some additional effort as it is the inverse mapping, due to a look up for which state can be occupied according to its rank. Nevertheless, all the details unfold from the general hashing function, Eq. (3.6), and the increasing behavior of N_c with both arguments.

The pseudo-code to compute the index of a configuration is provided in algorithm (1), which essentially evaluate Eq. (3.6) backwards and for each state add the costs using Eq. (3.1) until none particles are left.

Algorithm 1 Get index of a configuration

Require: $N > 0$, $M > 0$, occupation vector $\vec{n}$

1: $k \leftarrow 0$
2: $s \leftarrow N$
3: **for** $m = M - 1..1$ **do**
4:     $j \leftarrow n[m]$
5:     **while** $j > 0$ **do**
6:         $k \leftarrow k + N_c(s, m)$
7:         $s \leftarrow s - 1$
8:         $j \leftarrow j - 1$
9:     **end while**
10: **end for**
11: **return** k

Algorithm 2 Build configuration $\vec{n}$ from index β

Require: $N > 0$, $M > 0$, $N_c(N, M) > \beta \geq 0$

1: **for** $i = 0..M - 1$ **do**
2:     $n[i] \leftarrow 0$
3: **end for**
4: $k \leftarrow \beta$
5: $m \leftarrow M - 1$
6: $s \leftarrow N$
7: **while** $k > 0$ **do**
8:     **while** $k - N_c(s, m) < 0$ **do**
9:         $m \leftarrow m - 1$
10:     **end while**
11:     $k \leftarrow k - N_c(s, m)$
12:     $n[m] \leftarrow n[m] + 1$
13:     $s \leftarrow s - 1$
14: **end while**
15: **if** $s > 0$ **then**
16:     $n[0] \leftarrow n[0] + s$
17: **end if**

The inverse hashing, assembling of a configuration from its index, is provided in algorithm (2). The outermost while loop iterate until the initial index is consumed by the costs to populate the states. In this iterative process, we must find the maximum state number m still satisfying $N_c(s, m) \leq k$, which means that at this iteration stage, k is larger than the space dimension with remaining particles s distributed in states with index from 0 to $m - 1$, as such, allowing to populate the state m. This process is repeated until $k = 0$, whereas, the rest of particles, if any, are set in the costless state, the one with number 0.

A worth point to be emphasized is the arbitrariness of the IPS enumeration, which is hold as an input features in a numerical approach. For instance, they generally nor are

energetically sorted neither the state number 0 hold the majority of particles. Moreover, the IPS used in the computation of time dynamics are not necessarily the natural ones defined in Sec. 2.4, though they are related by an unitary transformation.

Aiming the solution of the MCTDHB Eqs. (2.140, 2.141), some important numerical obstacles will be discussed in more details. The first one is the ineffectiveness of storing the Hamiltonian defined in Eq. (2.106), since it must be updated at every time step which impose a hard computational penalty. With the hashing algorithms provided in this section, we can actually work with a routine to apply the Hamiltonian using only the coefficients as input. Moreover, we can store mappings with the action rules of the creation and destruction operators, as explored in the following.

3.3   Relevant numerical improvements

Once the enumeration of configurations is properly defined, as well as the hashing algorithm, the next step is how to act with operators of second quantization formalism numerically. The goal is to take as input a vector of complex coefficients $\mathbf{C}$ from the finite expansion of a many-particle state as defined in Eq. (3.2), and compute expectation values involving $\hat{a}/\hat{a}^\dagger$, since by construction, all operators are reduced to this combination multiplied by complex numbers.

In view of the equations derived in the previous chapter, only up to $2-$body operators are needed. Therefore, we can focus in the properties of the $1-$ and $2-$RDMs as well as the Hamiltonian. The unnormalized discrete $1-$RDM in the truncated space is

$$\tilde{\rho}^{(1)}_{kl}(t) = \langle \Psi; t|\hat{a}^\dagger_k(t)\hat{a}_l(t)|\Psi; t\rangle = \sum_{\beta,\gamma=0}^{N_c(N,M)-1} C^*_\gamma(t)C_\beta(t)\langle \vec{n}^{(\gamma)}; t|\hat{a}^\dagger_k(t)\hat{a}_l(t)|\vec{n}^{(\beta)}; t\rangle, \quad (3.16)$$

while the $2-$RDM becomes

$$\tilde{\rho}^{(2)}_{klqs}(t) = \sum_{\beta,\gamma=0}^{N_c(N,M)-1} C^*_\gamma(t)C_\beta(t)\langle \vec{n}^{(\gamma)}; t|\hat{a}^\dagger_k(t)\hat{a}^\dagger_l(t)\hat{a}_q(t)\hat{a}_s(t)|\vec{n}^{(\beta)}; t\rangle. \quad (3.17)$$

In appendix A, the rules to compute the elements of $\tilde{\rho}^{(1)}$ and $\tilde{\rho}^{(2)}$ are summarized, which are readily obtained from the bosonic commutation relations. Finally, the Hamiltonian is essential for evolution of the coefficients in Eq. (2.141), thus, a numerical routine to

evaluate $\tilde{\mathbf{C}}$ such that

$$\tilde{\mathbf{C}}(t) = H(t) \cdot \mathbf{C}(t) , \quad \tilde{C}_\gamma = \sum_{\beta=0}^{N_c(N,M)-1} H_{\gamma\beta}(t)C_\beta(t) , \qquad (3.18)$$

is required, where H is the matrix representation of $\hat{H}$ in the configurational space with $H_{\gamma\beta}(t) = \langle \vec{n}^{(\gamma)}; t|\hat{H}(t)|\vec{n}^{(\beta)}; t\rangle$ with $\hat{H}$ defined in Eq. (2.106). It is worth to emphasize again that the matrix will not be stored since it must be updated according to the time evolution, instead, the hashing algorithms are used whenever needed for the action of operators.

In the computation of the operators described above, Eqs. (3.16, 3.17, 3.18), we need to perform just the sum in β, whereas for each β there is a unique value for γ, the one corresponding to the configuration after replacing the particles due to the action of the creation and annihilation operators. Therefore, for β running from 0 to $N_c(N,M)-1$, we need three steps to perform the operation required. First, obtain the configuration corresponding to β using algorithm 2. Second, reconfigure the occupation numbers according to the action of creation/annihilation operators. Finally, use this new configuration to compute the corresponding index γ using algorithm 1 and do the multiplication of coefficients, with the corresponding rules given in appendix A.

In a naive computation, we must use the algorithms 2 and 1 $N_c(N,M)$ times for every element of the density matrices, that results in a total of $M^2 N_c(N,M)$ calls of both functions to setup all the elements of $\tilde{\rho}^{(1)}$ and $M^4 N_c(N,M)$ for $\tilde{\rho}^{(2)}$[1]. The setup of $\tilde{\mathbf{C}}$ from the Hamiltonian action requires a similar number of operations of $\tilde{\rho}^{(2)}$ due to the sum over the IPS in $\hat{H}$ definition in Eq. (2.106).

This naive approach can be improved as shown in the following, whereas new structures to avoid such number of calls for the hashing algorithms are defined. Although these improvements are not related to physics, as will be shown, they are critical to make possible calculations with larger configurational spaces. Moreover, some balance between memory consumption and execution time must be achieved due to the inherent numerical complexity of the MCTDHB, otherwise relevant physical problems may be unfeasible due to ill use of resources.

---

[1]Actually, this number can be halved if one use hermiticity, and reduced even more using the commutation relations in the case of $\tilde{\rho}^{(2)}$. Moreover, when the indexes of the creation and annihilation operators are the same no calls of the conversion algorithms are need at all.
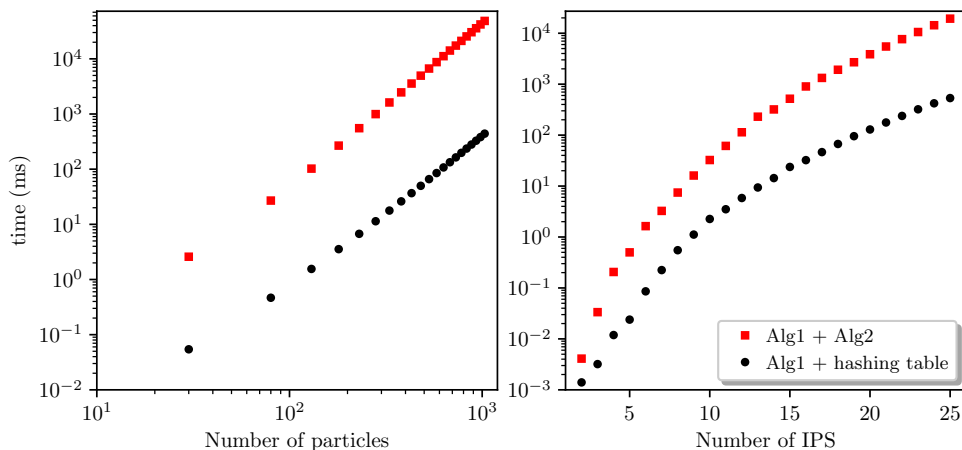
Figure 3.3: Time to compute all elements of $\tilde{\rho}^{(1)}$. The red squares correspond to an implementation that uses just the conversion algorithms 2 and 1 and the black circles make use of a hashing table to store and sort the configurations, which restrict to use only algorithm 1. In the left panel was fixed three IPS while varying the number of particles and in the right panel was varied the number of IPS with five particles.

3.3.1 Hashing table

A first improvement is to build once all occupation vectors and maintain them stored during all operations, defining a hashing table. For instance, they can be stored along rows of a matrix of integers, with the row number being the index of the respective configuration. This hashing table demands storage of $MN_c(N, M)$ integers in exchange of avoiding calls of algorithm 2 when computing $\tilde{\rho}^{(1)}$ and $\tilde{\rho}^{(2)}$.

The time required to set all $\tilde{\rho}^{(1)}$ elements is shown in Fig. 3.3 using two different implementations, the first using both algorithms 2 and 1, and the second using a hashing table (all configurations previously set in memory) and algorithm 1. The basic difference between the two implementations is the call of algorithm 2 face to a memory access of the hashing table. As can be noted in Fig. 3.3, the performance gain is critical, highlighted by the logarithmic scale, for both cases, when either varying the number of particles or the number of IPS. Moreover, in the left panel, the time required with respect to the number of particles has a clear linear relation in logarithmic scales, which indicates a power law of the form $\tau = bN^a$, with τ the time and N the number of particles, which will be investigated later.

The values of the time demanded in Fig. 3.3 are not specially relevant, since it depends on the hardware used and whether or not a parallel implementation is possible. The relevant part is the information on how the time demanded scales with the optimizations.

As we can see, the hashing table provided a time reduction of about 100 in the the most demanding cases with larger number of particles (left panel) or IPS (right panel).

Other routines, to build the two-body density matrices and to apply the Hamiltonian using the multiconfigurational basis shall benefit even more from the hashing table, because they require much more operations. Therefore, both $\tilde{\rho}^{(2)}$ and the Hamiltonian action routine will be the focus for the next improvements.

3.3.2   Second quantization operators mapping routines

The next step is to set the computational routines of Eqs. (3.16, 3.17, 3.18) completely free from calls of the algorithm 1 as well. For this aim, it is necessary to define a structure where given an index it has stored all possible jumps[2] of one and two particles among the IPS, corresponding to the action of one and two pairs of creation/annihilation operators respectively. This procedure is equivalent to store just column numbers of nonzero elements of a sparse matrix, where all forbidden transitions (annihilation operator in empty states) are ignored. Despite the underneath sparse matrix itself is time-dependent, the location of zeros is not.

In a single particle jump, one has at most M different states to remove a particle and M different states to place it back, which implies that for every configuration there are at most M^2 possible transitions. Thus a straightforward way to map all these transitions is to define a triple indexed structure, which stores integers, where the first index is from the configuration number, and the other two are IPS numbers, one from where the particle is being destroyed and other where it is being created. This one-particle jump mappings would require $N_c(N, M)M^2$ new integers to store.

It is worth pointing out that the memory cost for this one-particle jump mapping is greater than the first improvement of the hashing table, where in that case was stored all the occupation numbers and therefore had a cost of $N_c(N, M)M$ integers. This justify why there was no concern about memory cost at that stage. Moreover, the $N_c(N, M)M^2$ integers wastes some memory because there are configurations with some empty IPS, which actually do not have M^2 possible transitions. Therefore, in the implementation used in this project, the forbidden cases are ignored and this raw estimative is an upper bound. More details about how to do this is given in the following when double jumps

---

[2] Jump here means the simultaneous destruction and creation of particle in different states.
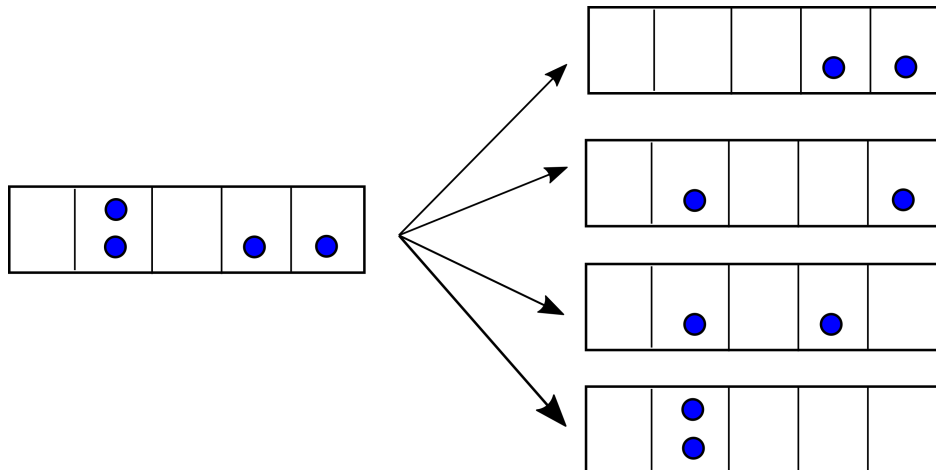
Figure 3.4: In the left, a possible configuration for $M = 5$ and $N = 4$. In the right the arrows indicate all possible ways to remove two particles from the single particle states, that is four.

mappings are introduced.

Analogously, a structure that maps double jumps can also be implemented, when two particles are moved to different IPS. If we follow the same naive idea presented for the one-particle jump, for each configuration there would be at most M^2 possibilities to take two particles from the occupation numbers, and for each one of these possibilities, there are again M^2 ways to replace them. Following this naive way, we would end up with the additional memory requirement of $N_c(N, M)M^4$ integers. Nevertheless, it is possible to attenuate this demand.

A thorough inspection over configurations shows us that M^2 possibilities to take two particles from the IPS (equivalent to the action of two annihilation operators) is not true for the most part of the configurations because there are many configurations with empty IPS. The real number of possibilities can be obtained as follows: for every non-empty IPS k, we search for $s \geq k$ non-empty as well, and whenever we find such numbers, we will have M^2 possible IPS to replace these particle taken from k and s.

In Fig. 3.4 is illustrated for a simple case, given a specific configuration, the possible ways to remove simultaneously two particles by the action of two annihilation operators. The arrows conducts to the possible outcomes, where for each one, we have M^2 possibilities to replace the particles removed. Originally, the naive way would store a lot of useless information since it considers a bunch of forbidden transitions, consisting on removal from empty states. For instance, in the case represented in Fig. 3.4, it would require $5^4 = 625$ possibilities, while there are only $4 \times 5^2 = 100$ real possibilities.

In summary, to save memory for this structure of double jump mappings, we cannot allocate those forbidden transitions. To overcome this problem, a structure like a hashing table must be defined, though each line of the table has a variable number of elements, where the line number corresponds to an index of a configuration. Its elements are integers, indexes of other configurations that are outcomes of all possible jumps of two particles.

A possible way to sort the elements for each line in the table is starting with the IPS $k = 0$ up to $k = M - 1$, we take $k \leq s < M$ and for each possible simultaneous removal of particles in k and s, we allocate a stride of M^2 integer numbers that corresponds to new configurations indexes obtained for every possible way to replace the particles removed. Therefore, if one wants to know the configuration index γ, that is a result of rearranging two particles of another configuration $\vec{n}^{(\beta)}$ from IPS i and $j \geq i$ to q and l IPS, it is required to check out how many strides must be ignored. In this case, the number of strides is the number of possible simultaneous removal from IPS k and s for every $k = 0, ..., i$ and $s = k, ..., j - 1$.

For example, suppose in Fig. 3.4 we are interested in the transitions that come from removing the last two particles, thus we need to skip 3 strides. In other words, in our table, in the line corresponding to the configuration in the figure, we need to skip the 3×5^2 elements to get the indexes of configurations we are interested. In the following we compare the performance between implementations that uses only hashing table and the ones that uses jump mappings.

In Fig. 3.5 the performances of two routines to setup $\tilde{\rho}^{(2)}$ are compared. The first, uses the hashing table of configurations and algorithm 1. The second, does not use any of the algorithms for conversion between indexes and configurations, instead, it uses the hashing table and jump mappings explained above. The hashing table is still required to exclude forbidden transition in the rules given in appendix A. For large number of particles, we see a good performance gain, while for large number of IPS, there is a slight improvement, indicating that the use of algorithm 1 is not the bottleneck in this case.

A careful inspection in algorithm 1 show us that it need to remove all particles from the configuration and thus demands the total number of particles as operations. Therefore, it is expected that the gain in performance using jump mappings is bigger for large number of particles than for large number of IPS. In other words, it is harder to empty many particles from a few IPS than a few particles from many IPS.
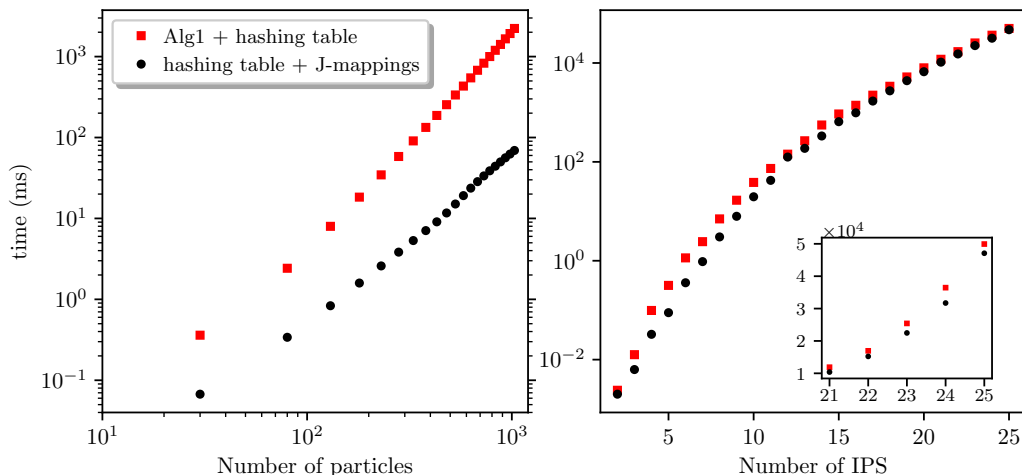
Figure 3.5: Time to compute all elements of $\tilde{\rho}^{(2)}$. The red squares correspond to an implementation that uses hashing table of configurations and calls of algorithm 1 while the black circles refers to one that uses direct jump mappings between configurations related by the action of the creation/annihilation operators and dismiss completely the use of algorithms 2 and 1. In the left while varying the number of particles, three IPS were used, and in the right, varying the number of IPS, five particles were used.

Another very important routine to check the performance gain is the time to act with the Hamiltonian over a state expressed in the configurational basis, that is to compute Eq. (3.18). In the same way that was done for $\tilde{\rho}^{(2)}$, in Fig. 3.6 we compare the time demanded in Eq. (3.18) using two routines, again one using the hashing table and algorithm 1 and other using the hashing table and jump mappings. Similarly, there is again a clear improvement varying the number of particles (left panel), but this time, there is also a substantial gain varying the number of IPS.

In all comparisons between the routines that used the algorithm 1 with the hashing table and those that use mappings, when varying the number of particles, there is an evident constant slope behavior in the logarithmic scale, at least for large number of particles. This reveals that the time demanded with respect to the number of particles can be written as a power law in the form

$$\tau_M(N) = b_M N^{a_M}, \tag{3.19}$$

where M is the number of IPS fixed. The parameters can be extracted from curve fitting, where a_M is the slope in the logarithmic scale plot. Since the study varying the number of particles in all cases presented here were carried out with $M = 3$, the index M is dropped
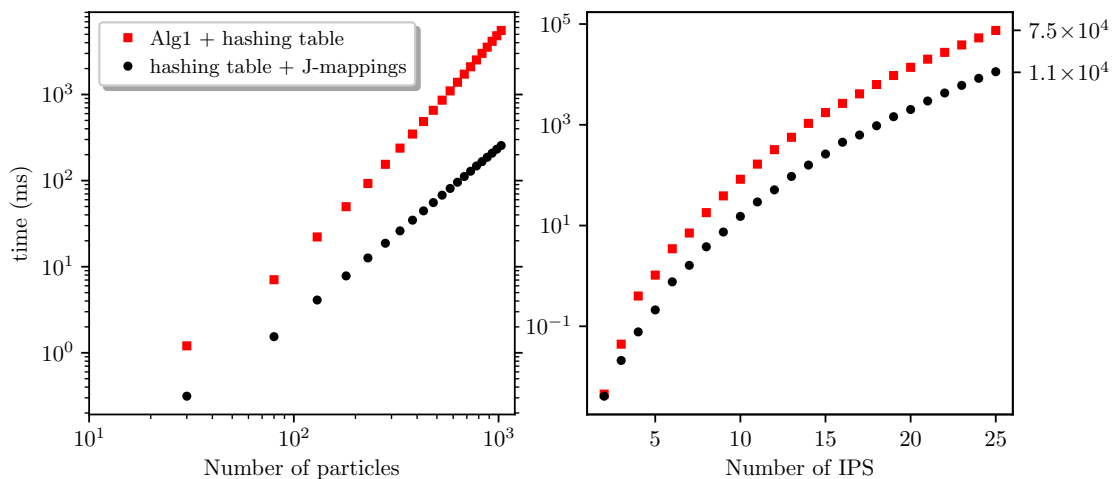
Figure 3.6: Time required to act with the Hamiltonian operator in the configuration basis as in Eq. (3.18). As done for $\rho^{(2)}$ in Fig. 3.5 the red squares correspond to a routine that uses hashing table and algorithm 1 and the black circles to one that uses mappings instead of algorithm 1. Three IPS and five particles were used in the left and right sub-figures respectively.

	$\rho^{(2)}$		$\mathcal{H}$	
	a	b	a	b
hashing table	2.835(5)	$6.33(9) \times 10^{-6}$	2.791(5)	$2.13(3) \times 10^{-5}$
jump mappings	2.34(3)	$6.4(6) \times 10^{-6}$	2.000(2)	$2.40(2) \times 10^{-4}$

Table 3.1: Fitted parameters, for implementations using hashing table and jump mappings, with $M = 3$ IPS using data with $N > 100$ particles, in the left panel of Figs. (3.5, 3.6).

from parameters in the following.

A linear curve fitting was evaluated for the most time demanding routines, $\tilde{\rho}^{(2)}$ and $H \cdot C$, with the values for the parameter shown in Tab. 3.1. The most important feature is that the mappings reduced the exponents(a) for both cases, what shows that the improvement is more expressive as larger is the number of particles.

In spite of all improvements the jump mappings brought, the limitations in terms of the additional memory demanded must be estimated. Indeed, all the gain in time had a cost in memory, as showed in Fig. 3.7. From the left panel, the case we vary the number of particles, we see that this cost is relatively cheap, some hundreds of megabytes (MB), right the case the performance gain was more expressive. The case in the right panel shows that we cannot ignore the memory consumption since it demanded up to some thousands of MB, thereby indicating that a possible limitation may come up if we go beyond $M = 25$ IPS with $N = 5$ particles.
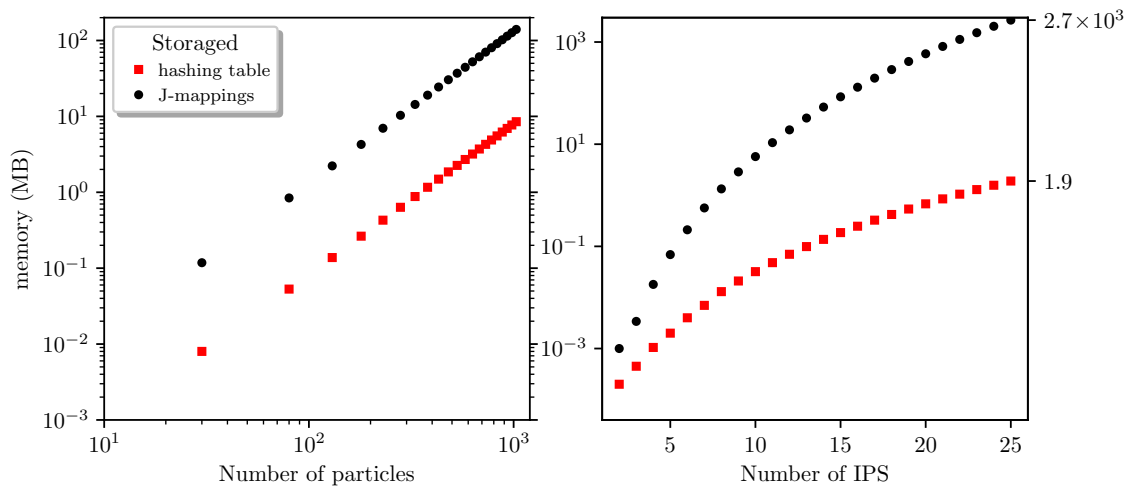
Figure 3.7: Memory allocation for the jump mappings structure of creation/annihilation operators and hashing table for the number of particles and IPS as used in previous figures, measured in megabytes (MB). Three IPS and five particles were used in the left and right sub-figures respectively.

	a	b
hashing table	1.9953(2)	$8.288(5) \times 10^{-6}$
jump mappings	2.0004(1)	$1.3158(1) \times 10^{-4}$

Table 3.2: Fitted parameters of power law for the memory consumption as function of N for $M = 3$ fixed, for the left panel of Fig. 3.7.

It is worth to highlight the very similar behavior between the memory cost in Fig. 3.7 and time execution in Fig. 3.6, where again a constant slope can be identified in the logarithmic scale plot with respect to the number of particles. The results of the fitting parameters according to Eq. (3.19) for memory consumption are shown in Tab. 3.2.

This survey on the numerical implementation details to handle the action of operators is important to establish application constraints. The profiled results showed here did not take into account the effects of parallelization, which are common in modern processors. A work to complement this study with a parallel implementation is provided in Ref. [65].

So far, all these subjects discussed were needed independent of what will be done with the IPS, which are the next subject. Before exploring them, an application is done with a physical system in the next section, using diagonalization techniques in the multiconfigurational space, with the IPS fixed as plane waves. This will demonstrate, without taking in account the variational method, a consistency test with respect to an exact solvable model.

3.4   Fixed IPS basis test - Lieb-Liniger gas

Before using the time-dependent approach with Eq. (2.140) for the IPS, with all the explanation of the previous sections, a test using Exact Diagonalization(ED) of the Hamiltonian in the multiconfigurational space [53, 54, 79, 80] is evaluated, considering the IPS fixed.

For the Hamiltonian diagonalization, the Lanczos iterative algorithm was used to compute approximately the ground state energy of a LL gas [4, 5], aiming an easy way to compare the numerical solution with an analytically solvable model. The LL Hamiltonian in Schrödinger formalism is given by [4–8]

$$\left[-\frac{\hbar^2}{2m} \sum_{i=1}^{N} \frac{\partial^2}{\partial x_i^2} + g \sum_{i,j>i}^{N} \delta(x_j - x_i) \right] \psi(x_1, ..., x_N) = E\psi(x_1, ..., x_N), \qquad (3.20)$$

where the wave function is subject to periodic boundary conditions $\psi(x_1, ..., x_k+L, ...x_N) = \psi(x_1, ..., x_k, ...x_N)$, $\forall k = 1, ..., N$ and g is the contact interaction strength.

The energies can be computed indirectly through the solution of a system of nonlinear equations. Here the same convention of Refs. [6,8] are adopted for these equations, which can be written as

$$\left\{ k_j = \frac{2\pi}{L} I_j - \frac{2}{L} \sum_{i=1}^{N} \arctan\left(\frac{k_j - k_i}{mg/\hbar^2} \right) \right\}_{j \in \left\{ -\frac{N-1}{2}, ..., \frac{N-1}{2} \right\}}, \qquad (3.21)$$

where for the ground state energy we must take $I_j = j - (N+1)/2$ and the energy is related to the numbers k_j by

$$E_0^{LL}(g) = \frac{\hbar^2}{2m} \sum_{j=1}^{N} k_j^2. \qquad (3.22)$$

Despite the relation in Eq. (3.22) looks like the kinetic energy of an ideal gas, it is worth to remind that these k_j depend on the contact interaction parameter g. However, in the limit $g \to \infty$, it is well known that the LL gas will be described by a Tonks-Girardeau(TG) gas [9], whose solution indicate that the energy will be given by the corresponding ideal Fermi gas, but with some care in choosing the momentum in the Slater determinant, because for an odd or even number of particles the fermions wave function must satisfy periodic or antiperiodic boundary conditions, respectively [10].

In Fig. 3.8, the ground state energy obtained from numerical diagonalization for 5 particles limited to 11 and 21 IPS are compared with the exact analytical solution computed
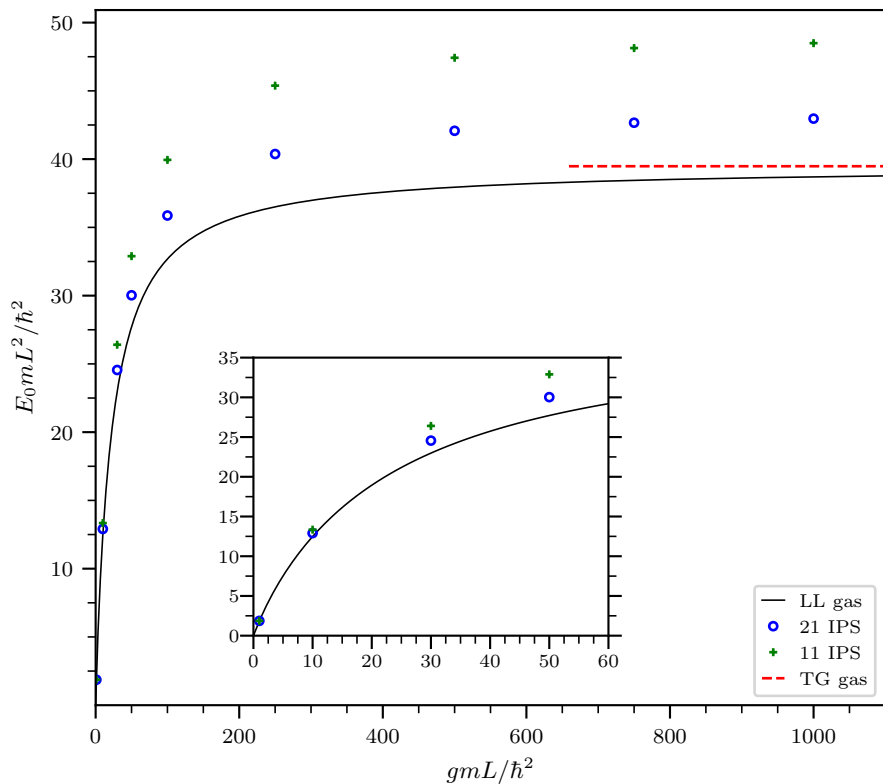
Figure 3.8: Ground state energy of the LL gas with five particles computed using numerical diagonalization (crosses and open circles) and the analytical form (full line).

from Eqs. (3.21, 3.22). The IPS in the numerical computation were chosen as periodic plane waves $\phi_n = e^{ik_n x}/\sqrt{L}$ where $k_n = 2\pi n/L$ with $n = -5, -4, ..., 4, 5$ (eleven IPS) and $n = -10, -9, ..., 9, 10$ (twenty one IPS). The numerical diagonalization was computed approximately using Lanczos algorithm for tridiagonal decomposition [85–87] together with LAPACK library [88] to diagonalize the resulting tridiagonal matrix.

The implementation of Lanczos iteration was done with complete re-orthogonalization, to enforce the orthogonality of the output eigenvectors [89,90] and the number of iteration was restricted to 1/8 of the dimension of configurational space given by Eq. (3.1), since Lanczos algorithm offer good precision with small number of iterations for the smallest eigenvalue as shown in Refs. [53, 87].

We can see that the deviation of the numerical solution from the exact analytical one in Fig. 3.8 grows with the interaction and diminishes as we increase the number of IPS. From the TG gas solution, the wave-function is not equal to the corresponding wave-function for the system of ideal fermions. Instead, it is necessary a symmetrization function, since the problem refers to bosons, as pointed out in Refs. [9, 10]. Therefore,

despite the fermions occupy exactly 5 IPS in the ground state, this is not true for the bosons, what can be at first sight counter intuitive.

There are two other important things to appoint about the convergence in this example. The first is about the observable being analyzed, the energy, which requires up to two-body features through the density matrix. The convergence for observables behaves differently depending upon the order of the RDM required, but generally, the convergence is slower as higher is the order. The second point is about the simplification of the configurational space due to translation invariance, which implies that the natural IPS are exactly the plane waves. Therefore, we could have separated sectors of the full Hilbert space with definite total angular momentum, allowing a larger number of IPS. Nonetheless, this example serves as an initial consistency test.

These results on the LL model, show us that the number of IPS plays the main role in the accuracy and assert the consistency of the multiconfigurational space part. Nevertheless, in this model is rather simple to choose the IPS, since it is periodic and no trap potential is present. It will not be the case for most of the current applications being studied and worked experimentally. Therefore, the following sections discuss the remaining numerical details of the MCTDHB with full time dependence, including the IPS.

3.5   Integration of MCTDHB equations

Most part of the technical points about the numerical implementation of the multiconfigurational space were discussed in the previous sections, but additional information is still necessary to provide accuracy metrics during time evolution and the specific protocol to handle the differential equations, which are approached in the following.

3.5.1   Coefficients and IPS integration protocol

Several works that applied MCTDHB numerically mention the same approach to evaluate Eqs. (2.140, 2.141) , among them, the default integration methods used were treated in more detail in Refs. [30, 91–93]. The consensus is that despite separately the IPS and coefficients may be highly oscillatory in time, the coupling between them promoted by $\tilde{\rho}^{(1)}(t)$, $\tilde{\rho}^{(2)}(t)$, $\langle\phi_l;t|T|\phi_k;t\rangle$ and $\langle\phi_l,\phi_k;t|V|\phi_q,\phi_s;t\rangle$ do not change as fast. Therefore,

the IPS and coefficients can be propagated independently for a period τ at which the coupling quantities are updated.

Since the evolution during this period τ can be done independently, different integrators may be designed separately for the IPS and coefficients. The system of Eqs. (2.141) is the easier one to solve because it is linear and consist of ordinary equations, thus, there is no many obstacles to choose an integrator. Here, two methods were applied, the Fourth-Order Runge-Kutta(RK4) [94] and Short Iterative Lanczos(SIL) [93, 95]. For the IPS, Eq. (2.140), one approach was to use Split-Step(SS) with Fast Fourier Transforms(SS-FFT) [96] or with Crank-Nicolson Finite Differences(SS-CNFD) [97–99], and the other using Discrete Variable Representation(DVR) [100–102] underneath a Fifth-Order RK(RK5).

A first thing to mention is about the time domain. In the form the action was proposed in Eq. (2.105), the resulting equations (2.140, 2.141) are prepared to study dynamics. However, we can exploit them turning the time purely imaginary, $t \equiv -iT$ with $T \in \mathbb{R}$. This trick allows us to collect the ground state of the system, provided that we constantly renormalize the IPS and coefficients during this propagation on imaginary time. Generally, the evolution in real time is more difficult and some specific cares are needed, thus a separate discussion will be done in the following.

The coefficients are usually integrated with SIL, since it is robust[3] and preserve the norm in exact arithmetic, what is seen as a major advantage for unitary time evolution. Besides, we may adaptively choose the order increasing the number of Lanczos iterations. The RK4 also performed well in many cases to integrate the coefficients, because the norm showed an oscillatory behavior in real time. Although, as drawback, RK4 may present instabilities depending on the problem and time step size. For imaginary time, used to obtain the ground state, the norm conservation is no longer an advantage and the preference is a matter of implementation complexity. The codes used in this project have both methods available.

The IPS must be carefully analyzed and treated differently for real and imaginary time. First, the Eq. (2.140) has to be adjusted for real time integration to correct the loss of orthogonality and a possible singularity of $\tilde{\rho}^{(1)}(t)$, which needs to be inverted. The solution for these issues are given in Ref. [91, 93] and will be detailed in the next section carefully. In summary, as the DVR method is able to tackle together the linear and

---

[3]A robust integrator means here a stable and accurate to a given order independently of the initial conditions.

nonlinear part simultaneously, it preserves better the orthonormality, while the split-step methods evolve separately the linear and nonlinear part, with the projection operator present only in nonlinear one. Therefore, for split-step case, while it evolves the linear part of the equations, they are not being projected, what certainly accelerate the loss of orthogonality.

Regarding this brief discussion, the coefficients' integrator generally chosen for real time is SIL while for imaginary time both, RK4 and SIL are used. For the IPS, the usual integrator for real time is DVR-RK5, while for imaginary time either SS-FFT or SS-CNFD can also be applied. Despite there are no more comments about the coefficients' equation, some details about the IPS need to be deeper approached, specially for real time.

3.5.2 Specific issues of real time evolution

Imaginary time evolution requires a renormalization process, as mentioned before, and specifically, the IPS must be re-orthogonalized as well due to norm loss. These steps must be done manually, since it is an intrinsic feature of imaginary time methods. Nevertheless, in real time, the exact arithmetic show us that the norm and orthogonality conservation are direct implications of Eqs. (2.140, 2.141), and it should be sustained up to some accuracy in the numerical approach.

As result of numerical finite precision, the overlap matrix

$$\mathcal{O}_{kl}(t) = \langle \phi_k; t | \phi_l; t \rangle, \tag{3.23}$$

is usually not equal to the unit matrix $\mathbb{1}_M$. As consequence, the projection operator in Eq. (2.143) must be generalized to the case where the set $\{|\phi_k; t\rangle\}_{k \in \{1,...,M\}}$ is not perfectly orthogonal. This problem is reported in Refs. [91,93], and the generalization of Eq. (2.143) is

$$\bar{Q}(t) = \mathbb{1} - \sum_{i,j=1}^{M} |\phi_i; t\rangle \mathcal{O}_{ij}^{-1}(t) \langle \phi_j; t|. \tag{3.24}$$

Another problem that arises is the possibility of $\tilde{\rho}^{(1)}(t)$ becoming singular either during the time evolution or due to the initial state being a perfect BEC, in which case $\tilde{\rho}^{(1)}(t)$ has just one nonzero eigenvalue equals to the total number of particles. That imposes the ambiguity on how an unoccupied state evolves, since it is not needed on the description. This problem can be bypassed in two steps.

In the case there are one or more unoccupied states initially, corresponding to zero eigenvalues of $\tilde{\rho}^{(1)}(t)$, the IPS are maintained fixed in time and just the Eq. (2.141) is propagated, until the states get occupied up to some threshold. The reason is that the time change in the IPS is only required because they are not a complete set, and if there are unoccupied states, the IPS are already good enough for the description. This emphasize that the variational approach to them is only taken into account from the beginning due to the ignorance of which is the best set of IPS to describe the problem.

A simple example that is similar to this problem is a coherent state expressed in terms of the number eigen-basis of the quantum harmonic oscillator. This expansion requires an infinite number of well defined number-states, despite the wave function is a displaced gaussian, which oscillates around the center of the trap when propagated in time. There is an exact moment when its overlap with the ground state is one, thus, all excited states are not needed at this instant. As the time elapses, the overlap with excited states increases through the coefficients in the expansion, and eventually, if there is only a finite number of basis states we will need to adapt them variationally.

There are occasions when $\tilde{\rho}^{(1)}(t)$ becomes singular at some time during the evolution. To circumvent this problem, a regularization is imposed, as suggested in Refs. [91, 93], where we must use

$$\tilde{\rho}^{(1)}_{\text{reg}} = \tilde{\rho}^{(1)} + \epsilon \exp\left(-\tilde{\rho}^{(1)}/\epsilon\right), \tag{3.25}$$

for numerical purposes with $\epsilon \in [10^{-8}, 10^{-12}]$ usually. This procedure implies a minimum occupation (lower bound for $\tilde{\rho}^{(1)}$ eigenvalues), which shall not be harmful for the many-particle state dynamics.

3.5.3 Control parameters and self-consistency

There are some remaining questions about the numerical methods described. In imaginary time case, the stopping criteria and consistency of the ground state obtained still need to be specified, while in real time, conservation of orthonormality and energy are important to monitor during time evolution. The energy is especially important in both contexts, computed by

$$E = \langle \hat{H} \rangle = \sum_{k,l=1}^{M} \left[\tilde{\rho}^{(1)}_{kl}(t) T_{kl}(t) + \sum_{n,m=1}^{M} \tilde{\rho}^{(2)}_{klnm}(t) V_{kl,nm}(t) \right], \tag{3.26}$$

where the abbreviations $T_{kl}(t) = \langle \phi_k; t|T|\phi_l; t\rangle$ and $V_{kl,nm} = \langle \phi_k, \phi_l; t|V|\phi_n, \phi_m; t\rangle$ were used starting from Eq. (2.106). For numerical purposes, it is important for dynamics since it must be conserved, and for ground state indicating when to stop the numerical iterations.

Specific for imaginary time propagation, the first parameter adopted is the numerical residue of the eigenvalue equation. With the Hamiltonian matrix in the configurational space H, where we recall that its elements are $H_{\gamma\beta} \equiv \langle \vec{n}^{(\gamma)}|\hat{H}|\vec{n}^{(\beta)}\rangle$, the residue is measured using

$$R_E = \|H \cdot \mathbf{C} - E\mathbf{C}\|_\infty / N, \tag{3.27}$$

with $\|\mathbf{v}\|_\infty \equiv \max |v_i|$ and E computed using Eq. (3.26). By using Eq. (3.26) we have a consistency test including the density matrices, moreover, this norm chosen is more sensible to all components of the coefficients vector. The tolerance is typically set to $R_E < 10^{-4}$.

The main parameter to define the stop criteria in imaginary time is the relative energy variation in one step. Given the a time step $\delta\tau$ we can define

$$\Delta_E(\tau) \equiv \left| \left[E(\tau + \delta\tau) - E(\tau)\right]/E(\tau)\right|. \tag{3.28}$$

The range of values used is $\Delta_E(\tau) \in [10^{-8}, 10^{-14}]$, with the minimum of 10^{-14} reserved for specific cases since it is near the numerical roundoff error.

For some specific trap potentials, which the Virial theorem could be developed, it was used as accuracy indicator of the ground state obtained. The virial theorem derivation here is based on a scale transformation in the IPS, where $\phi_k(x,t) \to \phi_k(\alpha x, t)$, and the corresponding energy $\tilde{E}(\alpha)$ computed with $\phi_k(\alpha x, t)$ must have a minimum in $\alpha = 1$, thus implying $\partial\tilde{E}/\partial\alpha|_{\alpha=1} = 0$. This yields an equation in the form

$$\beta_k K + \beta_{\text{tr}} V_{\text{tr}} + \beta_{\text{int}} V_{\text{int}} = 0, \tag{3.29}$$

where K, V_{tr} and V_{int} are the averages of kinetic, potential and interacting operators respectively, with the coefficients β depending on the Hamiltonian. Obviously the relation

is not zero at finite precision arithmetic, what lead us to define the following residue

$$R_{\mathrm{vir}} = \left| \frac{1}{\tilde{E}(\alpha)} \frac{\partial \tilde{E}}{\partial \alpha} \right|_{\alpha=1}.$$ (3.30)

For real time propagation, three criteria were established to be verified at each time step, and in case they are not fulfilled, the program exits with an error. The first is the energy conservation, and similarly to the definition for the imaginary time, the restriction $\Delta_E(t) < 10^{-2}$ is demanded from the definition in Eq. (3.28). The second is the conservation of coefficients vector L_2-norm, with the norm residual given by

$$R_{\mathbf{C}}(t) = \left| 1 - \|\mathbf{C}\|_2 \right|,$$ (3.31)

where the tolerance is $R_{\mathbf{C}}(t) < 10^{-6}$. The third is the conservation of IPS $\mathcal{L}_2$-norm and mutual orthogonality. Actually, this is implemented on average using the trace and off-diagonal elements of overlap matrix as

$$R_{\mathrm{ortho}}(t) = \left| 1 - \mathrm{Tr}\big(\mathcal{O}(t)\big)/M \right| + \sum_{k \neq l} \left| \mathcal{O}_{kl} \right|/M,$$ (3.32)

with the maximum accepted value set to $R_{\mathrm{ortho}}(t) < 10^{-4}$.

In Tab. 3.3, an output example is showed for a system of $N = 50$ particles harmonically trapped, using MCTDHB with $M = 4$ IPS subject to contact interaction in one dimension. The energy is measured in units of $\hbar\omega$, where ω is the trap frequency, and distance in units of harmonic oscillator length $l_0 = \sqrt{\hbar/(M\omega)}$. These quantities are printed as the program runs, showing an overview of convergence.

The R_E is initially zero because the initial coefficients are obtained from a fixed IPS diagonalization, equivalent from a ED method, with the IPS defined by the first four quantum harmonic oscillator eigenstates. Nevertheless, as the IPS are evolved in imaginary time, a better basis is obtained and the final result, besides being an eigenstate within the numerical tolerance, it also has a smaller energy. This summarize the advantage of MCTDHB over ED, with the basis capable to adapt for the problem.

Progress	E/N	R_{vir}	R_E	n_0
0%	5.8318116	0.509324	0.00000	63%
10%	5.2804467	0.092422	0.00181	66%
20%	5.2142280	0.033389	0.00754	84%
30%	5.1856275	0.003957	0.00141	94%
40%	5.1832663	0.001204	0.00024	95%
60%	5.1828232	0.000415	0.00004	96%
70%	5.1828088	0.000192	0.00002	96%
80%	5.1828060	0.000089	0.00001	96%
90%	5.1828054	0.000043	0.00000	96%
100%	5.1828053	0.000022	0.00000	96%

Table 3.3: Imaginary time propagation output for 50 particles in 1D harmonic trap. All quantities are in dimensionless units with trap frequency $\omega = g_{1D} = 1$. $M = 4$ IPS were used, which were integrated with SS-CN scheme. The final converged values, particularly the energy and n_0 are suitable for reproduction.

3.6   Final remarks about the codes developed

The codes were basically split in two parts, one to compute integration of Eqs. (2.140, 2.141) and another for post convergence analysis for computation of all relevant observables, where the first was developed in C language and the later in python. The codes were generally designed to solve the many-particle problem for any number of particles and IPS in one dimension, which are treated just as a regular user defined parameter, therefore, providing a very general package to study a reasonable range of physical systems.

Despite the equations were described in a generic way without specifying the number of spatial dimensions, the results presented in this thesis are restricted to one dimension and contact interaction. Thus, the supplementary definition of the interacting part in Eq. (2.142) is reduced to

$$\langle x|W_{V_{ks}}(t)|\psi;t\rangle = \int \mathrm{d}x' \phi_k^*(x',t) g_{1D}\delta(x-x')\phi_s(x',t)\psi(x,t) = g_{1D}\phi_k^*(x,t)\phi_s(x,t)\psi(x,t) \ ,$$
(3.33)

where g_{1D} is the effective contact interaction strength in one dimension, which experimentally is related to the trap squeezed dimension and scattering length of the atoms [103]. Moreover it is also assumed that we can sweep this parameter g_{1D}, either using the transversal trap producing the one dimensional geometry or with Feshbach resonances [104–106].

Chapter 4

Application of MCTDHB

The previous chapter summarized the most challenging part, the full derivation and numerical implementation of MCTDHB equations, which consumed appreciable efforts. After several tests, some of them comparing to the available codes in Ref. [107] and reproducing some results of Ref. [33], relevant studies were evaluated in a ring geometry. Part of the findings presented in section 4.2 below were published in Ref. [64], but besides, new unpublished results regarding dynamics are shown starting in section 4.3.

Bose gases trapped in an annular geometry are remarkable to study beyond meanfield features, since we can afford much more IPS than a typical two or three dimensional systems, as such, allowing to study strong interacting regimes and dynamical process with high fragmentation. This specific theme is also justified by the recent interest in quantum analogs and possible applications [108–112]. In the following, after a brief show of interesting yet simple results about deviation of the meanfield description, some features studied in the ring are superfluidity, persistent currents and its dynamics in the presence of a potential barrier.

4.1 Preliminary meanfield and MCTDHB differences

The MCTDHB proposes to tackle the quantum many-particle problem with more degrees of freedom than the meanfield approximation, where in the latter, there is a single state $|\phi_0; t\rangle$ governed by the GP equation (2.144). Therefore, the GP equation is a particular case when the expansion in Eq. (3.2) has only one term, $C_\beta(t) = \delta_{0\beta}$, with $|\vec{n}^{(0)}; t\rangle = |N, 0, \ldots 0; t\rangle$, whereas the density matrices are consequently reduced to $\tilde{\rho}_{kl}^{(1)}(t) = \delta_{k0}\delta_{l0}N$
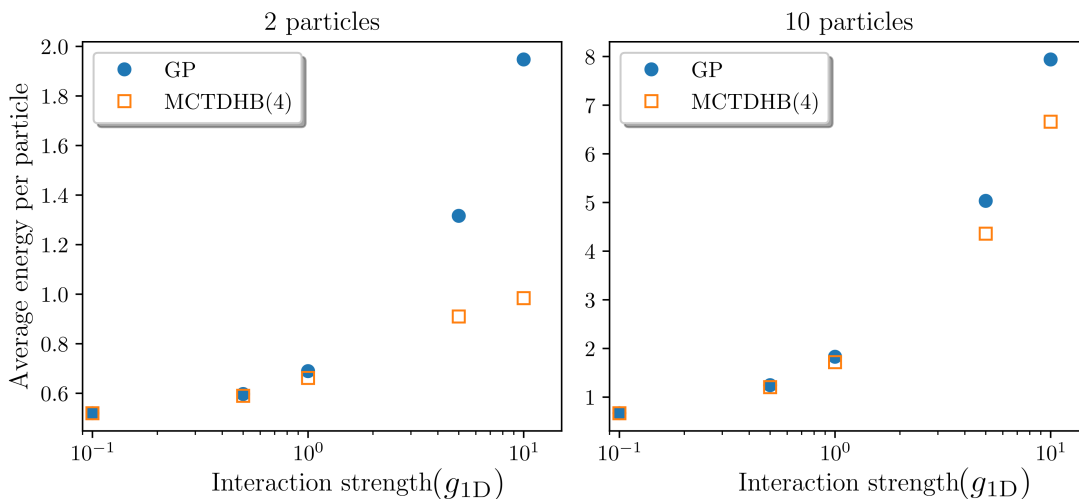
Figure 4.1: Comparison between energies from MCTDHB with 4 IPS, MCTDHB(4), and from meanfield for a system harmonically trapped as function of interaction strength parameter g_{1D}. Both axes are shown in dimensionless units which are normalized by harmonic trap parameter.

and $\tilde{\rho}^{(2)}_{klqs}(t) = \delta_{k0}\delta_{l0}\delta_{q0}\delta_{s0}N(N-1)$.

Since the GP equation is a restriction of the MCTDHB which comes from a variational approach, the GP energy must be an upper bound. This condition is verified in Fig. 4.1, which shows the energy obtained from both methods as function of the interaction strength, g_{1D}, for 2 and 10 particles in an harmonic trap described by the dimensionless Hamiltonian

$$\hat{H}_{HO} \equiv \int dx\ \hat{\Psi}^\dagger(x) \left(\frac{\partial^2}{\partial x^2} + \frac{x^2}{2} + \frac{g_{1D}}{2}\hat{\Psi}^\dagger(x)\hat{\Psi}(x) \right) \hat{\Psi}(x). \tag{4.1}$$

As could be anticipated, the agreement of both methods is better for weak interaction values, whereas the meanfield prediction for the energy grows above the MCTDHB values, as it should be according to the arguments above. Moreover, the relative deviation is smaller for 10 particles, with roughly 19% for $g_{1D} = 10$, while for this same value of g_{1D}, the meanfield prediction is approximately 98% above the MCTDHB for 2 particles.

Fig. 4.1 provides only a glimpse of the differences from the meanfield based on the variational theorem, which states that more degrees of freedom reduces the energy. Nonetheless, it also reveals a better description by the meanfield approach raising the number of particles. Apart from the particular case, this is an usual phenomenon and shows that the MCTDHB is more important for few particles systems.

Another consistency test is presented in Ref. [33], where an investigation of the Gross-Pitaevskii limit as proposed by Lieb [56, 57] is studied in one dimension. Despite there
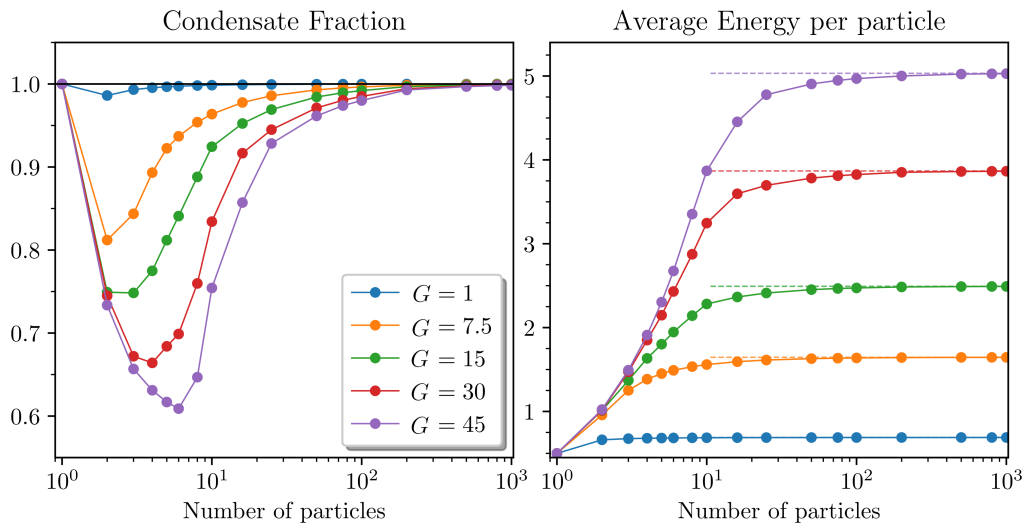
Figure 4.2: Convergence to mean field energy and condensate fraction (largest eigenvalue of $\rho^{(1)}$) for various values of $G = g_{1D}(N-1)$. The meanfield values to the energy are depicted by dashed lines with the corresponding color for each G. The full lines connecting the points only serve as guides.

is no convergence in the overlap of the many-particle state with a macroscopic occupied state, the energy converges to the meanfield approximation.

The GP limit is defined with $N \to \infty$ and $g_{1D} \to 0$ constrained to $g_{1D}(N-1) \equiv G$ being fixed in the process. The convergence of energy and condensate fraction, that is the largest eigenvalue of $\rho^{(1)}$, can be observed in Fig. 4.2, where again an harmonically trapped system is considered. Since G is fixed, g_{1D} varies according to N, but N was choose to the figure horizontal axis. The calculation changing the value of N was done adapting the number of IPS as the GP limit became closer, where for the extreme case with 1000 particles, $M = 3$ IPS were used, and for the most fragmented case, $N = 6$ and $G = 45$, $M = 15$ IPS were required.

Despite Fig. 4.2 provides a general outlook of the approximation to the meanfield description, it would be interesting to know how fast the convergence occurs, an information that may also help in the choice of the number of IPS in MCTDHB. The convergence behavior is better illustrated in Fig. 4.3, with the difference of MCTDHB and meanfield results plotted in log scale, for $G = 7.5$ and $G = 45$. A linear relation can be clearly identified for a large number of particles, a sector where a linear fitting was calculated with the resulting parameters provided in the figure legends. Interesting, the slope coefficient is almost independent of the meanfield parameter G, which appears to have a deeper impact in the bias coefficient. Similar results are shown in Ref. [33].
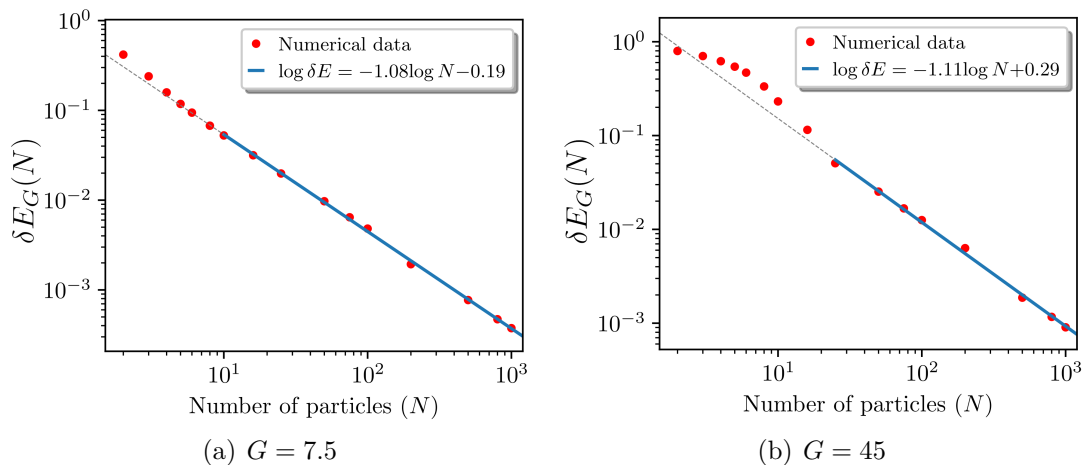
Figure 4.3: Fitting for the relative difference from both methods where $\delta E_G(N) = 1 - E_G^{(MC)}(N)/E_G^{(GP)}$, based on values shown in Fig. 4.2. To investigate the asymptotic behavior, just the points which overlap with the full blue line part were used to fit the parameters, with the dashed part only an extension provided for completeness.

The depletion induced by the interaction strength explored here is not the unique process which cause deviations from meanfield. The trap potential can play an important role as well, particularly in time-dependent cases. Nonetheless, the fragmentation induced by the trap usually requires a smaller number of IPS in the description than for strong interaction regimes. This effect is mostly related to the origin of each operator. While the first is of one-body nature the second involves pairs, which usually influences high order correlation functions, contrary to the trap potential, which all information must be contained in $1-$RDM. An example of trap induced fragmentation that was reproduced with this thesis codes is provided in Ref. [113].

With these tests presented here, along with all control parameters established in the previous chapter, the codes were widely tested, in all cases behaving as expected. The next step was to evaluate relevant studies that could generate an impact in some field. In the following sections, the problem of superfluid fraction of few bosons in the presence of a weak link is worked out beyond mean field approximation, highlighting the discrepancy to the GP prediction and addressing correlation as a candidate to explain the loss of superfluid fraction, what is not feasible in the mean field approach.

4.2 Superfluid fraction in annular geometry

The concepts of superfluidity [1, 62, 114] and Bose-Einstein condensation [19, 20] have dominated the research of cold bosonic systems. The presence of one does not necessarily imply the other, whereas superfluidity is related to dissipationless flow due to a minimum required energy to create excitations, Bose-Einstein condensation is characterized by majority occupation of one single particle state. Superfluid systems with a very small condensation fraction around 10%, like liquid helium, are well known [55, 115], thereby characterizing independent effects.

Nevertheless, many reports explore the superfluidity features of a BEC, as dilute cold bosonic gases are able to present both phenomena simultaneously [116]. Especially, persistent flow, a hallmark of superfluidity, has been reported for a BEC trapped in a ring shape format early in Ref. [117] and later in Ref. [118] in the presence of a tunable weak link. This boosted the interest to quantitatively study properties of the system due to a possible connection and quantum analogy with superconducting quantum interference devices (SQUID) [119].

Ring geometries provide a suitable platform to study persistent currents and quantum coherence. In the last few years, there has been much interest in annular condensates, especially in the context of the atomtronics [109, 120]. Many works studied several properties on imposing rotation for a BEC confined in a ring shape geometry, observing hysteresis ("swallow tail loops") [121–124], excitation mechanisms [125–127], spin superflow [128, 129] and superfluid fraction [63]. Former theoretical studies rely mostly on the GP equation that set a clear limitation on controlling the interactions to suppress the depletion from the condensate [130, 131]. Here, this theme is studied in both approaches, meanfield and MCTDHB, highlighting their differences, with the MCTDHB also allowing an independent characterization of superfluidity and condensation as well as beyond meanfield features.

In the following, a beyond meanfield study on the superfluid fraction of a gas of few bosons at zero temperature in the presence of a tunable weak link moving in a periodic system (an effective ring) is performed using the MCTDHB to show the loss of the superfluid fraction under a wide range of the physical parameters. For different rotating frequencies, we will found that the ground state energy remains periodic but with a different profile depending on the barrier height, and this periodicity implies a decrease on

the current fraction for fast rotating barriers. With the rotation frequency close to zero, our results show that increasing sufficiently the barrier, the superfluid fraction eventually drops to zero regardless of the interaction strength and number of particles. Also, the condensate fraction depends almost exclusively on the interaction strength, which shows independence of superfluidity and condensation. Eventually, the correlation functions are proposed to explain the superfluidity behavior.

4.2.1 Model and methods

The specific form of a barrier is generally unknown from an experimental perspective, though we must be able to define it through its thickness and height. As most of the experiments use lasers to physically implement a barrier [118], the height in the model plays the principal role as it is directly related to the laser beam intensity, while the thickness is determined by the laser beam width. An approach based on Dirac delta function for the barrier has been reported [11], which implies zero thickness. In any case, for a barrier rotating with velocity v, in the laboratory frame we thus have the one-body term of the Hamiltonian in the general form

$$h(t) = -\frac{\hbar^2}{2m}\frac{\partial^2}{\partial\bar{x}^2} + U(\bar{x} - vt) \; ; \quad \bar{x} \in (-\pi R, \pi R], \tag{4.2}$$

for a ring of radius R, where a specific form for U is chosen ahead. The two-body part is assumed to be described by an effective contact interaction $V(\bar{x} - \bar{x}') = g_{1D}\delta(\bar{x} - \bar{x}')$, where g_{1D} is related to the transverse harmonic trap frequency and the scattering length of the atoms [103]. Using the unitary transformation to move to the rotating frame, $\exp(vt\partial/\partial x)$, the time dependence of Eq. (4.2) is removed, resulting in the following many-body Hamiltonian in the second quantization formalism

$$\hat{H} = \int_{-\pi R}^{\pi R}dx \left\{ \hat{\Psi}^\dagger(x) \left[\frac{\hbar^2}{2m} \left(i\frac{\partial}{\partial x} + \frac{mv}{\hbar} \right)^2 + U(x) \right] \hat{\Psi}(x) + \frac{g_{1D}}{2}\hat{\Psi}^\dagger(x)\hat{\Psi}^\dagger(x)\hat{\Psi}(x)\hat{\Psi}(x) \right\}, \tag{4.3}$$

where $x = \bar{x} - vt$.

For numerical simulation purposes, the following system of units is assumed: length measured in units of (πR), density probability/particle in units of $(\pi R)^{-1}$ and energy by $\hbar\zeta$, where $\zeta = (\hbar/2m\pi^2R^2)$. Moreover, we introduce the dimensionless parameters

$\Omega = mRv/\hbar$ and $\gamma = 2m\pi R g_{1D}/\hbar^2$. In numerical computations, all these transformations yield the orthonormalization condition for the set of IPS $\int_{-1}^{1} dx \phi_l^*(x,t)\phi_k(x,t) = \delta_{lk}$, where x must be interpreted in units of πR in the integral.

4.2.2 Energy spectrum and superfluid fraction definition

In the absence of a barrier, the single-particle energy levels as a function of Ω are parabolas given by $E_j/(\hbar\zeta) = (j-\Omega)^2\pi^2$, each one defined by the winding number of the phase (j), centered at $\Omega_j = j$, and crossing each other at $\tilde{\Omega}_j = (j+1/2)$ [123].

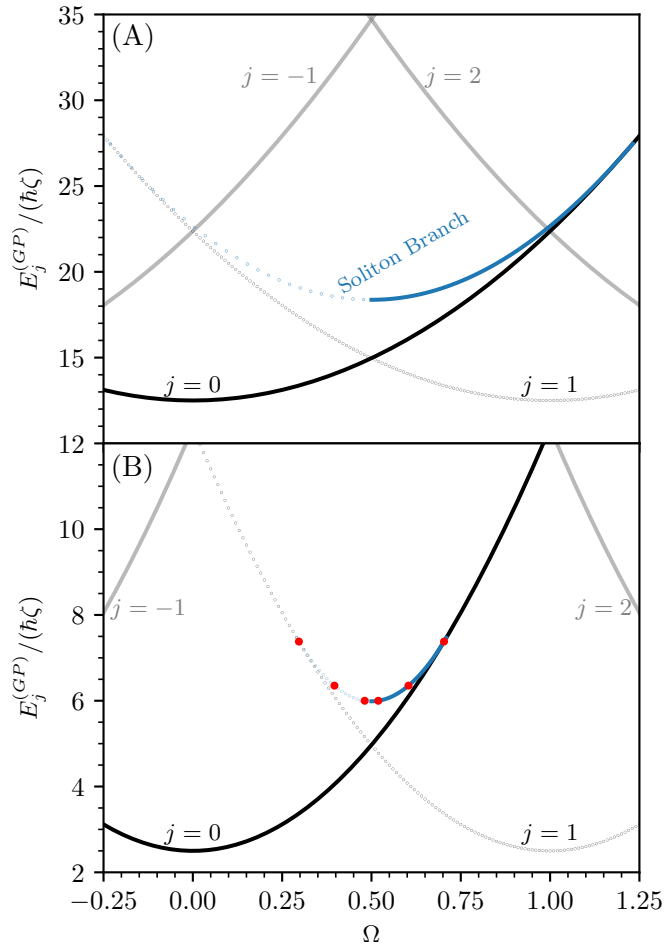As a first approach, we use the GP equation once the interaction is included in the

Figure 4.4: Energy per particle from the GP equation as a function of Ω for different winding numbers (j) with (A) $\gamma(N-1) = 50$ and (B) $\gamma(N-1) = 10$. In both cases the soliton's energy is depicted in blue, where the dotted part has winding number $j = 1$ and the full line $j = 0$, connecting the parabolas with corresponding winding numbers. Other values of winding numbers are shown in gray. The red dots are used in Fig. 4.5 to show examples of the soliton phases.

description. In this case, still in the absence of the barrier, there are two kinds of analytical solutions. One with constant density, which results in the same energy of single-particle case, with the addition of an interaction contribution, yielding $E_j^{(GP)}/(\hbar\zeta) = (j-\Omega)^2\pi^2 + \gamma(N-1)/4$ as average energy per particle. The other is a soliton given in terms of Jacobi elliptic functions [132,133] that exists for a finite range of values of Ω, where the extension of this range depends on the interaction strength (In the Appendix B the soliton solutions are derived)[1]. Fig. 4.4 shows an energy landscape of the analytical solutions of the GP equation with the soliton energy branch connecting two parabolas of constant density, where the dotted lines have winding number $j = 1$ and the filled line $j = 0$. Other winding number energies are shown in light gray.

In Fig. 4.5 the phase of solitons are presented for some values of the dimensionless rotation Ω. The soliton solutions exhibit a transition between different winding numbers and for increasing Ω a discontinuity in phase occurs at $\Omega = 0.5$, going from $j = 1$ to $j = 0$. Moreover, these solutions yield what is known as a "swallow-tail" loop in the energy shown in Fig. 4.4(A) and (B), which is related to a hysteretic behavior [121–123,134]. The soliton branch in Fig. 4.4 is an excited state and will not be further discussed here, since the aim of the present work is to measure the superfluid fraction of the ground state. In addition, Fig. 4.4 reveals that the ground state energy has a periodic behavior with respect to the rotation Ω, with kinks where the parabolas cross each other at $\tilde{\Omega}_j = (j + 1/2)$. This

---

[1]The soliton solution are also used in results showed in the next section, but with a different aim, so the notation in appendix B is not fully compatible with the units defined above
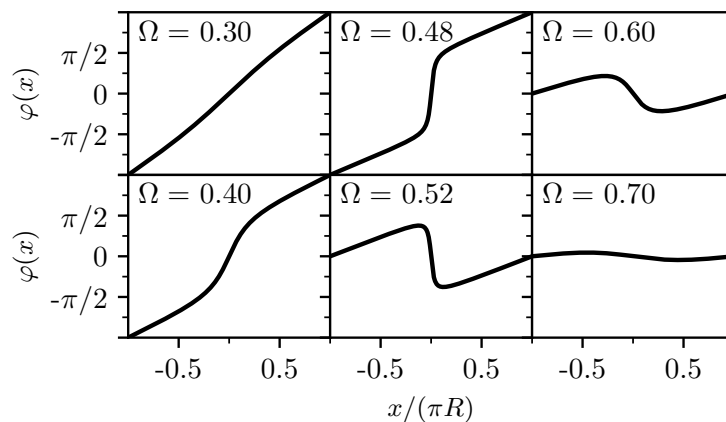

Figure 4.5: Phase profile of the soliton solution $\varphi(x)$ for some values of Ω corresponding to the red dots in 4.4(B). An abrupt transition occurs at $\Omega = 0.5$ that implies a transition in the winding numbers, from $j = 1$ to $j = 0$.

periodic structure remains even in the presence of a barrier but with soft peaks instead of kinks at $\tilde{\Omega}_j$, as will be shown later. An important fact is that we can relate the mass current circulation with the energy, and use this periodicity to understand what happens to the current under action of fast rotating barriers.

Superfluid fraction derivation

Here, a derivation of mass current by looking at the time variation of the number of atoms within the range $[x_1, x_2] \subseteq [-\pi R, \pi R]$ is presented, based on

$$\frac{\mathrm{d}}{\mathrm{d}t} \int_{x_1}^{x_2} \mathrm{d}x \, \langle \Phi(t)|\hat{\Psi}^\dagger(x)\hat{\Psi}(x)|\Phi(t)\rangle = \frac{i}{\hbar} \int_{x_1}^{x_2} \mathrm{d}x \, \left\langle \left[\hat{H}, \hat{\Psi}^\dagger(x)\hat{\Psi}(x)\right]\right\rangle_t, \tag{4.4}$$

where $\langle \cdot \rangle_t$ means the expectation value for an arbitrary time-dependent many-body state $|\Phi(t)\rangle$. Using Eq. (4.3) with the usual commutation relation for the boson field operator $[\hat{\Psi}(x), \hat{\Psi}^\dagger(x')] = \delta(x-x')$ to evaluate the commutator of the Hamiltonian with the density operator, the only terms that contribute are those carrying a derivative, and yield

$$\left[\hat{\Psi}^\dagger(x)\hat{\Psi}(x), \hat{H}\right] = -\frac{\hbar^2}{2m}\left(\hat{\Psi}^\dagger(x)\frac{\partial^2\hat{\Psi}(x)}{\partial x^2} - \frac{\partial^2\hat{\Psi}^\dagger(x)}{\partial x^2}\hat{\Psi}(x)\right)$$
$$+ i\hbar v\left(\hat{\Psi}^\dagger(x)\frac{\partial\hat{\Psi}(x)}{\partial x} + \frac{\partial\hat{\Psi}^\dagger(x)}{\partial x}\hat{\Psi}(x)\right). \tag{4.5}$$

It is straightforward to factor out the derivative with respect to x, and further using Eq. (4.5) in Eq. (4.4) yields

$$\frac{\mathrm{d}}{\mathrm{d}t}N([x_1, x_2]; t) = -\left[\langle\hat{J}(x_2)\rangle_t - \langle\hat{J}(x_1)\rangle_t\right], \tag{4.6}$$

where $N([x_1, x_2]; t) \doteq \int_{x_1}^{x_2} \mathrm{d}x \langle\Phi(t)|\hat{\Psi}^\dagger(x)\hat{\Psi}(x)|\Phi(t)\rangle$ is introduced and the particle number current operator $\hat{J}(x)$ is given by

$$\hat{J}(x) = -\frac{i\hbar}{2m}\left(\hat{\Psi}^\dagger(x)\frac{\partial\hat{\Psi}(x)}{\partial x} - \frac{\partial\hat{\Psi}^\dagger(x)}{\partial x}\hat{\Psi}(x)\right) - v\hat{\Psi}^\dagger(x)\hat{\Psi}(x). \tag{4.7}$$

The 1-RDM $\rho^{(1)}(x|x'; t)$ can be used within its diagonal representation in Eq. (2.94) to provide a formula for the average of current operator related to the natural orbitals.

Specifically, the average current becomes a superposition as $\langle \hat{J}(x) \rangle_t = \sum_k j_k(x,t)$, where

$$j_k(x,t) = -\left[\frac{i\hbar}{2m} \left(\psi_k^* \frac{\partial \psi_k}{\partial x} - \psi_k \frac{\partial \psi_k^*}{\partial x} \right) + v|\psi_k(x,t)|^2 \right] Np_k(t), \tag{4.8}$$

with $p_k(t)$ the respective eigenvalues of $\rho^{(1)}$.

For the ground state, the current $\langle \hat{J}(x) \rangle_t$ must be independent of position and time, because the density is not time dependent. If we further average it over a period in the counter direction of the barrier velocity, yields

$$\langle \rho_s \rangle(v) \doteq \tau \frac{1}{2\pi R} \int_{\pi R}^{-\pi R} \mathrm{d}x \left(\frac{\langle \hat{J} \rangle}{N} \right), \tag{4.9}$$

where $\tau = 2\pi R/v$ is the period of barrier rotation. This quantifies the mean fraction of particles that go through the counter direction of the barrier in one period, that is from πR to $-\pi R$ indicated by the limits of integration taken. Therefore, if $\langle \rho_s \rangle(v)$ takes the value 1, means a perfect superfluid since all the particles are flowing with velocity $-v$ in the rotating frame, that is, they remain at rest for an observer in the laboratory frame. Relations with other observables can be established, for instance, using the average momentum per particle

$$\langle \rho_s \rangle(v) = \left(1 - \frac{\langle \hat{p} \rangle}{mv} \right), \quad \hat{p} = -\frac{i\hbar}{N} \int_{-\pi R}^{\pi R} \mathrm{d}x \, \hat{\Psi}^\dagger(x) \frac{\partial}{\partial x} \hat{\Psi}(x), \tag{4.10}$$

and a relation with the energy, by taking the derivative with respect to the barrier velocity

$$\langle \rho_s \rangle(v) = \frac{1}{Nmv} \frac{\partial E}{\partial v}, \quad E = \langle \hat{H} \rangle. \tag{4.11}$$

The equation above can also be identified by the ratio between the moment of inertia of the atoms and the moment of inertia of a rigid body. Using $v = \omega R$, yields

$$\langle \rho_s \rangle(\omega) = \frac{1}{NmR^2} \left(\frac{1}{\omega} \frac{\partial E}{\partial \omega} \right) = \frac{I(\omega)}{I_{\mathrm{cl}}}. \tag{4.12}$$

The superfluid fraction at rest (or simply superfluid fraction), denoted here by $\langle \rho_s \rangle_0$ can be defined by taking the limit of $v \to 0$ in any of the Eqs. (4.9, 4.10, 4.11, 4.12) and was studied in this way in previous works [1,62,63,135]. With the dimensionless system of units and parameters introduced at the end of section 4.2.1, we have a suitable expression

for numerical calculations, defining $\epsilon \doteq E/(\hbar\zeta)$,

$$\langle\rho_s\rangle(\Omega) = \left(\frac{1}{2\pi^2 N\Omega}\frac{\partial\epsilon}{\partial\Omega}\right), \quad \langle\rho_s\rangle_0 \doteq \lim_{\Omega\to 0}\langle\rho_s\rangle(\Omega). \tag{4.13}$$

For arbitrary rotation values, $\langle\rho_s\rangle$ is not necessarily positive. This occurs because of the quantization of angular momentum states, which can possibly change the majority occupation of some definite momentum quantum number to another, for instance, in the transition point between the parabolas showed in Fig. 4.4. At these points, the particles eventually flow quicker than the barrier.

In the following, the MCTDHB was applied to find the ground state through imaginary time propagation for several parameters, first focusing in the effect of rotation. Fig. 4.6 illustrates the behavior of the ground state energy in panel (A) and the current fraction in
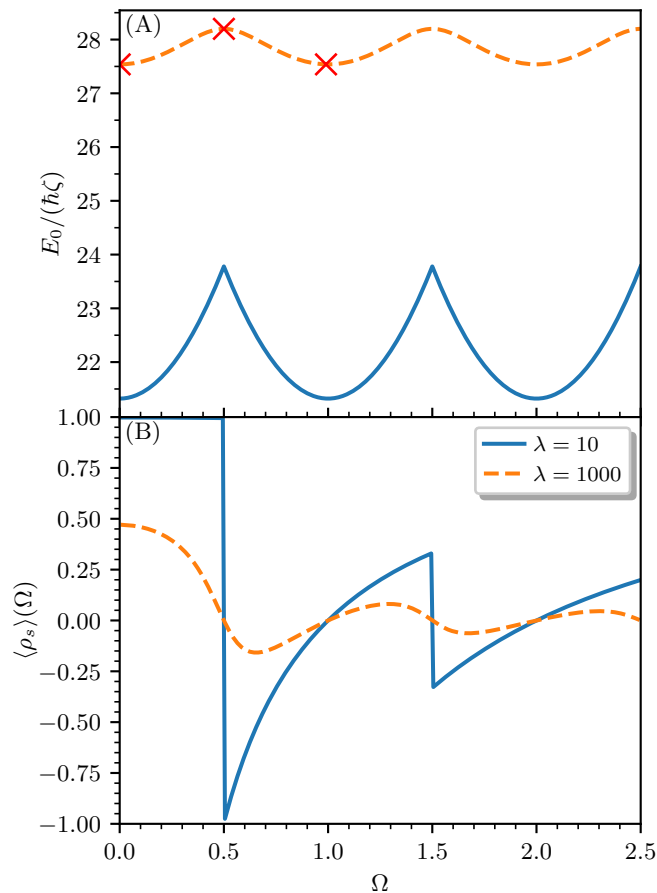

Figure 4.6: Ground state energy (A) and current fraction (B) for 11 particles as a function of dimensionless rotation velocity Ω in the rotating frame. The ground state energy remains periodic as it was in Fig. 4.4 but with a different landscape depending on the barrier height λ, and this periodicity implies a decrease on the current fraction for fast rotating barriers. We used $\gamma = 10$ and $M = 5$ IPS in the MCTDHB method.

panel (B) as a function of the dimensionless barrier frequency Ω for two different barrier heights, where the specific form used in Eq. (4.2) was

$$U(x) = \begin{cases} (\hbar\zeta\lambda)\cos^2\left(\dfrac{x}{2R\sigma}\right) & \text{if} \quad |x| \leq \pi R\sigma \\ 0 & \text{if} \quad \pi R \geq |x| > \pi R\sigma \end{cases}, \tag{4.14}$$

where λ denotes the barrier height in dimensionless units and the width was taken fixed at $\sigma = 0.1$.

The energy of the ground state in Fig. 4.6(A) has a period 1 with respect to dimensionless rotation frequency for both cases of weak and strong barriers, while the difference relies on the maximum that occurs at $\Omega_j = j$, that is sharp or smooth depending on the height λ. The superfluid fraction in Fig. 4.6(B) was computed using Eq. (4.13) with finite differences to take the derivative. It shows a periodic behavior with a damped amplitude as function of Ω, due to the periodicity of energy. According to Eq. (4.13), the amplitude is damped by a factor of $1/\Omega$. In the regions where $\langle\rho_s\rangle(\Omega) < 1$, the average momentum must increase together with the barrier velocity according to Eq. (4.10). Indeed, that is what occurs in the lower panel of Fig. 4.7 that shows the angular momentum distribution for some values of Ω. Moreover, there is a critical dependence of the superfluid fraction
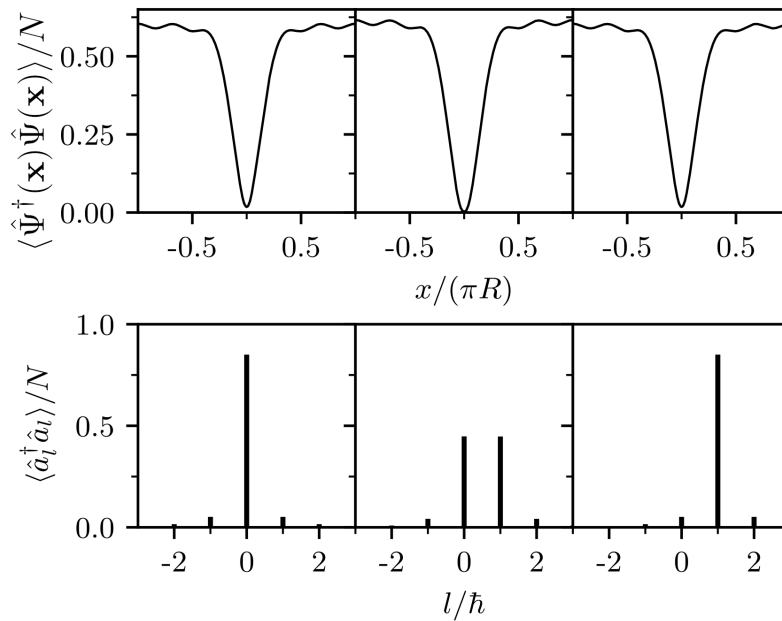

Figure 4.7: Probability distribution as a function of position (upper panel) and angular momentum distribution (lower panel) for barrier height $\lambda = 1000$. From left to right $\Omega = 0, 0.5, 1.0$, corresponding to red crosses in Fig. 4.6. As used in Fig. 4.6, here $\gamma = 10$, $N = 11$ particles and $M = 5$ IPS.

on the barrier height as Ω goes to zero, which is explored in the following.

4.2.3   Barrier effect on superfluid fraction

Numerical calculations of the superfluid fraction were carried out here using Eq. (4.13), finding the ground state by imaginary time propagation for $\Omega = 0$ and $\Omega = 0.02$ to approximate the derivative in $\Omega = 0.01$ and thus obtain $\langle \rho_s \rangle (0.01)$. As shown by Fig. 4.6, the slope of current fraction goes to zero as $\Omega \to 0$, therefore, the value at $\Omega = 0.01$ could be used as the proper superfluid fraction, since the difference $\langle \rho_s \rangle_0 - \langle \rho_s \rangle (0.01)$ is very small. To assure this method validation, the result was compared with Eq. (4.10) calculated at $\Omega = 0.02$, to check if there was no appreciable (less than 1%) variation on the estimation of superfluid fraction using an extrapolation.

In Fig. 4.8, the decrease of superfluid fraction for an increase of the barrier height λ is shown for different number of particles and interaction strengths. The tunneling of particles through the barrier becomes harder as the barrier height is increased, with the atoms acquiring momentum more easily as higher is the barrier, which can eventually drag all the particles. This easy momentum gain for large values of λ is responsible for the loss of superfluid fraction $\langle \rho_s \rangle_0$, as it imposes a rigid body rotation according to Eq. (4.12). It can also be noted that the superfluid fraction decreases more rapidly for fewer particles
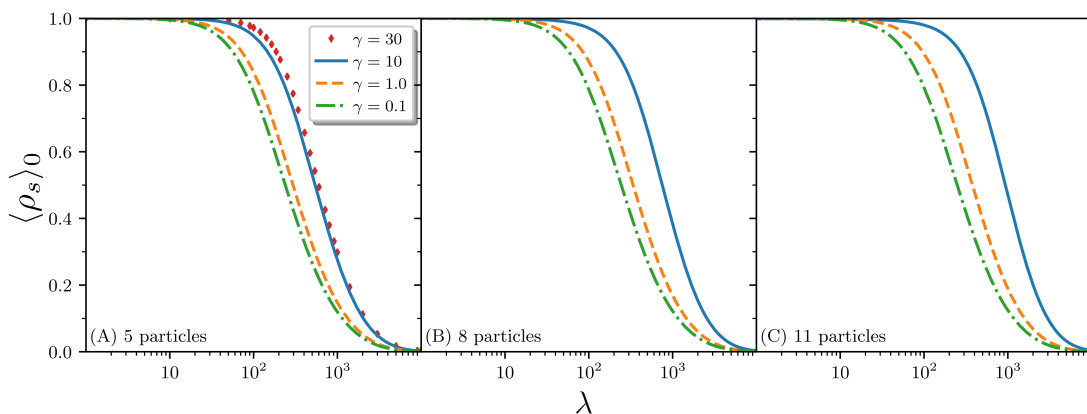

Figure 4.8: Decrease of superfluid fraction for different number of particles and interaction strength (γ) due to increasing of the barrier height (λ). All the cases share the common feature to be a perfect superfluid as the barrier becomes vanishing small, soon or later depending on the number of particles and interaction strength. For very high barriers all particles are dragged together, imposing a rigid body rotation to the system. The number of IPS was chosen as needed to converge the results, where for $\gamma \leq 10$, $M = 5$ was used while for $\gamma = 30$, $M = 9$ was used.
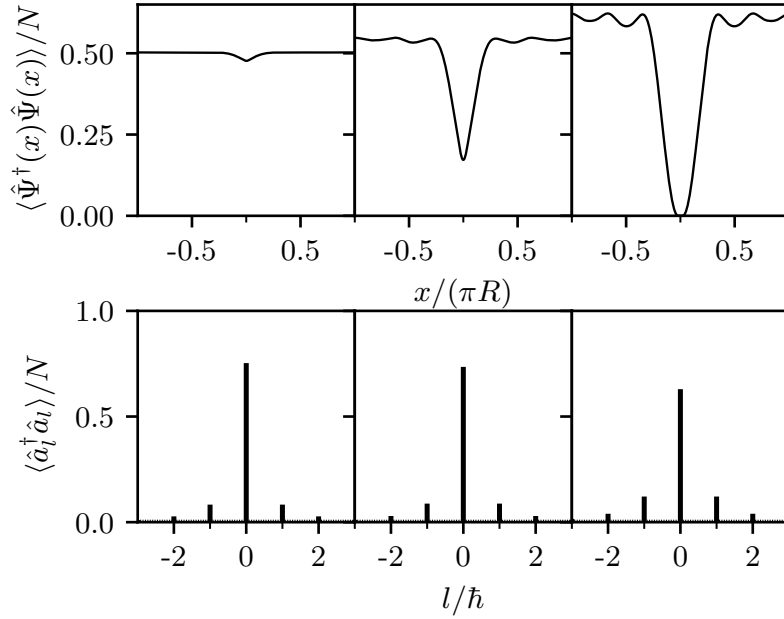
Figure 4.9: Probability distribution of position(upper panel) and angular momentum(lower panel) for five particles, $\Omega = 0$, $\gamma = 30$ and different barrier heights $\lambda = 10, 200$ and 10000 in the left, center and right columns respectively. The density distribution vanishes for $\lambda > 10^3$ at the peak of the barrier in $x = 0$, despite that there is just a slight increase on the width of the angular momentum distribution. As mentioned in Fig. 4.8, for $\gamma = 30$ we needed nine IPS in simulations.

and smaller interaction strength, however, these parameters have a small impact in the general form of the curves $\langle \rho_s \rangle_0$ as a function of λ.

As can be seen in the upper panel of Fig. 4.9, the barrier height λ influences mostly the density at its peak, while the effect over the momentum distribution is a slight increase in its variance, but preserving the average angular momentum $\langle \hat{L} \rangle = 0$, as can be checked in the lower panel. Therefore, the angular momentum distribution is not very revealing about the behavior of the superfluid fraction at rest, differently from the case for nonzero rotation shown in the lower panel of Fig. 4.7. Nonetheless, the density drastically changes as the barrier height increases, hence a more detailed study of $1-$RDM is suitable to complete the analysis.

It is worth noting that this loss of the superfluid fraction due to the increase in the barrier height is not related to the condensate fraction. As can be inferred from Table 4.1, the condensate fraction depends mostly on the interaction strength and is minimally affected by the barrier height, particularly for small values of γ.

The difference between the MCTDHB and the mean field theory was evaluated in

	Interaction strength (γ)		
N	1	10	30
11	0.9936 / 0.9920	0.92 / 0.89	-
8	0.9946 / 0.9935	0.92 / 0.88	-
5	0.9962 / 0.9956	0.91 / 0.88	0.75 / 0.70

Table 4.1: maximum/minimum condensate fraction computed over the set of values λ used along the curves in Fig. 4.8. The maximum and minimum values for each case have little influence from the barrier height whereas the superfluid fraction maximum and minimum values go from 1 to 0 respectively. For $\gamma = 30$, only calculations with five particles were feasible due to the code limitations when Ref. [64] was published. The number of IPS used follows the ones mentioned in Fig. 4.8 depending on γ.
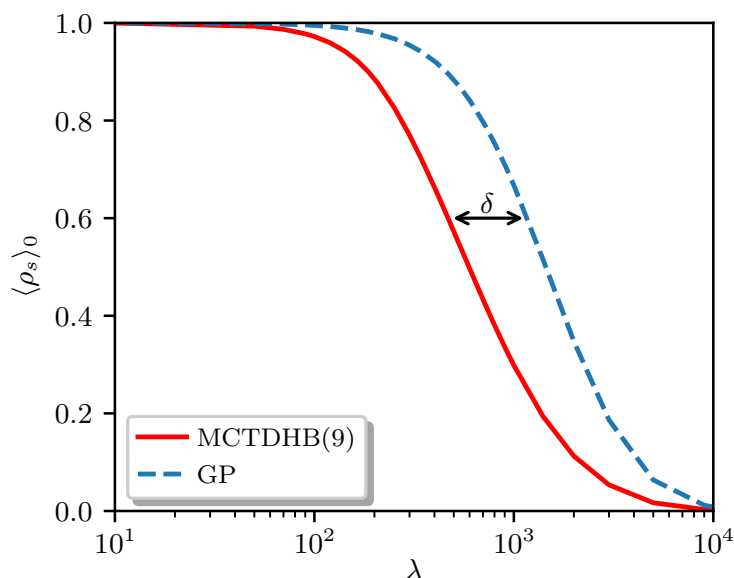

Figure 4.10: Comparison between the superfluid fraction predicted by mean field GP equation (blue dashed line) and the MCTDHB with nine IPS (full red line) for five particles and $\gamma = 30$, as function of barrier height λ. δ indicate the gap between the curves.

terms of the superfluid fraction in Fig 4.10. In this case, the same values are predicted in the limits $\lambda \to 0$ and $\lambda \to \infty$, nonetheless, between these values, a large gap δ is found between the superfluidity curves. For instance, the values $\bar{\lambda}$ where $\langle \rho_s \rangle_0$ goes below 0.6 are $\bar{\lambda}_{\mathrm{MCTDHB}} \approx 468$ and $\bar{\lambda}_{\mathrm{GP}} \approx 1160$, resulting in an appreciable difference of $\delta \approx 692$. In another way, to explore this difference, $\bar{\lambda}_{\mathrm{MCTDHB}} < \bar{\lambda}_{\mathrm{GP}}/2$ to have less than 60% of superfluid.

Since the MCTDHB provides many-body quantities beyond mean field approach, it was used to investigate how the tunneling amplitude is affected by the barrier height, that is, the transition amplitude for the system to move a particle from x to x'. This can be achieved with $|\langle \hat{\Psi}^\dagger(x') \hat{\Psi}(x) \rangle|^2$ weighted by the probabilities to find these particles

in respective positions x and x'. This is directly related to the first order correlation function, which from the general definition in Eq. (2.97) is simply

$$g^{(1)}(x|x') = \frac{\rho^{(1)}(x|x')}{\sqrt{\rho^{(1)}(x)\rho^{(1)}(x')}}, \tag{4.15}$$

where the notation with vertical bars was introduced in section 2.4 to separate the arguments of the field operators creating or destroying particles in $p-$RDM definition.

The values of $g^{(1)}$ shall be drastically affected by the barrier and must have an abrupt variation as $xx' > 0$ changes to $xx' < 0$, since the tunneling must be much harder if the shortest distance between two points has the barrier in the middle. Reminding that the system is periodic, this discussion applies just at the vicinity of either x or x' being zero, because if $(x/\pi R)(x'/\pi R) = -1$, they are actually the same point in the ring.

The effect of barrier height mentioned above is in agreement with the images in Fig. 4.11 that maps $|g^{(1)}(x|x')|^2$ values to colors. In panel (A), in the presence of a weak barrier, it depends approximately only on $|x - x'|$, while in panel (B) this symmetry is lost, with an abrupt variation near at the barrier peak, x or x' approximately zero. Therefore, high barriers split the image in four square blocks, with the darker regions (small normalized tunneling probabilities) located on $xx' < 0$. This is consistent with previous studies in Ref. [136], despite the different boundary conditions and interaction regimes.

It is important to stress the relevance of applying a method that allows us to compute such many-body quantities, as $|g^{(1)}(x|x')|^2$ would be identical to 1 for all x and x' in case one uses the GP equation, that corresponds to just one eigenstate of $\rho^{(1)}(x|x')$. Therefore, this first order correlation function, besides its relation to the tunneling amplitude, provides us a measure of how well the system can be described by a product state that corresponds to the meanfield approach.

Correlation functions became more important in the past few years due to experimental advances for measuring them [137, 138]. Recently, hybrid techniques of experimental methods and machine learning algorithms show promising results towards facilitating the correlations measure processes [139]. In this scenario the MCTDHB provides a more general and flexible platform to calculate correlations, specially for system with few particles, whereas some other approaches based on Bogoliubov description on top
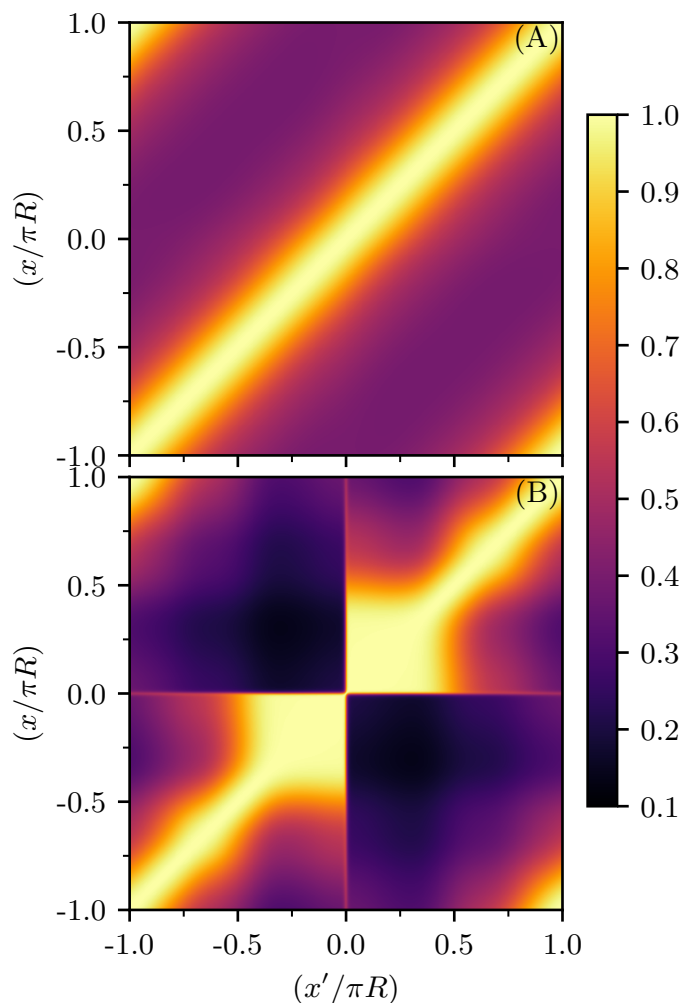
Figure 4.11: $|g^{(1)}(x|x')|^2$ mapped to colors in the ring, for 5 particles and $\gamma = 30$. Values of barrier height used are $\lambda = 10$ in (A) and $\lambda = 10^4$ in (B) but sharing the same color scale. Here, nine IPS were used in the numerical simulations.

of a meanfield state implies restrictions on interaction strength and many-body state fragmentation [140, 141].

In the following, a collection of results about dynamical properties of persistent currents are shown within the same physical system of bosons trapped in a ring geometry.

4.3 Dynamical properties of persistent currents

Persistent currents are characterized by frictionless flow of a gas within its container, which is the annular trapping potential in the present case. This effect was experimentally observed first in Ref. [117] and later in Ref. [118] including a potential barrier emulating a defect in the trapping container to analyze the current decay. The latter provides a

probability function for observing or not the flow imposed to the initial state depending on the interaction and barrier height [118, Fig. 2], which motivates the study presented in the following.

Although the ground state for a nonrotating trap have zero circulation, the persistent flow is associated with the presence of metastable states, which are local minima of the energy as function of the angular momentum. These metastable states are separated by local maxima, which depend on the system's configuration and can provide extremely long-lived quantized currents, robust against perturbations, with duration near one minute in experiments [118,142]. Fig. 4.12 illustrates qualitatively the energy landscape of low-lying states with respect to angular momentum per particle with arrows indicating the decay processes.

The energy spectrum depicted in Fig. 4.12 contains only the lowest energy state for each angular momentum, which is also known as the yrast line[2]. Apart from the qualitative illustrations, the first rigorous formulation for these energy minima with periodic dependence on angular momentum was first pointed out by Bloch decades ago [144], however, only recently the full spectrum was obtained, including all excitations [145]. The yrast spectrum was also investigated in binary mixtures [146] and in the Tonks-Giradeau regime [147].

With the inclusion of a container defect through a potential that breaks the transla-

---

[2]The origin of the term comes from Swedish *yr* meaning dizzy, with *yrast* denoting its superlative [143].
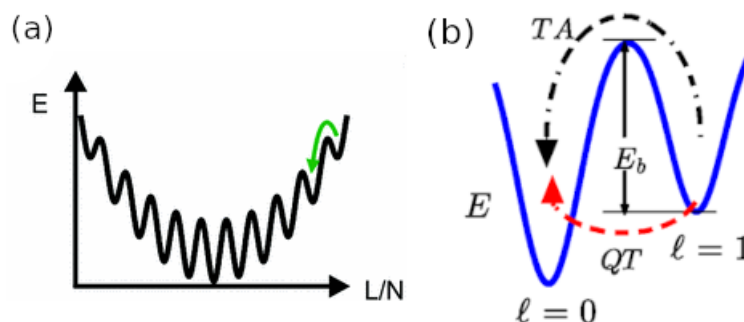

Figure 4.12: Energy landscape and metastability illustration of persistent currents in a ring. (a) the energy minima corresponds to metastable states with integer quantized angular momentum per particle. The green arrow indicate the possible decay to lower values. (b) A zoomed frame to the global and first local minima. The local maximum serve as a barrier preventing the flow to decay to global minimum, with the Thermal Activation(TA) and Quantum Tunneling(QT) decay processes indicated by black and red arrows respectively. Illustrations taken from Refs. [127, 142].

tional symmetry, it is no longer possible to separate the angular momentum values, which will be mixed. Therefore, if an initial state with a quantized circulation is prepared, by introducing the potential with a quench for instance, not only it will pump energy in the system, but also can couple to states near the local maximum in Fig 4.12, eventually easing the decay to lower circulation values. Before discussing in details the approach used here, we need to be aware of one-dimensional description limitations and try to address in which conditions the results are valid.

4.3.1 Discussion about decay processes

In the scope of this thesis, only the quantum tunneling will be considered as our formalism is valid for negligible thermal effects. Nevertheless, some recent works studied this problem trying to simultaneously take into account finite temperatures [126, 127], which is still interesting to contrast with exclusive zero temperature effects.

The superflow interrupting agent proposed here is a potential barrier that is raised in a specific point of the ring, which must have a width much smaller than the ring circumference. The experimental protocol to realize this physical setup was first detailed in Ref. [118], where angular momentum is induced in the atoms to produce the initial flowing state and then the barrier is suddenly raised. A large collection of works approached the problem [126, 127, 148–151], however, most part of these references use techniques to approximately handle all its properties, for instance, including temperature and ring thickness. Generally, the truncated Wigner approximation and stochastic projected Gross-Pitaevskii equation are used, mainly to include finite temperature effects.

The approach suggested here is much simpler, since neither temperature nor two-dimensional effects such as vortices are present. These assumptions reduce a bit the experimental appeal of the results, but with a simpler model we aim to study intrinsic many-body properties, which can be interesting with refinement of trapping and cooling techniques. These refinements are not challenging to achieve as high resolution traps were reported recently, using the Digital Micromirror Devices(DMD) [112, 152, 153]. Fig. 4.13 shows some examples of BECs clouds generated with DMD based traps.
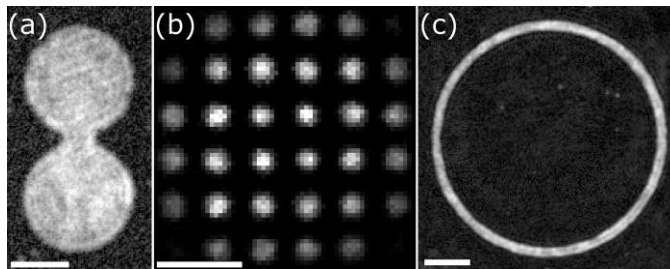
Figure 4.13: Examples of BEC images with traps designed with DMD taken from Ref. [112]. The scale white bar in the bottom of each frame corresponds to $20\mu m$. In (c) we have the interesting case for this section with a ring of $110\mu m$ diameter and $10\mu m$ radial width.

4.3.2 Analytical stationary analysis of persistent currents

Before diving into MCTDHB dynamical properties of the devised system, by quenching a barrier in an initial superflow state, a detailed derivation of the stability condition is provided using meanfield with small fluctuations in the Bogoliubov description.

The Hamiltonian represented in the momentum IPS basis for a periodic system is

$$\hat{H} = \sum_n \epsilon_n \hat{a}_n^\dagger \hat{a}_n + \frac{g_{1D}}{2L} \sum_{mnk} \hat{a}_{m+k}^\dagger \hat{a}_{n-k}^\dagger \hat{a}_m \hat{a}_n, \tag{4.16}$$

with g_{1D} representing the one-dimensional reduction of a contact interaction strength and the single particle energies given by

$$\epsilon_n = \frac{\hbar^2}{2mL^2} (2\pi n)^2, \tag{4.17}$$

with L the length of the periodic system, for every $n \in \mathbb{Z}$ with the corresponding single particle functions

$$\phi_n(x) = \frac{1}{\sqrt{L}} e^{2\pi i x/L} \equiv \frac{1}{\sqrt{2\pi R}} e^{ix/R}. \tag{4.18}$$

Differently of the standard approaches in the books [20, 21], here we need to consider small fluctuations for a majority occupation in an specific angular momentum mode $j \neq 0$, which represents the metastable persistent current state, instead of the zero momentum state.

Aiming the Bogoliubov approximation, we must keep only quadratic terms for $\hat{a}_k$ and their Hermitian conjugates for every $k \neq j$. This means that in the interaction part of the Hamiltonian will only remain terms containing at least two operators with the majority

occupied state index j, thereby,

$$\hat{H}_B = \epsilon_j \hat{a}_j^\dagger \hat{a}_j + \frac{g_{1D}}{2L} \hat{a}_j^\dagger \hat{a}_j^\dagger \hat{a}_j \hat{a}_j + \sum_{k \neq 0} \epsilon_{j+k} \hat{a}_{j+k}^\dagger \hat{a}_{j+k} +$$

$$\frac{g_{1D}}{2L} \left[4\hat{a}_j^\dagger \hat{a}_j \sum_{k \neq 0} \hat{a}_{j+k}^\dagger \hat{a}_{j+k} + \hat{a}_j \hat{a}_j \sum_{k \neq 0} \hat{a}_{j+k}^\dagger \hat{a}_{j-k}^\dagger + \hat{a}_j^\dagger \hat{a}_j^\dagger \sum_{k \neq 0} \hat{a}_{j-k} \hat{a}_{j+k} \right] . \quad (4.19)$$

The second term containing four operators in j needs additional attention for consistency with the total number of particles in the system, since

$$\hat{a}_j^\dagger \hat{a}_j = N - \sum_{k \neq 0} \hat{a}_{j+k}^\dagger \hat{a}_{j+k}. \quad (4.20)$$

In order to preserve only quadratic terms in fluctuations,

$$\hat{a}_j^\dagger \hat{a}_j \hat{a}_j^\dagger \hat{a}_j = N^2 - 2N \sum_{k \neq 0} \hat{a}_{j+k}^\dagger \hat{a}_{j+k}, \quad (4.21)$$

$$\hat{a}_j^\dagger \hat{a}_j^\dagger \hat{a}_j \hat{a}_j + \hat{a}_j^\dagger \hat{a}_j = N^2 - 2N \sum_{k \neq 0} \hat{a}_{j+k}^\dagger \hat{a}_{j+k}, \quad (4.22)$$

$$\hat{a}_j^\dagger \hat{a}_j^\dagger \hat{a}_j \hat{a}_j = N(N-1) - 2\left(N - \frac{1}{2}\right) \sum_{k \neq 0} \hat{a}_{j+k}^\dagger \hat{a}_{j+k}, \quad (4.23)$$

where in the last line $\hat{a}_j^\dagger \hat{a}_j$ is replaced using Eq. (4.20). The steps above starting from Eq. (4.20) are completely general, but in the scope of the Bogoliubov description we need a very large number of particles to effectively validate our assumption of small fluctuations on top of a condensate state. Therefore, with $N \gg 1$, we can simplify $N \pm O(1) \rightarrow N$ and obtain

$$\hat{a}_j^\dagger \hat{a}_j^\dagger \hat{a}_j \hat{a}_j = N^2 - 2N \sum_{k \neq 0} \hat{a}_{j+k}^\dagger \hat{a}_{j+k}. \quad (4.24)$$

The second part of the Bogoliubov description is the substitution of $\hat{a}_j^\dagger \hat{a}_j$ and $\hat{a}_j^\dagger \hat{a}_j^\dagger \hat{a}_j \hat{a}_j$ using Eqs. (4.20, 4.24) in the Hamiltonian $\hat{H}_B$. In addition, the remaining factor $\hat{a}_j \hat{a}_j$ as well as its Hermitian conjugate are simply replaced by N, since they are already multiplying quadratic terms in fluctuations. Therefore,

$$\hat{H}_B = N\left(\epsilon_j + \frac{G}{2}\right) + \sum_{k \neq 0} \left[(\epsilon_{j+k} - \epsilon_j + G)\hat{a}_{j+k}^\dagger \hat{a}_{j+k} + \frac{G}{2}\left(\hat{a}_{j+k}^\dagger \hat{a}_{j-k}^\dagger + \hat{a}_{j-k} \hat{a}_{j+k}\right) \right], \quad (4.25)$$

with $G = Ng_{1D}/L$, which is the meanfield energy interaction parameter.

Here, we can follow similar steps of Ref. [20, Section 8.1.1], where we must first separate in the sum the positive and negative momenta, such that

$$
\hat{H}_B = N\left(\epsilon_j + \frac{G}{2}\right) + \sum_{k>0}\left[\lambda_+^{(k)}\hat{a}_{j+k}^\dagger\hat{a}_{j+k} + \lambda_-^{(k)}\hat{a}_{j-k}^\dagger\hat{a}_{j-k} + G\left(\hat{a}_{j+k}^\dagger\hat{a}_{j-k}^\dagger + \hat{a}_{j-k}\hat{a}_{j+k}\right)\right],
$$

(4.26)

with $\lambda_\pm^{(k)} = \epsilon_{j\pm k} - \epsilon_j + G$. Thus, our problem is reduced to set the Hamiltonian

$$
\hat{h}_B = \lambda_+\hat{a}^\dagger\hat{a} + \lambda_-\hat{b}^\dagger\hat{b} + G(\hat{a}^\dagger\hat{b}^\dagger + \hat{b}\hat{a}),
$$

(4.27)

in a diagonal form. However, differently from Ref. [20] where $\lambda_+ = \lambda_-$, some additional steps will be required.

Introducing the Bogoliubov transformation as

$$
\hat{a} = u\hat{\alpha} - v\hat{\beta}^\dagger, \; \hat{b} = u\hat{\beta} - v\hat{\alpha}^\dagger,
$$

(4.28)

where the numbers u and v are assumed reals and due to the bosonic commutation relations, they must satisfy

$$
u^2 - v^2 = 1.
$$

(4.29)

Substituting the transformations (4.28) in $\hat{h}_B$ yield

$$
\hat{h}_B = \hat{\alpha}^\dagger\hat{\alpha}\left(u^2\lambda_+ + v^2\lambda_- - 2uvG\right) + \hat{\beta}^\dagger\hat{\beta}\left(v^2\lambda_+ + u^2\lambda_- - 2uvG\right) + \\
\left(\hat{\alpha}\hat{\beta} + \hat{\alpha}^\dagger\hat{\beta}^\dagger\right)\left[G(u^2 + v^2) - uv(\lambda_+ + \lambda_-)\right] + v^2(\lambda_+ + \lambda_-) - 2uvG. \quad (4.30)
$$

The complete determination of u and v is obtained with the term inside squared brackets being zero,

$$
G(u^2 + v^2) - uv(\lambda_+ + \lambda_-) = 0,
$$

(4.31)

which, together with Eq. (4.29) is solved by[3]

$$u^2 = \frac{1}{2}\left(\frac{\lambda_+ + \lambda_-}{2\tilde{\epsilon}} + 1\right), \ v^2 = \frac{1}{2}\left(\frac{\lambda_+ + \lambda_-}{2\tilde{\epsilon}} - 1\right), \tag{4.32}$$

where

$$\tilde{\epsilon} = \sqrt{\left(\frac{\lambda_+ + \lambda_-}{2}\right)^2 - G^2}. \tag{4.33}$$

With these expressions for u and v, Eq. (4.30) can be simplified as follows

$$\hat{h}_B = \hat{\alpha}^\dagger\hat{\alpha}\left(u^2\lambda_+ + v^2\lambda_- - 2uvG\right) + \hat{\beta}^\dagger\hat{\beta}\left(v^2\lambda_+ + u^2\lambda_- - 2uvG\right) + v^2(\lambda_+ + \lambda_-) - 2uvG \tag{4.34}$$

$$\hat{h}_B = v^2(\lambda_+ + \lambda_-) - 2uvG + \hat{\alpha}^\dagger\hat{\alpha}\left[(u^2 + v^2)\left(\frac{\lambda_+ + \lambda_-}{2}\right) + (u^2 - v^2)\left(\frac{\lambda_+ - \lambda_-}{2}\right) - 2uvG\right] + $$
$$\hat{\beta}^\dagger\hat{\beta}\left[(u^2 + v^2)\left(\frac{\lambda_+ + \lambda_-}{2}\right) - (u^2 - v^2)\left(\frac{\lambda_+ - \lambda_-}{2}\right) - 2uvG\right] \tag{4.35}$$

$$\hat{h}_B = v^2(\lambda_+ + \lambda_-) - 2uvG + \hat{\alpha}^\dagger\hat{\alpha}\left[(u^2 + v^2)\left(\frac{\lambda_+ + \lambda_-}{2} - \frac{2G^2}{\lambda_+ + \lambda_-}\right) + \left(\frac{\lambda_+ - \lambda_-}{2}\right)\right] + $$
$$\hat{\beta}^\dagger\hat{\beta}\left[(u^2 + v^2)\left(\frac{\lambda_+ + \lambda_-}{2} - \frac{2G^2}{\lambda_+ + \lambda_-}\right) - \left(\frac{\lambda_+ - \lambda_-}{2}\right)\right] \tag{4.36}$$

$$\hat{h}_B = v^2(\lambda_+ + \lambda_-) - 2uvG + \hat{\alpha}^\dagger\hat{\alpha}\left[(u^2 + v^2)\left(\frac{2\tilde{\epsilon}^2}{\lambda_+ + \lambda_-}\right) + \left(\frac{\lambda_+ - \lambda_-}{2}\right)\right] + $$
$$\hat{\beta}^\dagger\hat{\beta}\left[(u^2 + v^2)\left(\frac{2\tilde{\epsilon}^2}{\lambda_+ + \lambda_-}\right) - \left(\frac{\lambda_+ - \lambda_-}{2}\right)\right] \tag{4.37}$$

$$\hat{h}_B = v^2(\lambda_+ + \lambda_-) - 2uvG + \hat{\alpha}^\dagger\hat{\alpha}\left[\tilde{\epsilon} + \left(\frac{\lambda_+ - \lambda_-}{2}\right)\right] + \hat{\beta}^\dagger\hat{\beta}\left[\tilde{\epsilon} - \left(\frac{\lambda_+ - \lambda_-}{2}\right)\right]. \tag{4.38}$$

The last step is to recover the momentum, by indexing all elements used in this

---

[3]This solution is valid taking the same sign of the square root for both u and v as can be directly verified by substitution in Eq. (4.31). If different signs are chosen it will not solve the equation. Moreover, as $\hat{h}_B$ is invariant under changing simultaneous the sign of u and v, we can stick only with the positive roots.

derivation with the momentum k back in Eq. (4.26),

$$\hat{H}_B = N\left(\epsilon_j + \frac{G}{2}\right) + \sum_{k>0}\left[v_k^2(\epsilon_{j+k} + \epsilon_{j-k} - 2\epsilon_j + 2G) - 2u_k v_k G\right] +$$
$$\sum_{k>0}\left\{\hat{\alpha}_k^\dagger\hat{\alpha}_k\left[\tilde{\epsilon}_k + \left(\frac{\epsilon_{j+k} - \epsilon_{j-k}}{2}\right)\right] + \hat{\beta}_k^\dagger\hat{\beta}_k\left[\tilde{\epsilon} - \left(\frac{\epsilon_{j+k} - \epsilon_{j-k}}{2}\right)\right]\right\}, \quad (4.39)$$

where the $\lambda_\pm^{(k)}$ was replaced by its definition. For a final simplification, we can use the definition of ϵ_n in Eq. (4.17). For instance, we can apply the property $\epsilon_{j+k} - \epsilon_{j-k} = -(\epsilon_{j-k} - \epsilon_{j+k})$ and define $\hat{\beta}_k \equiv \hat{\alpha}_{-k}$ since they are independent operators to finally write[4]

$$\hat{H}_B = N\left(\epsilon_j + \frac{G}{2}\right) + \sum_{k\neq 0}\left[v_k^2(\epsilon_k + G) - u_k v_k G\right] + \sum_{k\neq 0}\hat{\alpha}_k^\dagger\hat{\alpha}_k\left[\tilde{\epsilon}_k + \left(\frac{\epsilon_{j+k} - \epsilon_{j-k}}{2}\right)\right], \quad (4.40)$$

whereas, just for completeness,

$$\tilde{\epsilon}_k = \sqrt{(\epsilon_k + G)^2 - G^2}. \quad (4.41)$$

Throughout all these steps, the difference from the traditional Bogoliubov formalism provided in the textbooks [20, 21] is the additional term inside the last square brackets, defining shifted quasi-particle energies, whereas Eq. (4.41) is the usual spectrum for a uniform gas. The explicit form of the quasi-particles excitations is

$$\epsilon_k^{(j)} = \left(\frac{\hbar^2}{mR^2}\right)jk + \sqrt{(\epsilon_k + G)^2 - G^2}, \quad (4.42)$$

with $R = L/(2\pi)$ the radius associated with the circumference length L.

In the equation above, the possibility of $\epsilon_k^{(j)}$ to be negative for some $k < 0$ indicates an energetic instability of the system, with small fluctuations being able to decrease the energy. Therefore, the system is stable if

$$\sqrt{(\epsilon_k + G)^2 - G^2} > \left(\frac{\hbar^2}{mR^2}\right)j|k|, \quad (4.43)$$

$$\epsilon_k^2 + 2G\epsilon_k > \left(\frac{\hbar^2}{mR^2}\right)^2 j^2 k^2, \quad (4.44)$$

$$G > \left(\frac{\hbar^2}{mR^2}\right)\left(j^2 - \frac{k^2}{4}\right). \quad (4.45)$$

---

[4]Note that the sums were extended for all $k \neq 0$ instead of $k > 0$ from previous steps

The largest possible result on the right side of this inequality occurs for $k = 1$. Therefore, with some additional manipulations and using the elementary parameters of the Hamiltonian, we obtain the condition

$$\frac{Ng_{1D}}{2\pi}\left(\frac{mR}{\hbar^2}\right) > j^2 - \frac{1}{4}, \tag{4.46}$$

for the persistent current with charge j to be energetically stable.

In experiments, the two most easier parameters to tune are the number of particles N and the interaction g_{1D}, but not restricted to them, one can also change the ring radius. Another notable feature about this final result is the dependence on the meanfield parameter Ng_{1D} instead of an arbitrary dependence on N and g_{1D} separately.

Another possible derivation of this result can be done entirely with the GP equation, which is shown in appendix B. The advantage of this other approach is the possibility to draw the yrast line within the meanfield description, since in the calculation is possible to obtain an arbitrary GP solution with a fixed average momentum. Moreover, it provides a slightly different condition as pointed by Eq. (B.31), which in accordance with the notation introduced here is

$$\frac{(N-1)g_{1D}}{2\pi}\left(\frac{MR}{\hbar^2}\right) > j^2 - \frac{1}{4}. \tag{4.47}$$

The only difference is the adaptation $N \to (N-1)$ in Eq. (4.46), although they become equivalent with the assumption of large number of condensed particles required in the Bogoliubov description.

In the following, the relation (4.47) is preferred to establish the stability condition for the persistent currents, since if it holds, condition (4.46) is also satisfied as $N > N - 1$ and it provides a better self-consistency to compare with numerical results as for $N = 1$ there cannot be metastability.

4.3.3 Yrast spectrum

As mentioned before, without a potential to break the translational symmetry, we can simultaneously obtain the spectrum for energy and angular momentum, thus, in a first moment, the latter can be fixed to reduce the configurational space. The most general approach to this problem is presented in Ref. [145], with a rather large number of states
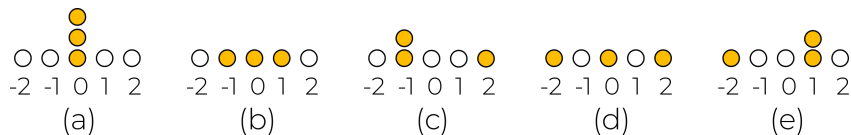
Figure 4.14: From (a)-(e) all configurations with total angular momentum $L_M = 0$ for a system of 3 particles and 5 IPS. The bare configurational space have dimension $N_c(3,5) = 35$, thus, 7 times larger than the $L_M = 0$ sector.

obtained. However, the most important for this thesis is the lowest energy band with respect to angular momenta, that is the yrast line.

Here, two approaches are used to calculate the yrast spectrum. The first is by explicit diagonalization of the Hamiltonian in Eq. (4.16) and the second is using the GP equation with constrained angular momentum as presented in appendix B. As stated in the appendix, the GP formalism lacks correlations and multiple IPS occupations, thus, it can only provide the yrast line with respect to the average angular momentum, whereas only in integer average momenta per particle the GP solution is actually an angular momentum eigenstate.

The specific reason to go for diagonalization of Hamiltonian (4.16) instead of the MCTDHB with imaginary time propagation is to avoid extra computational cost due to analytically knowing the natural IPS. As a many-particle eigenstate $|\Psi(L_M)\rangle$ of Hamiltonian (4.16) has a definite total angular momentum L_M, it implies $\langle\Psi(L_M)|\hat{a}_l^\dagger\hat{a}_k|\Psi(L_M)\rangle = n_l\delta_{kl}$, thus according to the discussion in section 2.4.1, the plane waves are actually the natural orbitals. Therefore, the IPS are frozen and the underlying multiconfigurational space is separated in sectors for each total total angular momentum, from which the blocks in Hamiltonian matrix are diagonalized separately. See Fig. 4.14 that lists examples of configurations with $L_M = 0$. Besides, in this case we can store the matrix with a sparse algorithm suitable for parallelization.

With the tweaks mentioned above to work in sectors of the multiconfigurational space, much larger spaces are achievable, where the IPS are truncated by assuming a maximum single particle momentum modulus, $l_{\max}$, for the set of plane waves (4.18). Therefore, the respective total number of IPS becomes $2l_{\max} + 1$. For instance, this approach allow us to use approximately three times more IPS than the naive treatment with the MCTDHB within the same execution time.

In Fig. 4.15 the yrast spectrum is compared with the different methodologies described in this section. In all three cases, we have the same GP interaction parameter fixed, thus,
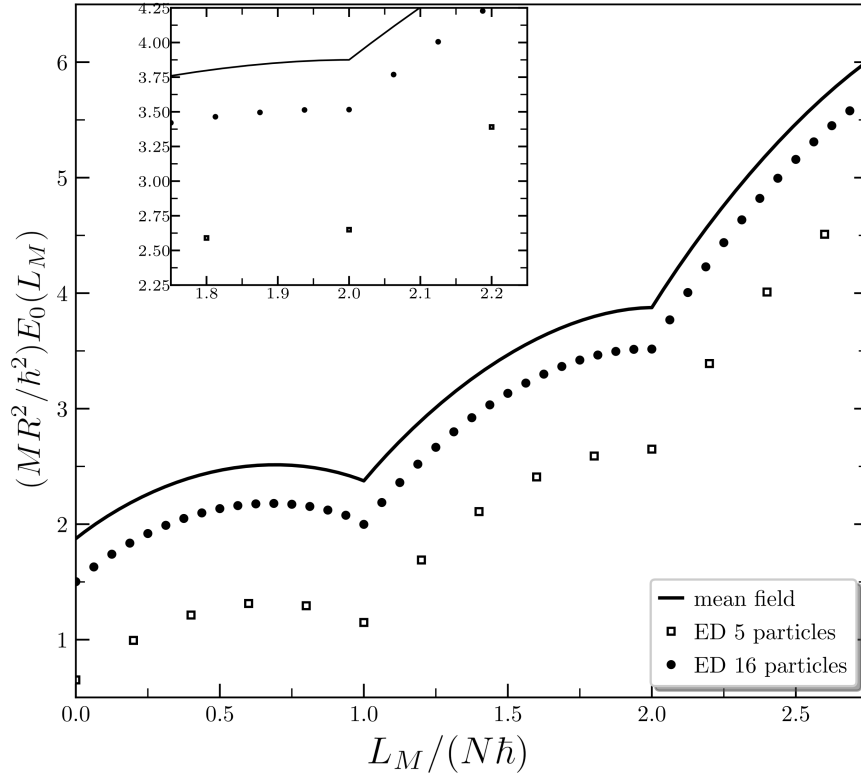
Figure 4.15: Example of yrast spectrum for different number of particles and the meanfield using $g_{1D}(N-1)mR/(2\pi\hbar^2) = 3.75$ as GP interaction parameter, which is the threshold to support persistent current with charge $j = 2$ according to Eq. (4.47). The full line correspond to the analytical solution based on the appendix B. In ED cases, the value g_{1D} used in Eq. (4.16) was adapted according to the number of particles to respect the same meanfield interaction parameter.

when the number of particles is changed in the Exact Diagonalization(ED) case, g_{1D} is adapted accordingly. For the value $g_{1D}(N-1)mR/(2\pi\hbar^2) = 3.75$ chosen, which is the threshold to provide persistent currents with charge $j = 2$, we can clearly see the local minimum in $L_M/(N\hbar) = 1$, as expected at least for the full line. Remarkably, even for low number of particles ($N = 5$) the local minimum persists, despite there is a large offset of the entire curve. Nearby $L_M/(N\hbar) = 2$ we can also see a vanishing slope from the left for the ED case (see the inset axes), which is rather surprising because we are far from a number of particles being much larger than unit.

The local minimum existence in $L_M/(N\hbar) = 1$ is robust with respect to the number of particles, despite derived in the meanfield approach, thus, there is no need to exhaustively repeat the computations to every number of particles being worked out. Nonetheless, specific values of the energy cannot be taken from meanfield computations, as there can be a large offset compared to ED.

4.3.4 Potential barrier effect on persistent currents

After an analytical derivation for the persistent current stabilization condition and the exemplification by calculating explicitly the yrast spectrum in the last section and appendix B, we can now return to the original question about the effect of a potential barrier over the flow in a ring. The main purposes is to explore beyond meanfield dynamics by quenching a potential barrier on an initial state with integer angular momentum per particle.

By introducing a potential that breaks the translational symmetry, the spectrum showed in Fig. 4.15 is no longer possible since we cannot fix the angular momentum. Nevertheless, qualitatively, for small enough barriers a similar shape should appear if one instead uses the average angular momentum to display as horizontal axis. Moreover, the potential introduced shall dynamically pump the energy in the system, easing the tunneling among the plane wave states. As a final introductory remark, another point to investigate is the implications of the barrier's shape, which may deeply influence transition probabilities between states with different angular momenta.

The Hamiltonian model is the same presented in Eq. (4.3). First, according to Fig. 4.6(A), the Lagrange multiplier is adjusted to produce a state with unit angular momentum per particle without single particle potential($U = 0$) through imaginary time propagation. At this stage, the Lagrange multiplier is only a tool for the numerical method, since otherwise the state would go to global minimum, thus it shall not be interpreted as rotation when evaluating dynamics. The classification of whether it will be a persistent current state or not, in meanfield level, is defined according to the criterion in Eq. (4.47), which according to the discussion in the previous section provide a good agreement even for small number of particles.

Once the stationary current state is prepared, it is used as initial condition for real time evolution. At this stage, the Lagrange multiplier is no longer needed, thus the system's Hamiltonian taken from Eq. (4.3) is used with $v = 0$ to study the dynamics with U describing the potential barrier. Similar to the barrier used before, here,

$$U_b(x) = \begin{cases} (\hbar \omega_R \lambda) \cos^2 \left(\dfrac{x}{2R\sigma} \right) & \text{if} \quad |x| \leq \pi R \sigma \\ 0 & \text{if} \quad \pi R \geq |x| > \pi R \sigma \end{cases} , \qquad (4.48)$$

with $\omega_R \equiv \hbar/mR^2$ set the frequency and time scales, for instance, with $\tau = 1/\omega_R$[5].
In this way, λ and σ are the dimensionless parameter to control the barrier height and
width, respectively. As before, the width is fixed for the barrier as $\sigma = 0.1$ in the
following. Naturally, a suitable parameter to compare with superflow condition (4.47) is
$\gamma_R = (N-1)g_{1D}/(\hbar\omega_R R)$, thus, as done before, within the MCTDHB we can adjust g_{1D}
when analyzing different number of particles, maintaining the initial states in the same
regions of stability.

In addition to the barrier defined above, to compare with other type of translational
symmetry breaking potentials, a lattice potential is used. The lattice is defined by

$$U_l^{(k)}(x) = (\hbar\omega_R\lambda)\sin^2\left(\frac{kx}{2R}\right), \ k \in \mathbb{N}, \tag{4.49}$$

where k is the number of peaks in the lattice.

In Fig. 4.16 the average population in the plane-wave state with unit angular mo-
mentum is shown after quenching the potential (4.48) in frames (a) and (b), while the
lattice potential (4.49) is used in (c), where $\hat{c}_l$ is the destruction operator for $\phi_l(x) \equiv$
$e^{ilx/R}/\sqrt{2\pi R}$. First, in frames (a) and (b) $\lambda = 1$ was used while the interaction varies

_____
[5]This system of units is different from before for the interaction parameter better agree with the
condition derived in Eq. (4.47). The conversion is simple though, only a factor of $2\pi^2$
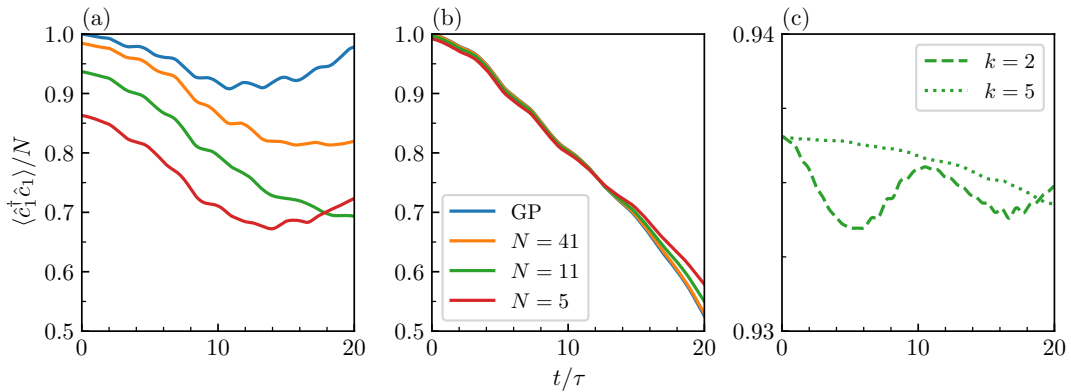

Figure 4.16: Average population on $l = 1$ state exploring different parameter values and
number of particles. (a) The barrier U_b is used with $\lambda = 1$ and $\gamma_R = 10$. (b) Same case of
(a) but with $\gamma_R = 1$. Finally in (c), the lattice potential $U_l^{(k)}$ is used with $\lambda = 0.1$, $\gamma_R = 10$
and two values for k. For this case with a lattice, only 11 particles is showed, which can
be compared with the full green line in (a). As the dimensionless interaction parameter
used here is $\gamma_R = (N-1)g_{1D}/(\hbar\omega_R R)$, the GP result is independent of the number of
particles. The number of IPS needed were 5, 9 and 11 for the number of particles 41, 11
and 5 respectively. The time scale is given by $\tau = mR^2/\hbar$.

from 10 in (a) to 1 in (b) for the dimensionless meanfield parameter γ_R. Once again, as the number of particles change for the different lines in a same frame, thus g_{1D} must be adjusted accordingly to maintain γ_R. In order to have the same initial energy pumped in the system, the lattice $U_l^{(k)}$ used in frame (c) have $\lambda = 0.1$, since the initial energy per particle introduced by a generic potential quench $U(x)$ is easily obtained by

$$\int_{-\pi R}^{\pi R} dx \rho^{(1)}(x) U(x) = \frac{1}{2\pi R} \int_{-\pi R}^{\pi R} dx U(x), \tag{4.50}$$

as the single particle probability $\rho^{(1)}(x)$ is constant.

Among some important features to mention about Fig. 4.16, the first is the good agreement with GP description in frame (b), with the orange line corresponding to 41 particles completely overlapping the blue. This agreement was expected by raising the number of particles with fixed meanfield interaction parameter as discussed in section 4.1, especially for small values of γ_R. In contrast with the case in (a), which has stronger interaction, in (b) we see an almost linear decay of the population in the state with angular momentum 1, and this can be attributed to the respective values of interaction being in different regimes according to Eq. (4.47). Note that the γ_R minimal value for the first local minimum to appear is $3\pi/2$, thus in the case presented in (b), there is no energy barrier for the transition to zero circulation state. Therefore the main difference between (a) and (b) is the amount of particles that continues to flow.

Another important point in Fig. 4.16 to emphasize is the lattice potential case in (c). Despite the energy added to the system be the same, the fraction that continues to flow is much bigger than the full gree line in (a), which share all parameters but the barrier form. Thus, the energy injected initially in the system is definitely not the unique feature to consider.

In summary, in the case presented above with two types of symmetry breaking potentials we could fulfill some expectations, as the better concordance with GP for weaker interactions and larger number of particles, besides the faster loss of particles in the flowing state for interactions below the minimum value provided by (4.47). Nonetheless, we can go beyond to provide more information about many-body observables.

Before proceeding to additional features accessible within MCTDHB, the case with 11 particles (full green line) in Fig. 4.16(a) was explored in more detail in Fig. 4.17, changing the barrier height λ. Generally, by increasing λ the current decays faster, however for
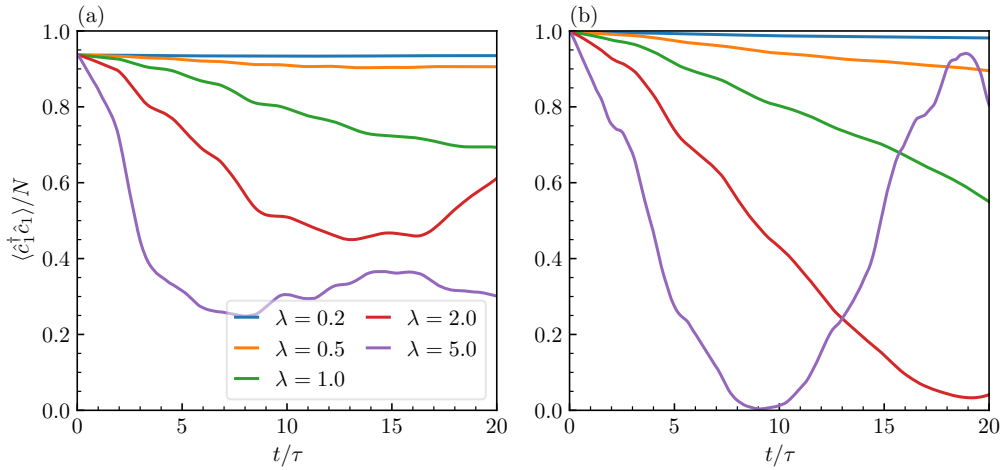
Figure 4.17: Effect of barrier height according to U_b in Eq. (4.48) for a system with 11 particles. In panel (a) $\gamma_R = 10$ and in (b) $\gamma_R = 1$. The green lines of each panel correspond to the ones in the same panels of fig. 4.16.

the cases which the interaction is below the condition (4.47), in Fig. 4.17(b), besides the initial faster loss of particles in the circulating state, there is a return to the initial value as shown by the purple line at $t \approx 19\tau$. This period with increasing number of flowing particles are generally not present with temperature included in the formalism, where the momentum of the systems only decreases in time.

The previous figures only provide part of what can be extracted from MCTDHB, and we can provide more information useful in experimental measures. Starting from Ref. [118], we can assume that independent measurements can identify the presence of a ring structure after releasing the atoms if they were in a state with quantized flowing. Actually, the images can be blurry, because generally there is only a fraction of atoms still flowing, with the rest carrying no momentum (see inset axes of Fig. 2 in Ref. [118]). Therefore, after many experimental runs one can count the number of states in which the persistent flow was observed, even addressing a flow probability.

To better understand the distribution when measuring the fraction of flowing particles, the fluctuation of operators is used here, defined as

$$\delta\hat{O} \equiv \hat{O} - \langle\hat{O}\rangle, \tag{4.51}$$

for a generic operator $\hat{O}$. Therefore, the standard deviation is simply $\sqrt{\langle(\delta\hat{O})^2\rangle}$, which can be used as dispersion for quantum expectation values. Here we look at the dispersion of the occupation numbers in the state with $l = 1$ angular momentum per particle, which
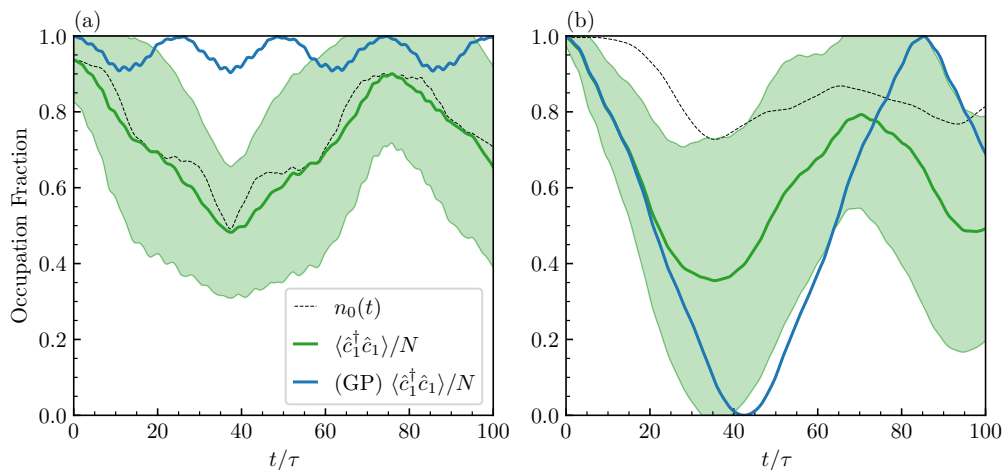
Figure 4.18: Time evolution of occupations for a system with 11 particles after a quench of the barrier U_b with $\lambda = 1$ and interaction (a) $\gamma_R = 10$ and (b) $\gamma_R = 1$. The full green lines up to $t = 20\tau$ are the same of Figs. 4.16 and 4.17 respective panels. The filled area corresponds to $\sqrt{\langle (\delta \hat{c}_1^\dagger \hat{c}_1)^2 \rangle}$ interval upwards and downwards. The black dotted line is the condensation fraction according to the largest $1-$RDM eigenvalue and the blue line corresponds to the outcome of GP equation.

provide information on how likely different measurements will produce the same outcome.

In Fig. 4.18 in addition to the average occupation in $l = 1$ state, the fluctuations are provided as a filled green interval plot, with one standard deviation up and downwards. The condensation fraction and the outcome of the GP equation are also shown to highlight a visualization of the different concepts. First, it is worth to remind that the black dotted line must start with the full green line since in the absence of the barrier the plane waves must be exactly the natural orbitals as discussed previously. Once the dynamics start, they become distinct concepts, whereas the natural orbitals are eventually superposition of plane waves. Moreover, the full blue line disconnect from the other two as the time increases, with meanfield failing to describe both. Note also that with an unique IPS in the GP description, the standard deviation is always zero, in other words, it cannot describe any fluctuations in measurements.

It is worth to emphasize that, in absence of temperature effects, Fig. 4.18 provide almost all relevant information[6] to reconstruct the statistical distribution of measuring the number of particles that are still flowing in the ring at every time instant. Another important point to stress is the visualization as a symmetric interval in the upper and

---

[6]In this case, this statistical distribution is discrete in the interval $[0, 1]$ and to fully determine it we would need all higher order moments, such as $\sqrt{\langle (\hat{c}_1^\dagger \hat{c}_1)^n \rangle}$, with arbitrary n.

lower parts of the full line, which is only a tool to show simultaneously the standard deviation with the average, but the actual form of the distribution generally neither is symmetric nor is a gaussian.

Finally, the momentum distributions are shown in Fig. 4.19 for $t = 0$ in (a) and $t/\tau = 37.5$ in (b) with the same parameters used in Fig. 4.18(b). In the centered axes, the mutual probability to find particles with angular momentum l and l' are mapped into colors, while in the top and right axes the discrete single particle momentum distribution, $\langle \hat{c}_l^\dagger \hat{c}_l \rangle / N$, are shown for each case. The specific time instant $t/\tau = 37.5$ is where the maximum uncertainty occurs according to Fig. 4.18(b), and thus, where the many-body effects are pronounced. For instance, at this moment, the most probable state to find a particle is $l = -1$ with roughly 0.6 probability, nonetheless, the mutual probability is around 0.5 for $l = l' = -1$, which is larger than 0.36 produced approximately by the multiplication of the results of single particle distributions. This show us that the probability distribution have correlated events to find more particles in $l = -1$ state. The mutual probabilities are obtained with Eq. (2.82) for $p = 2$, where the operators must corresponds to plane waves as in Eq. (4.18)[7].

As a final remark, the specific momentum distribution as shown in Fig. 4.19 is crucial to understand the specific protocol to detect the current proposed in Ref. [118]. Even if a ring shape cloud is observed after releasing the atoms, this may not mean that the majority of the particles have the same flow direction than initially. For instance, the

---

[7]This is equivalent to take Fourier transform of the field operators in the ring domain
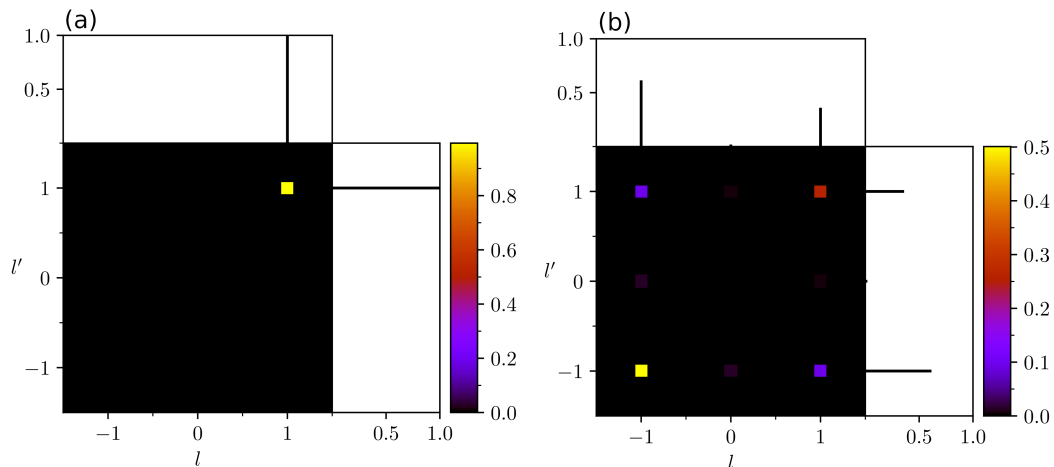

Figure 4.19: Mutual probability in momentum space for two instants (a) $t = 0$ and (b) $t/\tau = 37.5$ for the same parameters presented in Fig. 4.18(b). The additional axes at top and right of panels (a) and (b) show the single particle momentum distributions.

momentum direction can change, with the largest fraction occupying the state $l = -1$. Therefore, depending on the experimental circumstances, quantum fluctuations can play an important role in observing or not the flowing with the protocol suggested in Ref. [118], whereas the MCTDHB offers a good opportunity to access quantum fluctuations.

Chapter 5

Conclusions

Properties of bosonic gases were studied within the MCTDHB, which provides several new features beyond meanfield description with a very general methodology. As one of the approaches to study many-particle systems, the MCTDHB has a notorious advantage for time-dependent problems as it is inherently derived for this purpose and offers the capability to study many-particle systems with arbitrary precision, only limited by the numerical resources. Some other alternatives, as Monte Carlo and perturbative approximations, do not have the same appeal to study initial condition problems as showed here.

The numerical part development is one of the most challenging features in the understanding and implementation of MCTDHB. As such, the theme frequently confront us with numerical analysis techniques amid the physics, but such interdisciplinary concepts are inevitable for whoever wants to completely understand the method and implement it. Therefore, all proofs in the method's derivation and details of the numerical implementation were carefully provided in chapters 2 and 3, which are regarded as essential part of the theme.

Despite the constraints are technical, only depending on available resources, the limitations come up very quickly as the configurational space increases and in practice we cannot smoothly cover all possible regimes. For instance, the MCTDHB better suits for relatively small number of particles and in one spatial dimension, where we afford more liberty to explore strong interacting cases and better analyze the fragmentation. Nevertheless, even for a large number of particles, for instance $N > 1000$, it is possible to consider small fragmentation processes with few IPS, typically $M = 3$, in such way to

complement the meanfield description with a small fraction of depletion of the condensed state.

After all the numerical background is set, the MCTDHB can be easily adapted for a large variety of problems by changing the trapping potential, boundary conditions or the interatomic interactions. The results presented here were particularly focused in the flow properties of few bosons trapped in an annular geometry, eventually, using a barrier as potential. Nevertheless, the object of study can be easily switched, for instance with other type of single particle potentials as harmonic traps or double wells, possibly with an arbitrary time-dependence. Therefore, the MCTDHB is very adaptable for different physical setups not restricted to the ones investigated here.

Among the main results, initially, the superfluid fraction was computed for a bosonic gas analyzing all the parameters independently of the condensation fraction, in contrast to many other works where full condensation is commonly assumed. Here, the Leggett's suggestion of the superfluid fraction of an arbitrary many-particle system was adopted [1] and it could provide a computation methodology without any initial approximations, such as estimation of the sound velocity as the threshold for creating excitations. Moreover, details exclusive from many-particle features were explored, such as the translational symmetry breaking by the barrier observed in the first order correlation function, which is directly related to particles tunneling through space points. Consequently, this approach presented here can increase the interest in beyond meanfield features in superfluid characterization.

In a second part of the results about the particles flow in a ring, an energetic stability condition for persistent currents was derived with two analytical methods, one using the Bogoliubov Hamiltonian for small fluctuations and the other only with soliton solutions of GP equation (appendix B). Interestingly, in the full numerical calculation the local minima appears in accordance with the condition derived in meanfield even for a small number of particles. Despite the energy values have an increasing offset with respect to meanfield results for the yrast line as the number of particles decreases, the local minima remain as predicted by meanfield calculations. This investigation reveals that some results from meanfield can still provide relevant information about systems with few particles.

With the characterization of persistent current condition, the time dynamics after quenching a single particle potential in the form of a barrier was investigated. The

stronger interacting cases, which fulfilled the condition to persistently flow, show a smaller depletion of particles from the initial state with unit angular momentum per particle. Besides the average occupation values, the standard deviation was also analyzed to provide more information about the quantum statistical distribution. Remarkably, in some time periods rather large values of standard deviation were observed, which is a very important feature to consider when analyzing experimental measurements, particularly depending on how long the barrier was maintained raised. Despite these results provide a new path to interpret the flow probability introduced in Ref. [118], it may be difficult to separate the quantum and thermal effects in experimental measures, thus, with cooling techniques refinements and traps closer to an ideal ring, these intrinsic quantum effects may be observed more clearly.

In summary, the MCTDHB can provide a deeper understanding of various phenomena and a more accurate description than the meanfield does. Surely, for stationary states, it may not be the ideal method as there are other very relevant alternatives mentioned before, but it still provides a remarkable flexibility related with trap potentials and a straight-forward methodology for computing density distributions. Finally, for time-evolution dynamics, it is the most promising method to the best of our knowledge, only constrained by the numerical resources available.

5.1 Future perspectives

A thorough numerical implementation of the MCTDHB is a very time-consuming task, including reproducing some results and evaluating some consistency tests. Thus, additional efforts should be directed in improving analytical techniques for many-particle systems, at least for specific limits to provide an additional support for the numerical results. The current known tools are deeply connected with the meanfield description yet, as the Thomas-Fermi approximation, soliton solutions of GP equation and Bogoliubov Hamiltonian. This last one is the closest we currently have that works for small fluctuations, however, it is still not suitable for cases with large fragmentation which are commonly studied in MCTDHB. A survey of methods applicable in this case must be examined.

Related to the numerical method, there is already a version ready to handle binary mixtures, although this version was not submitted under enough tests to be applicable in

any specific theme. This generalization for mixtures was possible only after spending some time in two-component BECs in the meanfield level as can be consulted in Ref. [154]. As soon as some results are obtained, the main goal is to study correlations and entanglement involving mixtures, trying to extent quantum information topics to systems of neutral atoms.

Finally, a version that could be applied in two and three dimensions is being developed, again, after working in a simpler problem within GP equation [155]. Nonetheless, the numerical implementation must be carefully designed since the calculations will be very demanding and to study relevant themes we usually need a suitable configurational space and number of IPS that must be feasible.

Appendix A

Matrix elements for the reduced two-body density matrices

We follow Ref. [30], and present the reduced one-body and two-body density matrices explicitly, addapted to our notation. Starting with a β configuration, β_a^b is a resulting configuration index where one particle from the a-th orbital is removed and then added to the b-th orbital. Analogously, starting from a β configuration, β_{ab}^{cd} is a resulting configuration index where, two particles are removed from the a-th and b-th IPS and then added to the c-th and d-th orbital, respectively. Sums over β index ranges from 0 to $N_c(N, M) - 1$.

$$\tilde{\rho}_{kk} = \sum_{\beta} C_{\beta}^* C_{\beta} n_k,$$

$$\tilde{\rho}_{ksks} = \sum_{\beta} C_{\beta}^* C_{\beta} n_k n_s,$$

$$\tilde{\rho}_{kl} = \sum_{\beta} C_{\beta}^* C_{\beta_k^l} \sqrt{(n_l + 1)n_k},$$

$$\tilde{\rho}_{kkqq} = \sum_{\beta} C_{\beta}^* C_{\beta_{kk}^{qq}}$$

$$\tilde{\rho}_{kkkk} = \sum_{\beta} C_{\beta}^* C_{\beta}(n_k^2 - n_k),$$

$$\tilde{\rho}_{kkql} = \sum_{\beta} C_{\beta}^* C_{\beta_{kk}^{ql}} \sqrt{(n_k - 1)n_k(n_q + 1)(n_l + 1)},$$

$$\tilde{\rho}_{kkkl} = \sum_{\beta} C_{\beta}^* C_{\beta_k^l}(n_k - 1)\sqrt{n_k(n_l + 1)},$$

$$\tilde{\rho}_{ksqq} = \sum_{\beta} C_{\beta}^* C_{\beta_{ks}^{qq}} \sqrt{n_k n_s(n_q + 1)(n_q + 2)},$$

$$\tilde{\rho}_{ksss} = \sum_{\beta} C_{\beta}^* C_{\beta_k^s} n_s \sqrt{n_k(n_s + 1)},$$

$$\tilde{\rho}_{kssl} = \sum_{\beta} C_{\beta}^* C_{\beta_k^l} n_s \sqrt{n_k(n_l + 1)},$$

$$\tilde{\rho}_{ksql} = \sum_{\beta} C_{\beta}^* C_{\beta_{ks}^{ql}} \sqrt{n_k n_s(n_q + 1)(n_l + 1)}.$$

Appendix B

Meanfield yrast line

The standard GP time dependent GP equation for the single particle macroscopically occupied state is

$$i\hbar\frac{\partial\psi}{\partial t} = -\frac{\hbar^2}{2M}\frac{\partial^2\psi}{\partial x^2} + (N-1)g_{1\text{D}}|\psi(x,t)|^2\psi(x,t), \tag{B.1}$$

where $g_{1\text{D}}$ is the effective contact interaction strength from $V(x,x') = g_{1\text{D}}\delta(x-x')$, and here we impose the conditions for a ring with length $L = 2\pi R$,

$$x \in \left[-\frac{L}{2}, \frac{L}{2}\right]; \ \psi(-L/2, t) = \psi(L/2, t); \quad \text{and} \quad \int_{-L/2}^{L/2} \mathrm{d}x |\psi(x,t)|^2 = 1. \tag{B.2}$$

The corresponding energy per particle functional is then given by

$$E = \int_{-L/2}^{L/2} \mathrm{d}x \left[\frac{\hbar^2}{2M}\left|\frac{\partial\psi}{\partial x}\right|^2 + (N-1)\frac{g_{1\text{D}}}{2}|\psi(x,t)|^4\right]. \tag{B.3}$$

To construct the Yrast line, the angular momentum of the system must be fixed in the stationary form of Eq. (B.1) obtained from $\psi(x,t) = \psi(x)e^{-i\mu t}$, which in the case of mean-field approach, this is only possible in terms of angular momentum average. For that, we must introduce the Lagrange multiplier Ω with the term $-\Omega l_z = i\hbar\Omega R\partial/\partial x$ in the right side of Eq. (B.1). An important property to note is the equivalence to impose a rotation in the system, and this derivation presented here provide the results used in section 4.2, for instance, to plot the soliton branches in Fig. 4.4 for the energy with respect to the Lagrange multiplier and the respective phases in Fig. 4.5.

A natural choice to obtain Eq. (B.1) in dimensionless units is defining the time scale

based on the frequency ω, such that $ML^2\omega = \hbar$. Thus, with position in units of L and energy in units of $\hbar\omega$ we have

$$\mu\psi(x) = -\frac{1}{2}\frac{\partial^2\psi}{\partial x^2} + iv\frac{\partial\psi}{\partial x} + \alpha|\psi(x)|^2\psi(x), \tag{B.4}$$

with $\alpha \equiv (ML/\hbar^2)(N-1)g_{1D}$ and $v = \Omega/(2\pi\omega)$. Applying the Madelung transformation in the field $\psi(x)$, with $\psi(x) = \sqrt{\rho(x)}e^{i\Phi(x)}$, one may arrive in the equations after separating the real and imaginary parts

$$0 = \left[\Phi'(x) - v\right]\left(\sqrt{\rho(x)}\right)' + \frac{1}{2}\sqrt{\rho(x)}\Phi''(x), \tag{B.5}$$

$$0 = \sqrt{\rho(x)}[\mu + v\Phi'(x)] + \frac{1}{2}\left(\sqrt{\rho(x)}\right)'' - \frac{1}{2}[\Phi'(x)]^2\sqrt{\rho(x)} - \alpha\left(\sqrt{\rho(x)}\right)^3, \tag{B.6}$$

where primes were used to simplify the derivatives with respect to x.

Eq. (B.5) can be integrated once after multiplied by $\sqrt{\rho(x)}$, as result

$$\Phi'(x) = v + \frac{A}{\rho(x)}, \tag{B.7}$$

with A being the integration constant. Substituting Eq. (B.7) above in Eq. (B.6) yield

$$0 = \left(\mu + \frac{v^2}{2}\right)\sqrt{\rho(x)} + \frac{1}{2}\left(\sqrt{\rho(x)}\right)'' - \frac{A^2}{2\rho(x)^2}\sqrt{\rho(x)} - \alpha\left(\sqrt{\rho(x)}\right)^3. \tag{B.8}$$

With the temporary substitution $f = \sqrt{\rho}$ in the equation and also multiplying it by $f'(x)$ produce

$$0 = (2\mu + v^2)\left[f(x)^2\right]' + \left[f'(x)^2\right]' + A^2\left[\frac{1}{f(x)^2}\right]' - \alpha\left[f(x)^4\right]'. \tag{B.9}$$

Thus, after the integration and the back substitution of $f = \sqrt{\rho}$, we obtain

$$\left[\frac{\rho'(x)}{2}\right]^2 = U(\rho) = \alpha\rho(x)^3 - (2\mu + v^2)\rho(x)^2 + B\rho(x) - A^2, \tag{B.10}$$

where B is just another integration constant.

A thorough analysis of Eq. (B.10), show us that the roots of U correspond to critical points of the density ρ, and that $\rho''(x) = dU/d\rho$, therefore, the solution must be constrained in an interval where $U > 0$, bounded by two roots a_1 and a_2, both positives since $\rho \geq 0$. Moreover, α is responsible for U asymptotic behavior, which here we are consid-
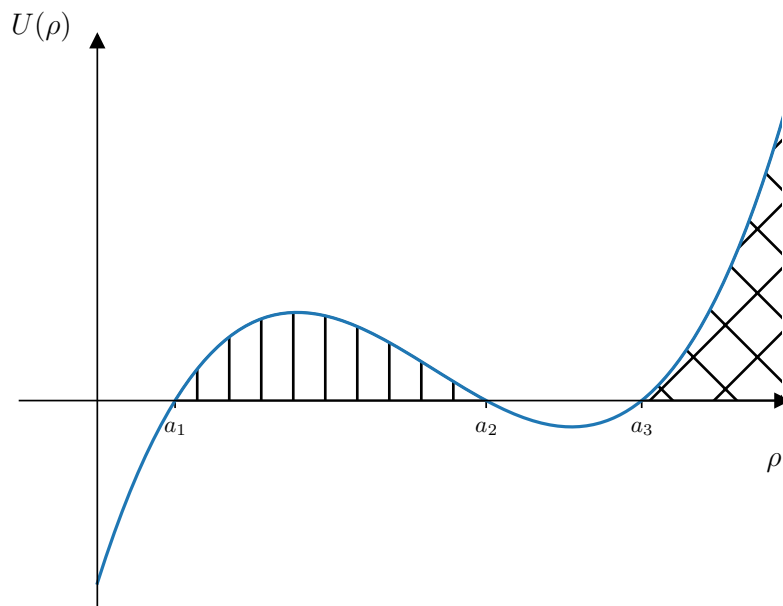
Figure B.1: Illustration of the region for solutions of ρ according to Eq. (B.10). The vertical hatched is the valid region for ρ values, while the crossed hatched region is the forbidden one, since only provide a minimum value by a_3, but no maximum.

ering positive(repulsive interaction). Therefore, we can conclude that all three roots of U must be positive, denoted by $a_1 \leq a_2 \leq a_3$, with $a_1 \leq \rho \leq a_2$ as depicted in Fig. B.1. Notably, if $a_1 = a_2$, the density ρ is constant and we shall recover the plane wave solutions. The equation for the density can then be written as

$$\left[\frac{\rho'(x)}{2}\right]^2 = \alpha(\rho(x) - a_1)(\rho(x) - a_2)(\rho(x) - a_3), \tag{B.11}$$

with the correspondence to previous variables given by

$$\alpha a_1 a_2 a_3 = A^2, \tag{B.12}$$

$$\alpha(a_1 + a_2 + a_3) = 2\mu + v^2, \tag{B.13}$$

$$\alpha(a_1 a_2 + a_1 a_3 + a_2 a_3) = B. \tag{B.14}$$

Eq. (B.11) can now be integrated, assuming that at $x = 0$ we have a minimum for ρ, which implies that $\rho(0) = a_1$, and then

$$2x = \int_{a_1}^{\rho(x)} \frac{\mathrm{d}\zeta}{\sqrt{\alpha(\zeta - a_1)(\zeta - a_2)(\zeta - a_3)}}, \tag{B.15}$$

which yields

$$\rho(x) = a_1 + (a_2 - a_1)\mathrm{sn}^2\Big(x\sqrt{\alpha(a_3 - a_1)}, \kappa\Big), \quad \kappa^2 \equiv \frac{a_2 - a_1}{a_3 - a_1} \in [0, 1], \qquad (B.16)$$

where the Jacobi elliptic function sn corresponds to the inverse of the incomplete elliptic integral of first kind $F(\phi, m)$ as [84]

$$\sin\phi = \mathrm{sn}\Big(F(\phi, m), m\Big), \quad F(\phi, m) = \int_0^\phi \frac{\mathrm{d}\theta}{\sqrt{1 - m^2\sin^2\theta}}. \qquad (B.17)$$

To completely determine the solution, Eq. (B.7) must be integrated, which results in

$$\Phi(x) = vx \pm \sqrt{\frac{a_2 a_3}{a_1(a_3 - a_1)}}\Pi\Big(1 - \frac{a_2}{a_1}\Big|\mathrm{am}(x\sqrt{\alpha(a_3 - a_1)}, \kappa), \kappa\Big),$$

$$\Pi\Big(n\Big|\phi, m\Big) = \int_0^\phi \frac{1}{1 - n\sin^2\theta}\frac{\mathrm{d}\theta}{\sqrt{1 - m^2\sin^2\theta}}, \qquad (B.18)$$

where Π is known as the incomplete elliptic integral of third kind and the function am is known as the Jacobi amplitude and is simply given by $\mathrm{am}(u, m) = \sin^{-1}[\mathrm{sn}(u, m)]$ [84]. The plus/minus sign that appears in Eq. (B.18) arise from Eq. (B.12).

Finally, we must impose the periodic boundary conditions and the unit norm. For the first constraint, we must use that $\mathrm{sn}(\mathrm{u}, \mathrm{m})^2$ is a periodic function with period $2K(m)$, where $K(m) = F(\pi/2, m)$ is the complete elliptic integral of first kind. Within the dimensionless variable $x \in [-1/2, 1/2]$ we must impose

$$2nK(\kappa) = \sqrt{\alpha(a_3 - a_1)}, \quad \forall n \in \mathbb{N}, \qquad (B.19)$$

where n indicate the number of minima ρ will display. Thus for $n > 1$, we have what is known as soliton train solution, due to the multiple peak structure that appears in the density. The phase in Eq. (B.18), albeit of the periodic conditions, it may just fulfill the complex exponential periodicity, what implies that $\Phi(1/2)$ differs from $\Phi(-1/2)$ by an integer multiple of 2π,

$$2w\pi = \Phi(1/2) - \Phi(-1/2) = v \pm 2n\sqrt{\frac{a_2 a_3}{a_1(a_3 - a_1)}}\Pi\Big(1 - \frac{a_2}{a_1}\Big|\frac{\pi}{2}, \kappa\Big); \quad \forall w \in \mathbb{Z}. \qquad (B.20)$$

Next we apply the unit norm condition as $\int dx \rho(x) = 1$ and using Eq. (B.19) we obtain

$$a_3 = 1 + \frac{4n^2}{\alpha} K(\kappa) E(\kappa), \tag{B.21}$$

where $E(\kappa)$ denotes the complete elliptic integral of second kind. Analogously to the form of Eq. (B.21), we can use it in Eq. (B.19) and then in the κ definition to obtain a_1 and a_2 also as function of κ and n as

$$a_1 = 1 - \frac{4n^2}{\alpha} K(\kappa) \Big[K(\kappa) - E(\kappa) \Big] > 0, \tag{B.22}$$

$$a_2 = 1 - \frac{4n^2}{\alpha} K(\kappa) \Big[(1 - \kappa^2) K(\kappa) - E(\kappa) \Big], \tag{B.23}$$

$$a_3 = 1 + \frac{4n^2}{\alpha} K(\kappa) E(\kappa). \tag{B.24}$$

With the set of equations (B.22)-(B.24) and (B.20) we have as free parameters κ , n, w and the sign in (B.20), where once these are fixed, all the others are readily obtained, including the Lagrange multiplier v. Moreover, we note that Eq. (B.22) impose an upper bound to κ value, which depends on the soliton train number and dimensionless interaction strength α. Another remarkable property is when $\kappa = 0$, implying $a_1 = a_2 = 1$ and $a_3 = 1 + n^2 \pi^2 / \alpha$. Consequently, one straightforwardly obtain

$$\text{If } \kappa = 0 \implies v_\pm = 2w\pi \mp \sqrt{\alpha + n^2 \pi^2}, \quad \Phi(x) = (2w\pi)x, \quad \rho(x) = 1, \tag{B.25}$$

which characterize just an momentum eigenstate given by a plane wave.

The angular momentum and energy per particle are key quantities to study the yrast line, though the integrals are rather cumbersome. The angular momentum per particle as well as its plane wave limit are given by

$$\frac{L_M}{N\hbar} = \frac{1}{2\pi} \int_{-1/2}^{1/2} \rho(x) \Phi'(x) = \frac{1}{2\pi} \Big[v_\pm \pm \sqrt{\alpha a_1 a_2 a_3} \Big] \xrightarrow[k=0]{} w. \tag{B.26}$$

while from Eq. (B.3), the energy can be written as

$$\left(\frac{ML^2}{\hbar^2} \right) E = \mu + v_\pm \int_{-1/2}^{1/2} \rho(x) \Phi'(x) - \frac{\alpha}{2} \int_{-1/2}^{1/2} \rho(x)^2 \xrightarrow[k=0]{} \frac{1}{2}(2w\pi)^2 + \frac{\alpha}{2}, \tag{B.27}$$

The energy can also be integrated analytically for an arbitrary value of κ, though the
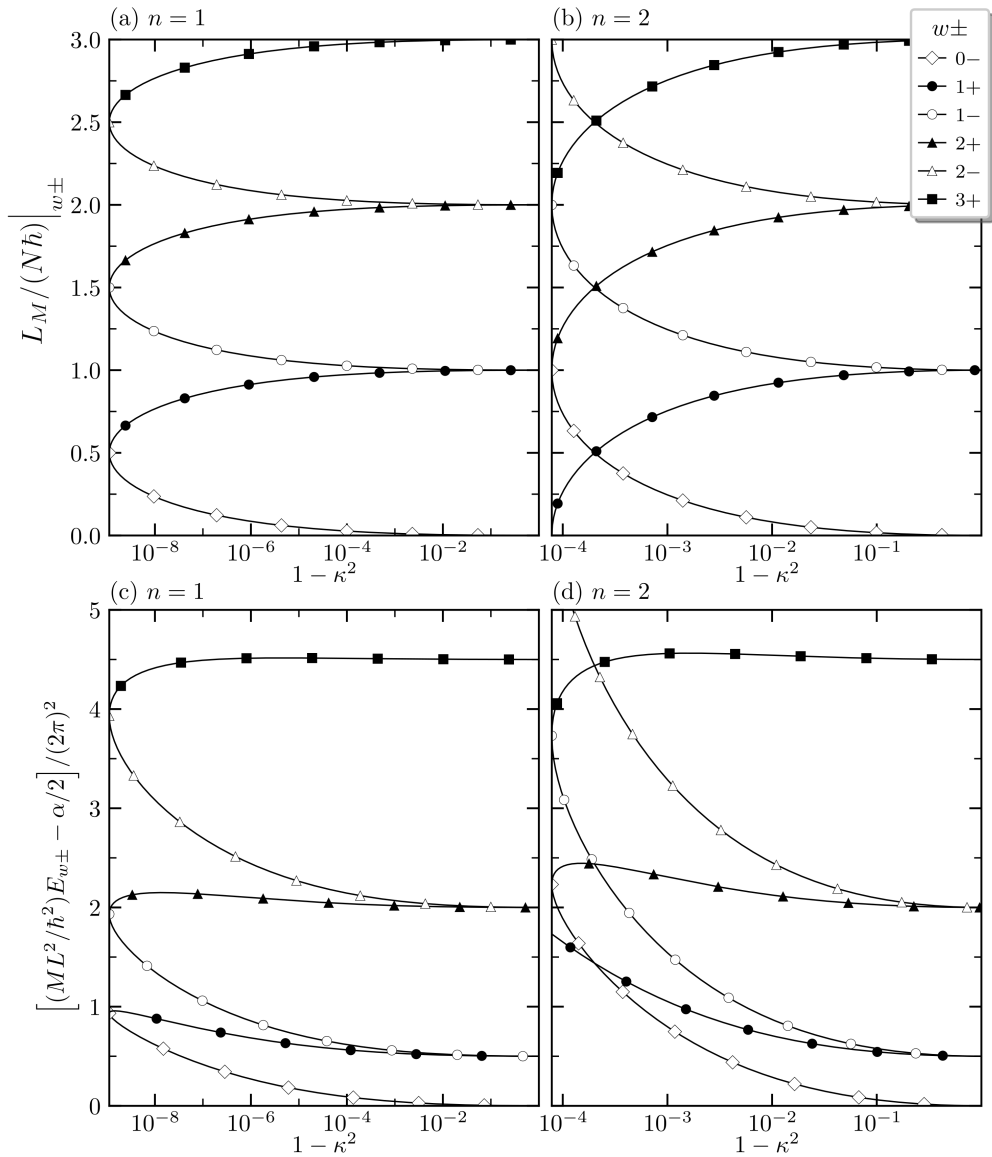
Figure B.2: Angular momentum and energy per particle as function of the elliptic parameter κ for various winding numbers w and sign choice for the phase in Eq. (B.18). The first column, frames (a) and (c), correspond to the case of a simple soliton($n = 1$), and frames (b) and (d) to a double soliton($n = 2$). All frames have in common the dimensionless interaction parameter $\alpha = 500$.

final formula is intricate and thus omitted here. Note, however, that the second integral is just proportional to the angular momentum, a fact that will be used in the persistent current stability condition below.

In Fig. B.2, the angular momentum and energy are shown as continuous function of the elliptic parameter, in terms of $1 - \kappa^2$, in which case ease the visualization in log scale since κ can be very close to 1. The energy is subtracted from the interacting part of the plane wave solution, that is $\alpha/2$, and divided by $(2\pi)^2$ to better display the result as
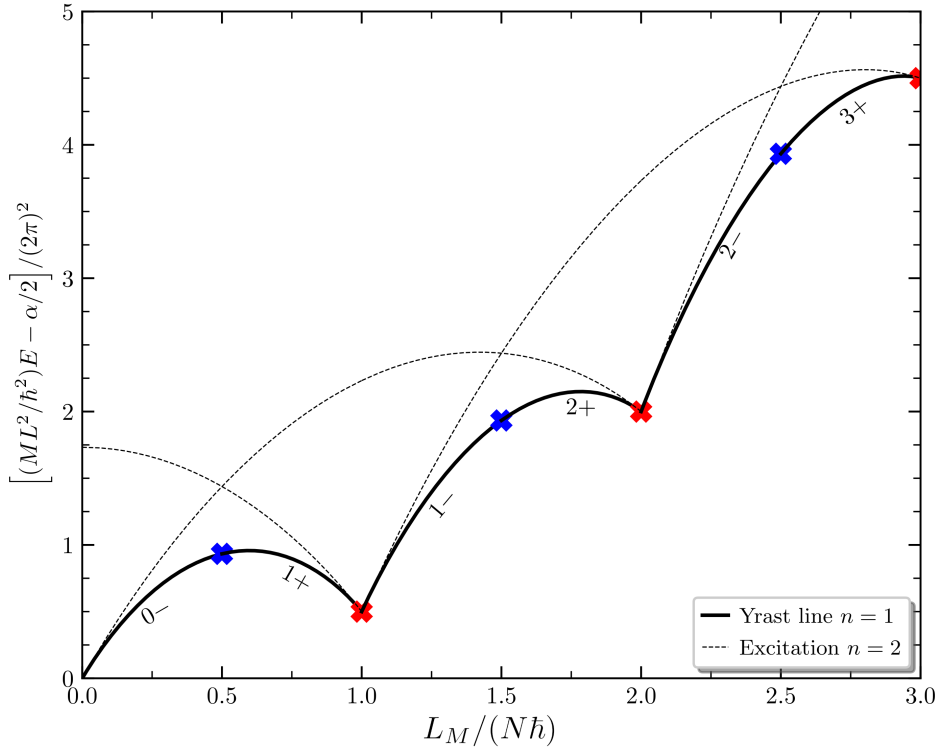
Figure B.3: Two energy branches of soliton solutions with $n = 1$ and $n = 2$. The Yrast line is the lowest energy state as function of angular momentum, corresponding to $n = 1$, whereas the crosses indicate the winding number and sign transition. The dimensionless interaction parameter is the same of Fig. B.2, $\alpha = 500$

$k \to 0$ according to Eq. (B.27), whereas we must obtain $w^2/2$ in this limit.

Finally, to properly define the yrast line within the meanfield approach, we must define a parametric curve using κ to plot the energy as function of momentum, connecting the line segments for each w, which results in Fig. B.3. As can be noted, the soliton trains, i.e $n > 1$, are excitations and therefore the Yrast line corresponds to $n = 1$.

The persistent current criterion is established based on the cusp presented in the transition between different signs for a fixed w, as illustrated in Fig. B.3, where there must be a sign inversion in the derivative of the energy with respect to the angular momentum. Therefore, with $\epsilon = (ML^2/\hbar^2)E$ the dimensionless energy and $l = L_M/(N\hbar)$ the dimensionless angular momentum per particle we have

$$\left(\lim_{l \to w^+} \frac{\partial \epsilon}{\partial l} \right) \left(\lim_{l \to w^-} \frac{\partial \epsilon}{\partial l} \right) < 0. \tag{B.28}$$

Since $\partial \epsilon / \partial l = 2\pi v_{\pm}$, we can use the limit $k \to 0$ that conducts to the plane waves in

Eq. (B.25) to obtain

$$\left[2\pi w + \sqrt{\alpha + \pi^2}\right]\left[2\pi w - \sqrt{\alpha + \pi^2}\right] < 0, \tag{B.29}$$

$$\frac{\alpha}{4\pi^2} > w^2 - \frac{1}{4}. \tag{B.30}$$

The result with respect to the system's bare parameters becomes $(R = L/(2\pi))$

$$\frac{(N-1)g_{1D}}{2\pi}\left(\frac{MR}{\hbar^2}\right) > w^2 - \frac{1}{4}, \tag{B.31}$$

which is almost the same result of Eq. (4.46) apart from parameters labels and the factor $(N-1)$. This discrepancy in the number of particles appearing in the formulas is natural, since in the Bogoliubov development, at some stages, we had to consider $N - O(1) \equiv N$. In this case, with $N \gg 1$ the formulas become identical.

As a final remark, among some important features to comment in this meanfield workout of yrast line, at least one deserve some attention. The yrast line built here considered the average angular momentum, thus, the states have broken translational symmetry. The GP equation is only capable to produce eigenstates of angular momentum in integer multiples of the number of particles, since all occupies the same state. In a many-body calculation, this line is actually composed by discrete points.

Bibliography

[1] A. J. Leggett. On the superfluid fraction of an arbitrary many-body system at T=0. J. Stat. Phys., **vol. 93**(3); pp. 927–941 (1998). doi:10.1023/B:JOSS.0000033170.38619.6c.

[2] K. Huang. *Statistical Mechanics*. John Wiley & Sons, New York (1987). ISBN 0-471-81518-7.

[3] R. K. Pathria and P. D. Beale. *Statistical Mechanics*. Elsevier, Oxford, 3rd edn. (2011). ISBN 978-0-12-382188-1.

[4] E. H. Lieb and W. Liniger. Exact analysis of an interacting bose gas. i. the general solution and the ground state. Phys. Rev., **vol. 130**; pp. 1605–1616 (1963). doi:10.1103/PhysRev.130.1605.

[5] E. H. Lieb. Exact analysis of an interacting bose gas. ii. the excitation spectrum. Phys. Rev., **vol. 130**; pp. 1616–1624 (1963). doi:10.1103/PhysRev.130.1616.

[6] G. Lang, F. Hekking, and A. Minguzzi. Ground-state energy and excitation spectrum of the lieb-liniger model : accurate analytical results and conjectures about the exact solution. SciPost Phys., **vol. 3**; p. 003 (2017). doi:10.21468/SciPostPhys.3.1.003.

[7] K. Sakmann, A. I. Streltsov, O. E. Alon, and L. S. Cederbaum. Exact ground state of finite bose-einstein condensates on a ring. Phys. Rev. A, **vol. 72**; p. 033613 (2005). doi:10.1103/PhysRevA.72.033613.

[8] J. Sato, R. Kanamoto, E. Kaminishi, and T. Deguchi. Quantum states of dark solitons in the 1d bose gas. New Journal of Physics, **vol. 18**(7); p. 075008 (2016). doi:10.1088/1367-2630/18/7/075008.

[9] M. Girardeau. Relationship between systems of impenetrable bosons and fermions in one dimension. Journal of Mathematical Physics, **vol. 1**(6); pp. 516–523 (1960). doi:10.1063/1.1703687.

[10] V. I. Yukalov and M. D. Girardeau. Fermi-bose mapping for one-dimensional bose gases. Laser Physics Letters, **vol. 2**(8); pp. 375–382 (2005). doi:10.1002/lapl.200510011.

[11] M. Cominotti, D. Rossini, M. Rizzi, F. Hekking, and A. Minguzzi. Optimal persistent currents for interacting bosons on a ring with a gauge field. Phys. Rev. Lett., **vol. 113**; p. 025301 (2014). doi:10.1103/PhysRevLett.113.025301.

[12] P. W. Anderson. More is different. Science, **vol. 177**(4047); pp. 393–396 (1972). doi:10.1126/science.177.4047.393.

[13] C. Monroe, W. Swann, H. Robinson, and C. Wieman. Very cold trapped atoms in a vapor cell. Phys. Rev. Lett., **vol. 65**; pp. 1571–1574 (1990). doi:10.1103/PhysRevLett.65.1571.

[14] S. Chu. Nobel lecture: The manipulation of neutral particles. Rev. Mod. Phys., **vol. 70**; pp. 685–706 (1998). doi:10.1103/RevModPhys.70.685.

[15] C. N. Cohen-Tannoudji. Nobel lecture: Manipulating atoms with photons. Rev. Mod. Phys., **vol. 70**; pp. 707–719 (1998). doi:10.1103/RevModPhys.70.707.

[16] W. D. Phillips. Nobel lecture: Laser cooling and trapping of neutral atoms. Rev. Mod. Phys., **vol. 70**; pp. 721–741 (1998). doi:10.1103/RevModPhys.70.721.

[17] S. N. Bose. Plancks gesetz und lichtquantenhypothese. Zeitschrift für Physik, **vol. 26**; pp. 178–181 (1924). doi:10.1103/PhysRevA.88.063627.

[18] A. Einstein. Quantentheorie des einatomigen idealen gases. Sitz. Ber. Preuss. Akad. Wiss., **vol. 22**; pp. 261–267 (1924).

[19] M. H. Anderson, J. R. Ensher, M. R. Matthews, C. E. Wieman, and E. A. Cornell. Observation of Bose-Einstein condensation in a dilute atomic vapor. Science, **vol. 269**(5221); pp. 198–201 (1995). doi:10.1126/science.269.5221.198.

[20] C. J. Pethick and H. Smith. *Bose-Einstein Condensation in Dilute Gases*. Cambridge University Press, Cambridge, 2nd edn. (2008).

[21] L. Pitaevskii and S. Stringari. *Bose-Einstein Condensation and Superfluidity*. Oxford University Press, United Kingdom, 2nd edn. (2016).

[22] W. Ketterle. Nobel lecture: When atoms behave as waves: Bose-einstein condensation and the atom laser. Rev. Mod. Phys., **vol. 74**; pp. 1131–1151 (2002). doi:10.1103/RevModPhys.74.1131.

[23] C. W. Gardiner and P. Zoller. *Quantum Noise*. Springer-Verlag, Heidelberg (2000). ISBN 3-540-66571-4.

[24] H.-P. Breuer and P. Francesco. *The Theory of Open Quantum Systems*. Oxford University Press, New York (2002).

[25] R. Kosloff. Time-dependent quantum-mechanical methods for molecular dynamics. The Journal of Physical Chemistry, **vol. 92**(8); pp. 2087–2100 (1988). doi:10.1021/j100319a003.

[26] Z. Kotler, A. Nitzan, and R. Kosloff. Multiconfiguration time-dependent self-consistent field approximation for curve crossing in presence of a bath. a fast fourier transform study. Chemical Physics Letters, **vol. 153**(6); pp. 483 – 489 (1988). doi:https://doi.org/10.1016/0009-2614(88)85247-3.

[27] H.-D. Meyer, U. Manthe, and L. Cederbaum. The multi-configurational time-dependent Hartree approach. Chemical Physics Letters, **vol. 165**(1); pp. 73 – 78 (1990). doi:https://doi.org/10.1016/0009-2614(90)87014-I.

[28] J. R. Waldeck, J. Campos-Martínez, and R. D. Coalson. Application of a coupled-surface time-dependent Hartree grid method to excited state optical spectroscopy. The Journal of Chemical Physics, **vol. 94**(4); pp. 2773–2780 (1991). doi:10.1063/1.459854.

[29] U. Manthe, H. Meyer, and L. S. Cederbaum. Wave-packet dynamics within the multiconfiguration Hartree framework: General aspects and application to nocl. The Journal of Chemical Physics, **vol. 97**(5); pp. 3199–3213 (1992). doi:10.1063/1.463007.

[30] O. E. Alon, A. I. Streltsov, and L. S. Cederbaum. Multiconfigurational time-dependent Hartree method for bosons: Many-body dynamics of bosonic systems. Phys. Rev. A, **vol. 77**; p. 033613 (2008). doi:10.1103/PhysRevA.77.033613.

[31] E. Fasshauer and A. U. J. Lode. Multiconfigurational time-dependent Hartree method for fermions: Implementation, exactness, and few-fermion tunneling to open space. Phys. Rev. A, **vol. 93**; p. 033635 (2016). doi:10.1103/PhysRevA.93.033635.

[32] A. U. J. Lode, K. Sakmann, O. E. Alon, L. S. Cederbaum, and A. I. Streltsov. Numerically exact quantum dynamics of bosons with time-dependent interactions of harmonic type. Phys. Rev. A, **vol. 86**; p. 063606 (2012). doi:10.1103/PhysRevA.86.063606.

[33] S. Klaiman and L. S. Cederbaum. Overlap of exact and gross-pitaevskii wave functions in Bose-Einstein condensates of dilute gases. Phys. Rev. A, **vol. 94**; p. 063648 (2016). doi:10.1103/PhysRevA.94.063648.

[34] R. Roy, A. Gammal, M. C. Tsatsos, B. Chatterjee, B. Chakrabarti, and A. U. J. Lode. Phases, many-body entropy measures, and coherence of interacting bosons in optical lattices. Phys. Rev. A, **vol. 97**; p. 043625 (2018). doi:10.1103/PhysRevA.97.043625.

[35] S. I. Mistakidis, L. Cao, and P. Schmelcher. Interaction quench induced multimode dynamics of finite atomic ensembles. Journal of Physics B: Atomic, Molecular and Optical Physics, **vol. 47**(22); p. 225303 (2014). doi:10.1088/0953-4075/47/22/225303.

[36] A. U. J. Lode, B. Chakrabarti, and V. K. B. Kota. Many-body entropies, correlations, and emergence of statistical relaxation in interaction quench dynamics of ultracold bosons. Phys. Rev. A, **vol. 92**; p. 033622 (2015). doi:10.1103/PhysRevA.92.033622.

[37] S. I. Mistakidis, L. Cao, and P. Schmelcher. Negative-quench-induced excitation dynamics for ultracold bosons in one-dimensional lattices. Phys. Rev. A, **vol. 91**; p. 033611 (2015). doi:10.1103/PhysRevA.91.033611.

[38] S. I. Mistakidis and P. Schmelcher. Mode coupling of interaction quenched ultracold few-boson ensembles in periodically driven lattices. Phys. Rev. A, **vol. 95**; p. 013625 (2017). doi:10.1103/PhysRevA.95.013625.

[39] J. Neuhaus-Steinmetz, S. I. Mistakidis, and P. Schmelcher. Quantum dynamical response of ultracold few-boson ensembles in finite optical lattices to multiple interaction quenches. Phys. Rev. A, **vol. 95**; p. 053610 (2017). doi:10.1103/PhysRevA.95.053610.

[40] G. M. Koutentakis, S. I. Mistakidis, and P. Schmelcher. Quench-induced resonant tunneling mechanisms of bosons in an optical lattice with harmonic confinement. Phys. Rev. A, **vol. 95**; p. 013617 (2017). doi:10.1103/PhysRevA.95.013617.

[41] S. Mistakidis, G. Koutentakis, and P. Schmelcher. Bosonic quantum dynamics following a linear interaction quench in finite optical lattices of unit filling. Chemical Physics, **vol. 509**; pp. 106 – 115 (2018). doi:https://doi.org/10.1016/j.chemphys.2017.11.022.

[42] T. Plaßmann, S. I. Mistakidis, and P. Schmelcher. Quench dynamics of finite bosonic ensembles in optical lattices with spatially modulated interactions. Journal of Physics B: Atomic, Molecular and Optical Physics, **vol. 51**(22); p. 225001 (2018). doi:10.1088/1361-6455/aae57a.

[43] E. Fasshauer and A. U. J. Lode. Multiconfigurational time-dependent Hartree method for fermions: Implementation, exactness, and few-fermion tunneling to open space. Phys. Rev. A, **vol. 93**; p. 033635 (2016). doi:10.1103/PhysRevA.93.033635.

[44] J. Erdmann, S. I. Mistakidis, and P. Schmelcher. Correlated tunneling dynamics of an ultracold fermi-fermi mixture confined in a double well. Phys. Rev. A, **vol. 98**; p. 053614 (2018). doi:10.1103/PhysRevA.98.053614.

[45] L. Cao, S. I. Mistakidis, X. Deng, and P. Schmelcher. Collective excitations of dipolar gases based on local tunneling in superlattices. Chemical Physics, **vol. 482**; pp. 303 – 310 (2017). doi:https://doi.org/10.1016/j.chemphys.2016.08.026.

[46] G. M. Koutentakis, S. I. Mistakidis, and P. Schmelcher. Probing ferromagnetic order in few-fermion correlated spin-flip dynamics. New Journal of Physics, **vol. 21**(5); p. 053005 (2019). doi:10.1088/1367-2630/ab14ba.

[47] S. I. Mistakidis, G. C. Katsimiga, G. M. Koutentakis, and P. Schmelcher. Repulsive fermi polarons and their induced interactions in binary mixtures of ultracold atoms. New Journal of Physics, **vol. 21**(4); p. 043032 (2019). doi:10.1088/1367-2630/ab1045.

[48] A. U. J. Lode and C. Bruder. Fragmented superradiance of a bose-einstein condensate in an optical cavity. Phys. Rev. Lett., **vol. 118**; p. 013603 (2017). doi:10.1103/PhysRevLett.118.013603.

[49] J. H. V. Nguyen, M. C. Tsatsos, D. Luo, A. U. J. Lode, G. D. Telles, V. S. Bagnato, and R. G. Hulet. Parametric excitation of a Bose-Einstein condensate: From Faraday waves to granulation. Phys. Rev. X, **vol. 9**; p. 011052 (2019). doi:10.1103/PhysRevX.9.011052.

[50] S. Klaiman, A. U. J. Lode, A. I. Streltsov, L. S. Cederbaum, and O. E. Alon. Breaking the resilience of a two-dimensional bose-einstein condensate to fragmentation. Phys. Rev. A, **vol. 90**; p. 043620 (2014). doi:10.1103/PhysRevA.90.043620.

[51] I. Březinová, A. U. J. Lode, A. I. Streltsov, O. E. Alon, L. S. Cederbaum, and J. Burgdörfer. Wave chaos as signature for depletion of a bose-einstein condensate. Phys. Rev. A, **vol. 86**; p. 013630 (2012). doi:10.1103/PhysRevA.86.013630.

[52] U. R. Fischer, A. U. J. Lode, and B. Chatterjee. Condensate fragmentation as a sensitive measure of the quantum many-body behavior of bosons with long-range interactions. Phys. Rev. A, **vol. 91**; p. 063621 (2015). doi:10.1103/PhysRevA.91.063621.

[53] A. Weiße and H. Fehske. Exact diagonalization techniques. In H. Fehske, R. Schneider, and A. Weiße, editors, *Computational Many-Particle Physics*, pp. 529–544. Springer Berlin Heidelberg, Berlin, Heidelberg (2008). ISBN 978-3-540-74686-7. doi:10.1007/978-3-540-74686-7_18.

[54] D. Raventós, T. Graß, M. Lewenstein, and B. Juliá-Díaz. Cold bosons in optical lattices: a tutorial for exact diagonalization. Journal of Physics B: Atomic, Molecular and Optical Physics, **vol. 50**(11); p. 113001 (2017). doi:10.1088/1361-6455/aa68b1.

[55] O. Penrose and L. Onsager. Bose-Einstein condensation and liquid helium. Phys. Rev., **vol. 104**; pp. 576–584 (1956). doi:10.1103/PhysRev.104.576.

[56] E. H. Lieb, R. Seiringer, and J. Yngvason. Bosons in a trap: A rigorous derivation of the Gross-Pitaevskii energy functional. Phys. Rev. A, **vol. 61**; p. 043602 (2000). doi:10.1103/PhysRevA.61.043602.

[57] E. H. Lieb and R. Seiringer. Proof of Bose-Einstein condensation for dilute trapped gases. Phys. Rev. Lett., **vol. 88**; p. 170409 (2002). doi:10.1103/PhysRevLett.88.170409.

[58] E. K. U. Gross, E. Runge, and O. Heinonen. *Many-particle theory*. Adam Hilger, England (1991). ISBN 0-7503-0155-4. English Edition.

[59] J. Javanainen and S. M. Yoo. Quantum phase of a bose-einstein condensate with an arbitrary number of atoms. Phys. Rev. Lett., **vol. 76**; pp. 161–164 (1996). doi:10.1103/PhysRevLett.76.161.

[60] M. Naraschewski and R. J. Glauber. Spatial coherence and density correlations of trapped Bose gases. Phys. Rev. A, **vol. 59**; pp. 4595–4607 (1999). doi:10.1103/PhysRevA.59.4595.

[61] K. Sakmann, A. I. Streltsov, O. E. Alon, and L. S. Cederbaum. Reduced density matrices and coherence of trapped interacting bosons. Phys. Rev. A, **vol. 78**; p. 023615 (2008). doi:10.1103/PhysRevA.78.023615.

[62] A. J. Leggett. Superfluidity. Rev. Mod. Phys., **vol. 71**; pp. S318–S323 (1999). doi:10.1103/RevModPhys.71.S318.

[63] N. R. Cooper and Z. Hadzibabic. Measuring the superfluid fraction of an ultracold atomic gas. Phys. Rev. Lett., **vol. 104**; p. 030401 (2010). doi:10.1103/PhysRevLett.104.030401.

[64] A. V. Andriati and A. Gammal. Superfluid fraction of few bosons in an annular geometry in the presence of a rotating weak link. Phys. Rev. A, **vol. 100**; p. 063625 (2019). doi:10.1103/PhysRevA.100.063625.

[65] A. Andriati and A. Gammal. Hashing algorithms, optimized mappings and massive parallelization of multiconfigurational methods for bosons (2020). `https://arxiv.org/abs/2005.13679`.

[66] E. Merzbacher. *Quantum mechanics*. John Wiley & Sons, New York, 3rd edn. (1998).

[67] G. Baym. *Lectures on quantum mechanics*. CRC Press, Boca Raton (1974).

[68] A. F. R. de Toledo Piza. *Mecânica Quântica*. Edusp, São Paulo (2009). ISBN 978-85-314-0748-2.

[69] E. J. Mueller, T.-L. Ho, M. Ueda, and G. Baym. Fragmentation of bose-einstein condensates. Phys. Rev. A, **vol. 74**; p. 033612 (2006). doi:10.1103/PhysRevA.74.033612.

[70] E. Nicolau, J. Mompart, B. Juliá-Díaz, and V. Ahufinger. Orbital angular momentum dynamics of bose-einstein condensates trapped in two stacked rings. Phys. Rev. A, **vol. 102**; p. 023331 (2020). doi:10.1103/PhysRevA.102.023331.

[71] A. Oliinyk, A. Yakimenko, and B. Malomed. Tunneling of persistent currents in coupled ring-shaped bose–einstein condensates. Journal of Physics B: Atomic, Molecular and Optical Physics, **vol. 52**(22); p. 225301 (2019). doi:10.1088/1361-6455/ab46f9.

[72] S. Tan. Three-boson problem at low energy and implications for dilute bose-einstein condensates. Phys. Rev. A, **vol. 78**; p. 013636 (2008). doi:10.1103/PhysRevA.78.013636.

[73] T. T. Wu. Ground state of a bose system of hard spheres. Phys. Rev., **vol. 115**; pp. 1390–1404 (1959). doi:10.1103/PhysRev.115.1390.

[74] A. J. Leggett. Bose-einstein condensation in the alkali gases: Some fundamental concepts. Rev. Mod. Phys., **vol. 73**; pp. 307–356 (2001). doi:10.1103/RevModPhys.73.307.

[75] A. J. Leggett and F. Sols. On the concept of spontaneously broken gauge symmetry in condensed matter physics. Foundations of Physics, **vol. 21**; pp. 353–364 (1991). doi:10.1007/BF01883640.

[76] S. Hassani. *Calculus of Variations, Symmetries, and Conservation Laws*, pp. 1047–1075. Springer International Publishing, Cham (2013). ISBN 978-3-319-01195-0. doi:10.1007/978-3-319-01195-0_33.

[77] S. Liang. A perfect hashing function for exact diagonalization of many-body systems of identical particles. Comput. Phys. Commun., **vol. 92**(1); pp. 11 – 15 (1995). doi:https://doi.org/10.1016/0010-4655(95)00108-R.

[78] A. I. Streltsov, O. E. Alon, and L. S. Cederbaum. General mapping for bosonic and fermionic operators in fock space. Phys. Rev. A, **vol. 81**; p. 022124 (2010). doi:10.1103/PhysRevA.81.022124.

[79] J. M. Zhang and R. X. Dong. Exact diagonalization: the Bose–Hubbard model as an example. European Journal of Physics, **vol. 31**(3); pp. 591–602 (2010). doi:10.1088/0143-0807/31/3/016.

[80] H. Q. Lin. Exact diagonalization of quantum-spin models. Phys. Rev. B, **vol. 42**; pp. 6561–6567 (1990). doi:10.1103/PhysRevB.42.6561.

[81] A. W. Sandvik. Computational studies of quantum spin systems. AIP Conference Proceedings, **vol. 1297**(1); pp. 135–338 (2010). doi:10.1063/1.3518900.

[82] C. Jia, Y. Wang, C. Mendl, B. Moritz, and T. Devereaux. Paradeisos: A perfect hashing algorithm for many-body eigenvalue problems. Comput. Phys. Commun., **vol. 224**; pp. 81 – 89 (2018). doi:https://doi.org/10.1016/j.cpc.2017.11.011.

[83] R. Sedgewick and K. Wayne. *Algorithms*. Addison-Wesley, Boston (2011). ISBN 978-3-642-22865-0.

[84] I. S. Gradshteyn and I. M. Ryzhik. *Table of integrals, series, and products*. Academic Press, New York, 7th edn. (2007).

[85] C. Lanczos. An iteration method for the solution of the eigenvalue problem of linear differential and integral operators. J. Res. Natl. Bur. Stand. B, **vol. 45**; pp. 255–282 (1950). doi:10.6028/jres.045.026.

[86] C. F. V. Loan and G. H. Golub. *Matrix Computations*. The Johns Hopkins University Press, London (1996).

[87] J. W. Demmel. *7. Iterative Methods for Eigenvalue Problems*, chap. 7, pp. 361–387. siam (1996). doi:10.1137/1.9781611971446.ch7.

[88] Linear algebra package. `http://www.netlib.org/lapack/`. Accessed: 2019-02-12.

[89] C. C. Paige. Practical use of the symmetric lanczos process with reorthogonalization. BIT Numerical Mathematics, **vol. 10**(2); pp. 183–195 (1970). doi:10.1007/BF01936866.

[90] H. D. Simon. Analysis of the symmetric lanczos algorithm with reorthogonalization methods. Linear Algebra and its Applications, **vol. 61**; pp. 101 – 131 (1984). doi:https://doi.org/10.1016/0024-3795(84)90025-9.

[91] M. Beck, A. Jäckle, G. Worth, and H.-D. Meyer. The multiconfiguration time-dependent Hartree (MCTDH) method: a highly efficient algorithm for propagating wavepackets. Physics Reports, **vol. 324**(1); pp. 1 – 105 (2000). doi:https://doi.org/10.1016/S0370-1573(99)00047-2.

[92] H.-D. Meyer, F. Gatti, and G. A. Worth. *Multidimensional Quantum Dynamics - MCTDH Theory and applications*. WILEY-VCH, Weinheim (2009).

[93] M. Beck and H.-D. Meyer. An efficient and robust integration scheme for the equations of motion of the multiconfiguration time-dependent Hartree (mctdh) method. Zeitschrift für Physik D Atoms, Molecules and Clusters, **vol. 42**; pp. 113–129 (1997). doi:10.1007/s004600050342.

[94] W. H. Press, S. A. Teukolsky, W. T. Vetterling, and B. P. Flannery. *Numerical Recipes in C - The Art of Scientific Computing*. Cambridge University Press, Cambridge (1992).

[95] T. J. Park and J. C. Light. Unitary quantum time evolution by iterative lanczos reduction. The Journal of Chemical Physics, **vol. 85**(10); pp. 5870–5876 (1986). doi:10.1063/1.451548.

[96] P. L. DeVries. *A First Course in Computational Physics*. John Wiley & Sons, Ohio (1994).

[97] J. Crank and P. Nicolson. A practical method for numerical evaluation of solutions of partial differential equations of the heat-conduction type. Mathematical Proceedings of the Cambridge Philosophical Society, **vol. 43**(1); p. 50–67 (1947). doi:10.1017/S0305004100023197.

[98] K. W. Morton and D. Mayers. *Numerical Solution of Partial Differential Equations*. Cambridge University Press, United Kingdom (2005).

[99] D. Quinney. *An Introduction to the Numerical Solution of Differential Equations*. Research Studies Press LTD, England (1987). Revised Edition.

[100] J. C. Light, I. P. Hamilton, and J. V. Lill. Generalized discrete variable approximation in quantum mechanics. The Journal of Chemical Physics, **vol. 82**(3); pp. 1400–1409 (1985). doi:10.1063/1.448462.

[101] V. Szalay. Discrete variable representations of differential operators. The Journal of Chemical Physics, **vol. 99**(3); pp. 1978–1984 (1993). doi:10.1063/1.465258.

[102] J. C. Light and T. Carrington Jr. *Discrete-Variable Representations and their Utilization*, pp. 263–310. John Wiley & Sons, Ltd (2007). ISBN 9780470141731. doi:10.1002/9780470141731.ch4.

[103] M. Olshanii. Atomic scattering in the presence of an external confinement and a gas of impenetrable bosons. Phys. Rev. Lett., **vol. 81**; pp. 938–941 (1998). doi:10.1103/PhysRevLett.81.938.

[104] E. Timmermans, P. Tommasini, M. Hussein, and A. Kerman. Feshbach resonances in atomic bose–einstein condensates. Physics Reports, **vol. 315**(1); pp. 199–230 (1999). doi:10.1016/S0370-1573(99)00025-3.

[105] W. Ketterle, D. M. Stamper-Kurn, H.-J. Miesner, J. Stenger, M. R. Andrews, and S. Inouye. Observation of feshbach resonances in a bose–einstein condensate. Nature, **vol. 392**; pp. 151–154 (1998). doi:10.1038/32354.

[106] C. Chin, R. Grimm, P. Julienne, and E. Tiesinga. Feshbach resonances in ultracold gases. Rev. Mod. Phys., **vol. 82**; pp. 1225–1286 (2010). doi:10.1103/RevModPhys.82.1225.

[107] A. U. J. L. Lode, M. C. T. Tsatsos, E. Fasshauer, L. P. R. Lin, P. Molignini, C. Lévêque, and S. E. Weiner. MCTDH-X: The Time-dependent multiconfigurational Hartree for indistinguishable particles software. `http://ultracold.org`. Accessed: 2019-07-17.

[108] C. Ryu, P. W. Blackburn, A. A. Blinova, and M. G. Boshier. Experimental realization of josephson junctions for an atom squid. Phys. Rev. Lett., **vol. 111**; p. 205301 (2013). doi:10.1103/PhysRevLett.111.205301.

[109] L. Amico, G. Birkl, M. Boshier, and L.-C. Kwek. Focus on atomtronics-enabled quantum technologies. New J. Phys., **vol. 19**; p. 063201 (2017). doi:10.1088/1367-2630/aa5a6d.

[110] C. Ryu, E. C. Samson, and M. G. Boshier. Quantum interference of currents in an atomtronic squid. Nature Communications, **vol. 11**; p. 3338 (2020). doi:10.1038/s41467-020-17185-6.

[111] A. C. Mathey and L. Mathey. Realizing and optimizing an atomtronic SQUID. New Journal of Physics, **vol. 18**(5); p. 055016 (2016). doi:10.1088/1367-2630/18/5/055016.

[112] L. Amico, M. Boshier, G. Birkl, A. Minguzzi, C. Miniatura, L.-C. Kwek, D. Aghamalyan, V. Ahufinger, D. Anderson, N. Andrei, A. S. Arnold, M. Baker, T. A. Bell, T. Bland, J. P. Brantut, D. Cassettari, W. J. Chetcuti, F. Chevy, R. Citro, S. De Palo, R. Dumke, M. Edwards, R. Folman, J. Fortagh, S. A. Gardiner, B. M. Garraway, G. Gauthier, A. Günther, T. Haug, C. Hufnagel, M. Keil, P. Ireland, M. Lebrat, W. Li, L. Longchambon, J. Mompart, O. Morsch, P. Naldesi, T. W. Neely, M. Olshanii, E. Orignac, S. Pandey, A. Pérez-Obiol, H. Perrin, L. Piroli, J. Polo, A. L. Pritchard, N. P. Proukakis, C. Rylands, H. Rubinsztein-Dunlop, F. Scazza, S. Stringari, F. Tosto, A. Trombettoni, N. Victorin, W. v. Klitzing, D. Wilkowski, K. Xhani, and A. Yakimenko. Roadmap on atomtronics: State

of the art and perspective. AVS Quantum Science, **vol. 3**(3); p. 039201 (2021). doi:10.1116/5.0026178.

[113] S. Bera, R. Roy, A. Gammal, B. Chakrabarti, and B. Chatterjee. Probing relaxation dynamics of a few strongly correlated bosons in a 1d triple well optical lattice. Journal of Physics B: Atomic, Molecular and Optical Physics, **vol. 52**(21); p. 215303 (2019). doi:10.1088/1361-6455/ab2999.

[114] I. M. Khalatnikov. *An Introduction to the Theory of Superfluidity*. Advanced Book Program, Perseus Publisher, New York (1965).

[115] V. F. Sears, E. C. Svensson, P. Martel, and A. D. B. Woods. Neutron-scattering determination of the momentum distribution and the condensate fraction in liquid ^{4}He. Phys. Rev. Lett., **vol. 49**; pp. 279–282 (1982). doi:10.1103/PhysRevLett.49.279.

[116] C. Raman, M. Köhl, R. Onofrio, D. S. Durfee, C. E. Kuklewicz, Z. Hadzibabic, and W. Ketterle. Evidence for a critical velocity in a Bose-Einstein condensed gas. Phys. Rev. Lett., **vol. 83**; pp. 2502–2505 (1999). doi:10.1103/PhysRevLett.83.2502.

[117] C. Ryu, M. F. Andersen, P. Cladé, V. Natarajan, K. Helmerson, and W. D. Phillips. Observation of persistent flow of a Bose-Einstein condensate in a toroidal trap. Phys. Rev. Lett., **vol. 99**; p. 260401 (2007). doi:10.1103/PhysRevLett.99.260401.

[118] A. Ramanathan, K. C. Wright, S. R. Muniz, M. Zelan, W. T. Hill, C. J. Lobb, K. Helmerson, W. D. Phillips, and G. K. Campbell. Superflow in a toroidal Bose-Einstein condensate: An atom circuit with a tunable weak link. Phys. Rev. Lett., **vol. 106**; p. 130401 (2011). doi:10.1103/PhysRevLett.106.130401.

[119] J. Clark and A. I. Braginski. *The SQUID Handbook*. Wiley-VCH, Weinheim (2004).

[120] L. Amico, A. Osterloh, and F. Cataliotti. Quantum many particle systems in ring-shaped optical lattices. Phys. Rev. Lett., **vol. 95**; p. 063201 (2005). doi:10.1103/PhysRevLett.95.063201.

[121] E. J. Mueller. Superfluidity and mean-field energy loops: Hysteretic behavior in Bose-Einstein condensates. Phys. Rev. A, **vol. 66**; p. 063603 (2002). doi:10.1103/PhysRevA.66.063603.

[122] S. Eckel, J. G. Lee, F. Jendrzejewski, N. Murray, C. W. Clark, C. J. Lobb, W. D. Phillips, M. Edwards, and G. K. Campbell. Hysteresis in a quantized superfluid 'atomtronic' circuit. Nature (London), **vol. 506**; pp. 200–203 (2014). doi:10.1038/nature12958.

[123] S. Baharian and G. Baym. Bose-Einstein condensates in toroidal traps: Instabilities, swallow-tail loops, and self-trapping. Phys. Rev. A, **vol. 87**; p. 013619 (2013). doi:10.1103/PhysRevA.87.013619.

[124] M. Syafwan, P. Kevrekidis, A. Paris-Mandoki, I. Lesanovsky, P. Krüger, L. Hackermüller, and H. Susanto. Superfluid flow past an obstacle in annular Bose–Einstein condensates. J. Phys. B: At. Mol. Opt. Phys., **vol. 49**(23); p. 235301 (2016). doi:10.1088/0953-4075/49/23/235301.

[125] K. C. Wright, R. B. Blakestad, C. J. Lobb, W. D. Phillips, and G. K. Campbell. Threshold for creating excitations in a stirred superfluid ring. Phys. Rev. A, **vol. 88**; p. 063633 (2013). doi:10.1103/PhysRevA.88.063633.

[126] M. Kunimi and I. Danshita. Decay mechanisms of superflow of Bose-Einstein condensates in ring traps. Phys. Rev. A, **vol. 99**; p. 043613 (2019). doi:10.1103/PhysRevA.99.043613.

[127] A. Kumar, S. Eckel, F. Jendrzejewski, and G. K. Campbell. Temperature-induced decay of persistent currents in a superfluid ultracold gas. Phys. Rev. A, **vol. 95**; p. 021602(R) (2017). doi:10.1103/PhysRevA.95.021602.

[128] J. H. Kim, S. W. Seo, and Y. Shin. Critical spin superflow in a spinor Bose-Einstein condensate. Phys. Rev. Lett., **vol. 119**; p. 185302 (2017). doi:10.1103/PhysRevLett.119.185302.

[129] S. Beattie, S. Moulder, R. J. Fletcher, and Z. Hadzibabic. Persistent currents in spinor condensates. Phys. Rev. Lett., **vol. 110**; p. 025301 (2013). doi:10.1103/PhysRevLett.110.025301.

[130] R. Lopes, C. Eigen, N. Navon, D. Clément, R. P. Smith, and Z. Hadzibabic. Quantum depletion of a homogeneous Bose-Einstein condensate. Phys. Rev. Lett., **vol. 119**; p. 190404 (2017). doi:10.1103/PhysRevLett.119.190404.

[131] R. Chang, Q. Bouton, H. Cayla, C. Qu, A. Aspect, C. I. Westbrook, and D. Clément. Momentum-resolved observation of thermal and quantum depletion in a Bose gas. Phys. Rev. Lett., **vol. 117**; p. 235303 (2016). doi:10.1103/PhysRevLett.117.235303.

[132] L. D. Carr, C. W. Clark, and W. P. Reinhardt. Stationary solutions of the one-dimensional nonlinear schrödinger equation. i. case of repulsive nonlinearity. Phys. Rev. A, **vol. 62**; p. 063610 (2000). doi:10.1103/PhysRevA.62.063610.

[133] J. Sato, R. Kanamoto, E. Kaminishi, and T. Deguchi. Quantum states of dark solitons in the 1d Bose gas. New J. Phys., **vol. 18**(7); p. 075008 (2016). doi:10.1088/1367-2630/18/7/075008.

[134] A. Muñoz Mateo, A. Gallemí, M. Guilleumas, and R. Mayol. Persistent currents supported by solitary waves in toroidal Bose-Einstein condensates. Phys. Rev. A, **vol. 91**; p. 063625 (2015). doi:10.1103/PhysRevA.91.063625.

[135] A. J. Leggett. Can a solid be "superfluid"? Phys. Rev. Lett., **vol. 25**; pp. 1543–1546 (1970). doi:10.1103/PhysRevLett.25.1543.

[136] X. Yin, Y. Hao, S. Chen, and Y. Zhang. Ground-state properties of a few-boson system in a one-dimensional hard-wall split potential. Phys. Rev. A, **vol. 78**; p. 013604 (2008). doi:10.1103/PhysRevA.78.013604.

[137] R. G. Dall, A. G. Manning, S. S. Hodgman, W. RuGway, K. V. Kheruntsyan, and A. G. Truscott. Ideal n-body correlations with massive particles. Nat. Phys., **vol. 9**; pp. 341–344 (2013). doi:10.1038/nphys2632.

[138] T. Schweigler, V. Kasper, S. Erne, I. Mazets, B. Rauer, F. Cataldini, T. Langen, T. Gasenzer, and J. Berges, Jürgen Schmiedmayer. Experimental characterization of a quantum many-body system via higher-order correlations. nature, **vol. 545**; pp. 323–326 (2017). doi:10.1038/nature22310.

[139] A. U. J. Lode, R. Lin, M. Büttner, L. Papariello, C. Lévêque, R. Chitra, M. C. Tsatsos, D. Jaksch, and P. Molignini. Optimized observable readout from single-shot images of ultracold atoms via machine learning. Phys. Rev. A, **vol. 104**; p. L041301 (2021). doi:10.1103/PhysRevA.104.L041301.

[140] I. Lovas, B. Dóra, E. Demler, and G. Zaránd. Quantum-fluctuation-induced time-of-flight correlations of an interacting trapped bose gas. Phys. Rev. A, **vol. 95**; p. 023625 (2017). doi:10.1103/PhysRevA.95.023625.

[141] S. Butera, D. Clément, and I. Carusotto. Position- and momentum-space two-body correlations in a weakly interacting trapped condensate. Phys. Rev. A, **vol. 103**; p. 013302 (2021). doi:10.1103/PhysRevA.103.013302.

[142] S. Moulder, S. Beattie, R. P. Smith, N. Tammuz, and Z. Hadzibabic. Quantized supercurrent decay in an annular bose-einstein condensate. Phys. Rev. A, **vol. 86**; p. 013629 (2012). doi:10.1103/PhysRevA.86.013629.

[143] B. Mottelson. Yrast spectra of weakly interacting bose-einstein condensates. Phys. Rev. Lett., **vol. 83**; pp. 2695–2698 (1999). doi:10.1103/PhysRevLett.83.2695.

[144] F. Bloch. Superfluidity in a ring. Phys. Rev. A, **vol. 7**; pp. 2187–2191 (1973). doi:10.1103/PhysRevA.7.2187.

[145] E. Kaminishi, R. Kanamoto, J. Sato, and T. Deguchi. Exact yrast spectra of cold atoms on a ring. Phys. Rev. A, **vol. 83**; p. 031601 (2011). doi:10.1103/PhysRevA.83.031601.

[146] K. Anoshkin, Z. Wu, and E. Zaremba. Persistent currents in a bosonic mixture in the ring geometry. Phys. Rev. A, **vol. 88**; p. 013609 (2013). doi:10.1103/PhysRevA.88.013609.

[147] R. Kanamoto, L. D. Carr, and M. Ueda. Metastable quantum phase transitions in a periodic one-dimensional bose gas. ii. many-body theory. Phys. Rev. A, **vol. 81**; p. 023625 (2010). doi:10.1103/PhysRevA.81.023625.

[148] G. Watanabe, F. Dalfovo, F. Piazza, L. P. Pitaevskii, and S. Stringari. Critical velocity of superfluid flow through single-barrier and periodic potentials. Phys. Rev. A, **vol. 80**; p. 053602 (2009). doi:10.1103/PhysRevA.80.053602.

[149] F. Piazza, L. A. Collins, and A. Smerzi. Vortex-induced phase-slip dissipation in a toroidal bose-einstein condensate flowing through a barrier. Phys. Rev. A, **vol. 80**; p. 021601 (2009). doi:10.1103/PhysRevA.80.021601.

[150] A. C. Mathey, C. W. Clark, and L. Mathey. Decay of a superfluid current of ultracold atoms in a toroidal trap. Phys. Rev. A, **vol. 90**; p. 023604 (2014). doi:10.1103/PhysRevA.90.023604.

[151] Z. Mehdi, A. S. Bradley, J. J. Hope, and S. S. Szigeti. Superflow decay in a toroidal bose gas: The effect of quantum and thermal fluctuations. SciPost Phys., **vol. 11**; p. 80 (2021). doi:10.21468/SciPostPhys.11.4.080.

[152] G. Gauthier, I. Lenton, N. M. Parry, M. Baker, M. J. Davis, H. Rubinsztein-Dunlop, and T. W. Neely. Direct imaging of a digital-micromirror device for configurable microscopic optical potentials. Optica, **vol. 3**(10); pp. 1136–1143 (2016). doi:10.1364/OPTICA.3.001136.

[153] M. Tajik, B. Rauer, T. Schweigler, F. Cataldini, J. ao Sabino, F. S. Møller, S.-C. Ji, I. E. Mazets, and J. Schmiedmayer. Designing arbitrary one-dimensional potentials on an atom chip. Opt. Express, **vol. 27**(23); pp. 33474–33487 (2019). doi:10.1364/OE.27.033474.

[154] A. Andriati, L. Brito, L. Tomio, and A. Gammal. Stability of a bose-condensed mixture on a bubble trap. Phys. Rev. A, **vol. 104**; p. 033318 (2021). doi:10.1103/PhysRevA.104.033318.

[155] L. Brito, A. Andriati, L. Tomio, and A. Gammal. Breakup of rotating asymmetric quartic-quadratic trapped condensates. Phys. Rev. A, **vol. 102**; p. 063330 (2020). doi:10.1103/PhysRevA.102.063330.